Spatially-coordinated airborne data and complementary products for aerosol, gas, cloud, and meteorological studies: The NASA ACTIVATE dataset

Armin Sorooshian[1,2,3], Mikhail D. Alexandrov[4,5], Adam D. Bell[6], Ryan Bennett[7], Grace Betito[2], Sharon P. Burton[8], Megan E. Buzanowicz[6,8], Brian Cairns[4], Eduard V. Chemyakin[6,8], Gao Chen[8], Yonghoon Choi[6,8], Brian L. Collister[8], Anthony L. Cook[8], Andrea F. Corral[1], Ewan C. Crosbie[6,8], Bastiaan van Diedenhoven[9], Joshua P. DiGangi[8], Glenn S. Diskin[8], Sanja Dmitrovic[3], Eva-Lou Edwards[1], Marta A. Fenn[6,8], Richard A. Ferrare[8], David van Gilst[7], Johnathan W. Hair[8], David B. Harper[8], Miguel Ricardo A. Hilario[2], Chris A. Hostetler[8], Nathan Jester[8], Michael Jones[6,8], Simon Kirschler[10,11], Mary M. Kleb[8], John M. Kusterer[8], Sean Leavor[6,8], Joseph W. Lee[8], Hongyu Liu[12], Kayla McCauley[2], Richard H. Moore[8], Joseph Nied[8], Anthony Notari[8], John B. Nowak[8], David Painemal[6,8], Kasey E. Phillips[8], Claire E. Robinson[6,8], Amy Jo Scarino[6,8], Joseph S. Schlosser[6,13], Shane T. Seaman[8], Chellappan Seethala[14], Taylor J. Shingler[8], Michael A. Shook[8], Kenneth A. Sinclair[4,5], William L. Smith Jr.[8], Douglas A. Spangenberg[6,8], Snorre A. Stamnes[8], Kenneth L. Thornhill[6,8], Christiane Voigt[10,11], Holger Vömel[15], Andrzej P. Wasilewski[4], Hailong Wang[16], Edward L. Winstead[6,8], Kira Zeider[1], Xubin Zeng[2], Bo Zhang[12], Luke D. Ziemba[8], Paquita Zuidema[14]

[1]Department of Chemical and Environmental Engineering, University of Arizona, Tucson, AZ, USA
[2]Department of Hydrology and Atmospheric Sciences, University of Arizona, Tucson, AZ, USA
[3]James C. Wyant College of Optical Sciences, University of Arizona, Tucson, AZ, USA
[4]NASA Goddard Institute for Space Studies, New York, NY, USA
[5]Department of Applied Physics and Applied Mathematics, Columbia University, New York, NY, USA
[6]Science Systems and Applications, Inc., Hampton, VA, USA
[7]Bay Area Environmental Research Institute, NASA Ames Research Center, Moffett Field, CA, USA
[8]NASA Langley Research Center, Hampton, VA, USA
[9]SRON Netherlands Institute for Space Research, Leiden, the Netherlands
[10]Institute of Atmospheric Physics, German Aerospace Center, Germany
[11]Institute of Atmospheric Physics, University Mainz, Germany
[12]National Institute of Aerospace, Hampton, VA, USA
[13]NASA Postdoctoral Program, NASA Langley Research Center, Hampton, VA, USA
[14]Rosenstiel School of Marine, Atmospheric, and Earth Science, University of Miami, Miami, FL, USA
[15]National Center for Atmospheric Research, Boulder, CO, USA
[16]Atmospheric Sciences and Global Change Division, Pacific Northwest National Laboratory, Richland, WA, USA

Correspondence to: Armin Sorooshian (armin@arizona.edu)

Abstract. The NASA Aerosol Cloud meTeorology Interactions oVer the western ATlantic Experiment (ACTIVATE) produced a unique dataset for research into aerosol-cloud-meteorology interactions with applications extending from process-based studies to multi-scale model intercomparison and improvement, and remote sensing algorithm assessments and advancements. ACTIVATE used two NASA Langley Research Center aircraft, a HU-25 Falcon and King Air, to conduct systematic and spatially coordinated flights over the northwest Atlantic Ocean amounting to 162 joint flights and 17 other single-aircraft flights between 2020 and 2022 across all seasons. Data cover 574 and 592 cumulative flights hours for the Falcon and King Air, respectively. The HU-25 Falcon conducted profiling at different level legs below, in, and just above boundary layer clouds (<3 km) and obtained in situ measurements of trace gases, aerosol particles, clouds, and atmospheric state parameters. In cloud-free conditions, the Falcon similarly conducted profiling at different level legs within and immediately above the boundary layer. The King Air (the high-flyer) flew at approximately ~9 km conducting remote sensing with a lidar and polarimeter while also launching dropsondes (785 in total). Collectively, simultaneous data collected from both aircraft help characterize the same vertical column of the atmosphere. In addition to individual instrument files, data from the Falcon aircraft are combined into "merge files" on the publicly available data archive that are created at different time resolutions of interest (e.g., 1, 5, 10, 15, 30, 60 s, or matching an individual data product start and stop times). This paper describes the ACTIVATE flight strategy, instrument and complementary dataset products, data access and usage details, and data application notes.

1 Introduction

Aerosol-cloud interactions are responsible for the largest uncertainty in estimates of total anthropogenic radiative forcing (Bellouin et al., 2020). This uncertainty stems partly from the difficulty in experimentally characterizing such interactions in the atmosphere due to the need for methods such as with airborne platforms. Also, it is challenging to isolate the relative influence of different factors that impact the life cycle and properties of clouds including meteorology and aerosol particles. Decades of airborne field studies focused on aerosol-cloud interactions have been limited in terms of data volume and number of variables measured, diversity of aerosol and weather conditions, and vertical data coverage. These limitations motivated the conception of the NASA Aerosol Cloud meTeorology Interactions oVer the western ATlantic Experiment (ACTIVATE), which included systematic, extensive, and spatially-coordinated flights with two aircraft over the northwest Atlantic (Sorooshian et al., 2019). ACTIVATE is one of five Earth Venture Suborbital-3 (EVS-3) missions.

ACTIVATE flights were strategically executed in different seasons (e.g., winter and summer) to increase the dynamic range of aerosol and meteorological conditions that resulted in different cloud types spanning warm and mixed-phase clouds, and the continuum from stratiform to cumulus clouds. The northwest Atlantic differs from subtropical regions often chosen for aerosol-cloud interaction campaigns due to multiple cloud types within reach, rather than the stratocumulus clouds that are simpler to characterize owing to their high cloud fraction and well-defined vertical structure as demonstrated by campaigns over the northeast Pacific (e.g., Durkee et al., 2000; Sorooshian et al., 2018), southeast Pacific (e.g., Mechoso et al., 2014), and southeast Atlantic (e.g., Zuidema et al., 2016; Redemann et al., 2021). ACTIVATE adds to the much needed inventory of data over the northwest Atlantic to build on efforts from projects such as the North Atlantic Regional Experiment (NARE; Leaitch et al., 1996), the Surface Ocean - Lower Atmosphere Study (SOLAS; Leaitch et al., 2010), the International Consortium for Atmospheric Research on Transport and Transformation (ICARTT; Avey et al., 2007), the Two - Column Aerosol Project (TCAP), and the Investigation of Microphysics and Precipitation for Atlantic Coast-Threatening Snowstorms (IMPACTS). With a disciplined strategy of conducting the same type of flight plan for over 90% of the flights (called "statistical surveys"), data were repeatedly collected at different vertical levels in and above the marine boundary layer, including within and immediately below and above clouds. Another subset of flights called "process studies" comprised more customized flight patterns to capitalize on targets of opportunity for remote sensing algorithm assessments and detailed model intercomparison studies such as with wintertime cold air outbreaks and summertime developing cumulus clouds. This rich dataset is ideal for a number of research applications including studying processes, model evaluation and improvement, parameterization development, and remote sensing algorithm analysis and advancement.

To aid the research community in the usage of the ACTIVATE data, the goal of this work is to provide a guide for users. The structure of this paper is as follows: (i) a description of the ACTIVATE campaign and flight strategy, which involved spatial coordination between a high-flying King Air and a low-flying HU-25 Falcon; (ii) summary of King Air instruments and associated datasets; (iii) summary of Falcon instruments and associated datasets; (iv) description of complementary data products; (v) visualization of data products relevant to a representative case study flight; (vi) data/code availability and file format; and (vii) conclusions. To guide readers, Appendix A has a nomenclature table defining all acronyms and abbreviations used in this paper. A forthcoming paper will provide a comprehensive overview of the science results from ACTIVATE and how those fit into the larger picture of past campaigns focused on aerosol-cloud interactions.

2 Field campaign description

2.1 Objectives, operations bases, and schedule

ACTIVATE generated a novel dataset that can be used to address three overarching objectives that were developed during the conception of the mission plan: (i) quantify relationships amongst aerosol particle number concentration (N_a), cloud condensation nuclei (CCN) concentration, and cloud drop number concentration (N_d), and reduce uncertainty in model parameterizations of aerosol activation and cloud formation; (ii) improve process-level understanding and model representation of factors that govern cloud micro/macro-physical properties and how they couple with cloud effects on aerosol; and (iii) assess advanced remote sensing capabilities for retrieving aerosol and cloud properties related to aerosol-cloud interactions. To achieve these objectives, it was important to conduct a high number of flights across different seasons to collect sufficient statistics across a range of aerosol, cloud, and meteorological conditions for more robust calculations relevant to understanding the life cycle and properties of different types of boundary layer clouds (e.g., stratiform and cumulus; mixed-phase and warm clouds). To address the challenge of needing data for different vertical levels relevant to the aerosol-cloud system and to achieve remote sensing objectives, two aircraft were employed that were kept highly coordinated in both space and time. These planes included the NASA Langley Research Center's HU-25 Falcon (low flyer, < 3 km) and King Air (high flyer, ~9 km). A critical element in the selection of the two aircraft was that both aircraft flew close to 120 m s^{-1} at their respective sampling altitudes. The flights were limited by the endurance of the aircraft (< 4 hours) and so flights were designed to try to extend the spatial range as much as possible while also still being able to characterize different vertical levels. This resulted in an approach of flying "statistical surveys" comprised of repeated "ensembles" that we describe below (sect. 2.2) and that have been discussed in detail elsewhere for ACTIVATE flights (Dadashazar et al., 2022b).

The northwest Atlantic study region is ideal for ACTIVATE objectives owing to the wide range of aerosol types and weather conditions (Corral et al., 2021; Painemal et al., 2021; Sorooshian et al., 2020) during the periods that flights would take place, which ended up including November-June and August-September. Flights were mostly based out of NASA Langley Research Center (NASA LaRC) with only a few others based out of secondary bases, including Newport News-Williamsburg International Airport (Virginia), Quonset State Airport (Rhode Island), Rhode Island T.F. Green International Airport (Rhode Island), and L. F. Wade International Airport (Bermuda). The original goal for flights was to do 25 joint flights in each of 6 deployments between 2020 and 2022, including a Winter (February-March) and Summer (May-June) deployment each year. As a result of operational delays, aircraft maintenance challenges, and COVID-19 emerging during the first deployment, deviations were necessary relative to the original flight schedule plan; however, the overall science plan was unaffected. These deviations are evident in Table 1, which shows a summary of flight metrics for each of the six deployments. Table 2 further summarizes each individual flight, including details specific to each aircraft such as takeoff and landing time, and special features per flight. It is difficult to assign specific flights to ACTIVATE's individual scientific objectives (sect. 2.1) because statistics from all flights can be helpful to each objective; however, that being said, Table 2's notes of special features and designation of some flights as "process study" flights (described in sect. 2) can be helpful for data users most interested in remote sensing objectives (e.g., satellite underflights, relatively more cloud-free conditions with high aerosol levels) and modeling activities such as large eddy simulation of cold air outbreak conditions (e.g., Li et al., 2022). Figure 1 shows the flight tracks each year for the Falcon and King Air.

2.2 Flight strategy

The original goal of ACTIVATE was to allocate 90% of the flights to "statistical surveys" whereby the two aircraft would repeatedly conduct coordinated cloud and cloud-free ensembles (Fig. 2). The threshold and baseline science mission success metrics from a flight perspective hinged on acquiring many of these ensembles for more robust calculations of aerosol-cloud-meteorology interactions. ACTIVATE far surpassed the number of ensembles needed for threshold and baseline mission requirements. Ensemble numbers and definitions of these mission categories are provided in Table 1. Cloud ensembles performed by the lower-flying Falcon included flying level legs (~3 min each unless otherwise dictated by flight conditions) in the following nominal order: below cloud base (BCB), above cloud base (ACB), a second pair of BCB and ACB, minimum altitude (MinAlt), above cloud top (ACT), below cloud top (BCT). MinAlt is defined as the lowest altitude the aircraft could fly at, which was ~150 m above sea level when clear of cloud and in good visibility conditions. The slant ascents from MinAlt to ACT provided multiple in situ vertical profiles across the range of relevant altitudes and included periods of cloudy and cloud-free sampling depending on conditions. A caveat with the interpretation of these "vertical" profiles is that in environments with spatially varying conditions (e.g., broken or episodic cloud), the slant ascent may not represent average conditions with any reliability. Clear ensembles in cloud-free conditions included legs in the following nominal order: MinAlt, above boundary layer top (ABL), below boundary layer top (BBL), Remote Sensing (RS) leg. The RS leg was implemented under conditions of high aircraft coincidence (<5 min and <6 km of separation between Falcon and King Air) and when no clouds affected the field of view. The RS leg provided a second low-altitude leg (~230 m) to help with lidar extinction comparison in the challenging near-surface region. The altitude of the ABL leg was estimated by flight scientists based on gradients in the available real-time data during ascents and descents. Occasionally deviations occurred to these leg orders for both ensemble types based on atmospheric conditions and air traffic control challenges requiring changes in altitude. The time span (distance) of each leg and cloud ensemble was ~3.3 min (~24 km) and ~35 min (~250 km), respectively, while clear ensembles were typically ~15 min (~100 km) (Dadashazar et al., 2022b). Across 162 final joint flights, all but 12 were classified as statistical surveys (93%), with classifications of each flight shown in Table 2. An archived forward camera video from the HU-25 Falcon on a representative statistical survey is accessible at this link to show data users how the ensembles appeared visually from the perspective of the aircraft: https://asdc.larc.nasa.gov/news/activate-data-webinar-materials. A representative statistical survey flight is discussed in more detail in sect. 6.

The disciplined approach of statistical surveys is uncommon for airborne flight projects as often the temptation is to target the most interesting features on a given day such as the strongest aerosol signal (e.g., smoke or dust plume) or opportunistic experimental conditions suited for aerosol-cloud interactions (e.g., ship tracks) (e.g., Christensen et al., 2022). Building routine statistics below, within, and above boundary layer clouds with a consistent flight strategy across a large number of flights is advantageous for developing probability density distributions of aerosol, cloud, and meteorological properties in a given region, which can be used to trace back onto processes. Furthermore, this approach provided a consistent dataset to better optimize data use among a diverse set of users.

The remaining 10% of flights were intended to be "process study" flights, with their number reduced to 12 out of 162 (7%) in practice. The goal of these flights was to focus on a target of opportunity with more detailed characterization in one location of a particularly interesting cloud scene. Four of the 12 process studies were conducted during wintertime cold air outbreak events, with the remaining eight focused on summertime cumulus cloud fields. These flights typically entailed more detailed vertical characterization in the same atmospheric column with the Falcon conducting stacked legs below, in, and above clouds (often termed a "wall" pattern) with bounding vertical soundings at the beginning and end of the wall(s). During that time, the high-flying King Air would conduct a carefully designed module at high altitude to maximize coordination, but also to provide detailed information about the scene encompassing the clouds of interest. For example, during some winter process studies, the King Air conducted a large circle aloft with numerous launched dropsondes to derive relevant quantities such as divergence profiles and surface fluxes to be used for model intercomparison studies (Chen et al., 2022a; Seethala et al., 2021; Li et al., 2022). A visual representation of a generic process study flight is shown in Fig. 3. Note that the aircraft would still conduct ensembles (Fig. 2) during process study flights during transits to and from the key area of focus where a "wall pattern" would be conducted.

2.3 Recommended terminology

The following guidelines are encouraged when reporting information about specific flights based on information in Table 2. References should provide the RF number and date. In cases of two flights on a given day, one can additionally include "L1" and/or "L2" to signify launch 1 and 2, respectively. Note here that launch number refers to the aircraft launch number per day following the International Consortium for Atmospheric Research on Transport and Transformation (ICARTT; described more in sect. 7) naming convention (Northup et al., 2017) and not processing level as employed by the satellite and remote sensing community. Since each flight has a unique RF number, the launch number becomes more important if only flight dates are used without reference to the RF number. Therefore, examples include: "RF1 (14 February 2020)"; "RF6 (22 February 2020) or "22 February 2020, L2". Furthermore, it is encouraged to refer to the six deployments according to their season and year for simplicity (e.g., Winter 2020, Summer 2020, Winter 2021, Summer 2021, Winter 2022, Summer 2022) as shown in Table 1, with the caveat that Winter 2022 still includes November-December flights occurring in 2021. This is encouraged for simplicity even though the months of flights do not perfectly align with typical seasonal definitions (e.g., DJF = winter, JJA = summer).

2.4 Special flight details

A few special features are worth expanding on that impacted flight execution:

- Single aircraft flights (17 in total) were conducted when one of the aircraft remained grounded, usually for a maintenance issue. In rare cases such as RF177 (16 June 2022), both planes began a joint flight, but one plane (Falcon in this case) experienced a maintenance issue during flight and returned to base without any science data archived. This meant the flight qualified as a single aircraft flight as only the King Air obtained archivable data. For single Falcon flights, statistical surveys were usually conducted with one process study flight; RF163 on 2 June 2022 was a unique process study flight in that it was conducted with the Falcon alone and involved wall patterns. The King Air also conducted its usual flight strategy in single aircraft flights, flying aloft around ~9 km and sampling targets of opportunity that were deemed to be too important to miss, even in the absence of the Falcon, such as cold air outbreaks (e.g., RF42 on 29 January 2021).
- Flights based out of either NASA Langley Research Center or Newport News-Williamsburg International Airport almost always included transits to one of two waypoints (ZIBUT [36.938° N, 72.666° W] or OXANA [34.363° N, 73.759° W]) to adhere to strict air traffic control restrictions, beyond which farther offshore there was more flexibility for waypoint selection. Those two waypoints can be thought of as 'pivot-points' that are visually evident and labeled in Fig. 1. A few flights included transits from one of the two Virginia bases to the northeast to waypoint ZIZZI (38.941° N, 74.529° W; shown in Fig. 1) to strategically sample upwind conditions in cold air outbreaks. Due to limitations associated with the COVID-19 pandemic in the first four deployments (2020-2021), secondary bases for the purpose of extending ACTIVATE's spatial range were only used in deployments 5-6 in 2022.
    - Notable was a series of flights based in Bermuda in June 2022 to make up for not flying there earlier in the campaign. The rationale for data collection around Bermuda was multifold: (i) farther removed from continental pollution sources and thus closer resembling a remote marine aerosol regime; (ii) conditions simplify parsing out causal drivers for aerosol-cloud interactions (e.g., less impacted by terrestrial boundary layer and Gulf Stream effects). The coastal region by the mid-Atlantic states has a strong airmass disequilibrium (e.g., high air-sea contrasts), but farther downwind airmasses relax to a more (quasi-) steady state, which has more global relevance than coastal regions; (iii) connect aircraft measurements with long-term surface measurements conducted at Bermuda (Sorooshian et al., 2020), including notable long-term aerosol and precipitation datasets collected through the Bermuda Institute of Ocean Sciences with demonstrated utility for ACTIVATE as shown in recent studies (Aldhaif et al., 2021; Dadashazar et al., 2021a); and (iv) bridge the gap for aerosol-cloud studies done in polluted conditions versus low-CCN conditions observed during missions like the North Atlantic Aerosols and Marine Ecosystems Study

(NAAMES) (Behrenfeld et al., 2019) and the Aerosol and Cloud Experiments in the Eastern North Atlantic (ACE-ENA) (Wang et al., 2022).

- Numerous flights were coordinated with satellite overpasses to achieve remote sensing objectives. Six and eleven of these 'underflights' of satellites were conducted in coordination with the Advanced Spaceborne Thermal Emission and Reflection Radiometer (ASTER) and Cloud-Aerosol Lidar and Infrared Pathfinder Satellite Observations (CALIPSO), respectively. In a few instances, the two aircraft coordinated to observe aerosol particles in clear sky conditions with the complete set of remote sensing polarimeter and lidar instruments with a matching full vertical profile of in-situ observations; this is related in part to past attempts to do such coordinated maneuvers in other regions (Xu et al., 2021). This type of aircraft observation module that must include an ascent/descent or spiraling aircraft pattern by the in-situ aircraft, became known as "unicorn aerosol modules". This name stuck thanks to the artwork of a team member's elementary schooler. These modules included the Falcon conducting a vertical spiral sounding with a slower climb rate (2-5 m s^{-1}) from its lowest possible altitude (usually ~120-150 m) to usually upwards of 5 km to reach the ceiling of high aerosol loadings, with the King Air flying aloft as it normally does. These modules targeted cloud-free scenes with relatively high aerosol concentrations to address aerosol optical and microphysical property remote sensing objectives, with a demonstration of results reported by Schlosser et al. (2022). Examples are associated with RF28 (26 August 2020), RF29 (28 August 2020), RF130 (2 March 2022), RF131 (3 March 2022), RF144 (26 March 2022) and RF155 (17 May 2022). Although not labelled as unicorn modules in Table 2, several spiral profiles were conducted with the Falcon just offshore of the Tudor Hill Marine Atmospheric Observatory during the set of Bermuda flights in June 2022 with the King Air flying overhead; these profiles sometimes included cloud (e.g., RF169 on 8 June 2022, RF178 on 17 June 2022) and were farther removed from the polluted eastern coast of the U.S. However, African dust was present during some of these cases and thus may interest some data users. Examples of Tudor Hill spirals with King Air overpasses are in RFs 166, 167, 169, 170, 172, 174, 175, 178 (dates shown in Table 2). The Tudor Hill site managed by the Bermuda Institute of Ocean Sciences was used during the June 2022 deployment for extensive surface and tower measurements relevant to atmospheric chemistry as part of the Bermuda boundary Layer Experiment on the Atmospheric Chemistry of Halogens (BLEACH).
- The HU-25 Falcon experienced a significant maintenance issue at the completion of RF47 (21 February 2021), resulting in a reduced instrument payload for the remainder of the Winter 2021 deployment (RF48-61, from 4 March to 2 April 2021). The following instruments (described in sect. 4) were not allowed to operate or collect data to minimize electrical power demand: trace gases (Picarro, 2B Tech.), AMS, PILS, CVI. The 11-day gap between RF47 and RF48 (4 March 2021) was due to the adaptation of the Falcon aircraft to the new payload strategy. To make up for most of Winter 2021 flights not having full payload capability, the Winter 2022 deployment was essentially the equivalent of two deployments, with flights starting as early as 30 November 2021 and ending 29 March 2022 (55 total flights rather than the nominal 25). No research flights occurred from 10 December 2021 to 11 January 2022 to observe the winter holiday period.

- Effort was made to keep the two aircraft as spatially coordinated as possible throughout the 162 joint flights. This at times was challenging due to pronounced differential wind speeds (and direction) between the boundary layer (Falcon) and at the ~8-10 km altitude (King Air), and due to unforeseen delays in takeoff for the second aircraft on a given day, typically due to the airfield operations. The goal was to try to keep the aircraft within approximately 5 minutes and 6 km of each other. This goal was attained for ~73% of the dataset (Schlosser et al., in review). If one aircraft was too far ahead, often it would conduct a "delay loop (i.e., racetrack)" whereby it would fly in a reverse track until the other aircraft caught up after which it would turn around again and fly in joint fashion. An example is shown in Fig. 3a for RF13 (1 March 2020, L1). Sometimes the trailing aircraft would turn around sooner at the "turn point" of an out-and-back flight to help reduce the spacing.

3 King Air measurements

Two separate King Air aircraft were used during the campaign, with nearly identical flight performance characteristics. The science payload was moved from the King Air with tail number N528NA (UC-12) to a second King Air with tail number N529NA (B200) for RF94 through RF119 to accommodate science flights during a planned maintenance period on N528NA. All other King Air research flights were flown on N528NA. Table 3 summarizes the King Air payload along with measured variables from each instrument and associated uncertainties and resolutions. Figure 4 shows a visual summary of the interior King Air layout. Table S1 (supplementary information) summarizes performance of each instrument on both aircraft for each flight to aid data users requiring at least some minimum combination of functional instruments for their applications. Each instrument package is described in detail below.

3.1 Applanix navigational data

For basic navigational and aircraft motion information, an Applanix 610 system acquired 1 second data for calendar day, time, latitude, longitude, GPS altitude, ground speed, vertical speed, true heading, track/drift/pitch/roll angle.

3.2 High spectral resolution lidar – generation 2 (HSRL-2)

The NASA Langley High Spectral Resolution Lidar (HSRL-2) is a multiwavelength airborne HSRL providing vertically resolved extensive and intensive aerosol properties. Extensive properties are those that depend both on aerosol particle properties and concentration whereas intensive properties depend only on the particle properties and are independent of concentration. Archived HSRL-2 core data include high resolution profiles of particulate backscatter and depolarization at three wavelengths (355, 532, 1064 nm) and simultaneous and independent measurements of particulate extinction at two wavelengths (355, 532 nm) via the HSRL technique (Hair et al., 2008; Burton et al., 2018). These profiles are used to derive horizontally and vertically resolved curtains of extinction and backscatter Ångström exponent, lidar ratio (i.e., extinction-to-backscatter ratio), backscatter Ångström exponents for spherical and nonspherical particles (dust, crystalline sea salt)

(Sugimoto and Lee, 2006), and aerosol type (Burton et al., 2012). Cloud screening is performed using a convolution of the measured 532 nm signal with a Haar wavelet to enhance edges (Davis et al., 2000) separating the sharper cloud edges from less pronounced aerosol features in each lidar profile. Cloud top altitudes are provided. Both cloud screened and non-cloud screened aerosol scattering ratio (i.e., ratio of aerosol scattering to molecular scattering), aerosol backscatter, and aerosol depolarization profiles are computed and provided at the three wavelengths. Aerosol extinction, aerosol optical thickness, and lidar ratio at 355 and 532 nm are provided only for cloud-free regions. If a cloud is detected in a profile, these data products are restricted to the region above the cloud top. The 532 nm molecular scattering signal for each profile is used to check that signal levels are sufficiently high to derive these aerosol products. Aerosol depolarization at 532 nm and 1064 nm (355 nm) is computed when aerosol scattering ratio values exceed 0.2 (0.068). The HSRL-2 backscatter and depolarization products are reported as 10 second averages while the extinction and lidar ratio products are averaged to 60 seconds. Higher resolution products are available from the HSRL-2 team upon request.

The aerosol backscatter product is also used to derive an aerosol mixed-layer height (MLH) (Fast et al., 2012; Scarino et al., 2014). Mixed layer heights are based on sharp gradients in aerosol backscatter profiles that are found using a modified Haar wavelet approach (Scarino et al., 2014). The MLH remains challenging to accurately determine in complex atmospheric conditions, such as shallow marine boundary layers (MBLs) and multiple aerosol layers as a function of altitude. There are many ways MLH can be defined and retrieved, and thus users should use discretion in how they use MLH data for their given applications. Aerosol typing (maritime, polluted maritime, pure dust, dusty mix, smoke, fresh smoke, urban, and ice) is based on an algorithm using depolarization, depolarization wavelength dependence, aerosol backscatter wavelength dependence, and the aerosol lidar ratio (Burton et al., 2012).

Under ACTIVATE, additional new HSRL-2 geophysical products have been developed (or under development), including an aerosol hygroscopic growth parameter for well-mixed MBLs, 10 m surface wind speeds, several cloud products, and an in-ocean backscatter product. A new product that is under development is the aerosol hygroscopic growth parameter f(RH), which is produced using the HSRL-2 aerosol backscatter product and state parameters retrieved from the AVAPS dropsonde system (sect. 3.5) in well-mixed MBLs (Ferrare et al., forthcoming). 10 m neutral stability (U10) surface wind speeds are estimated using HSRL-2 retrievals of sea surface backscatter, i.e., the reflectance of the transmitted laser pulses from the ocean surface (Dmitrovic et al., forthcoming). The surface backscatter, retrieved with a 1.25 m vertical resolution that corrects for ocean subsurface scattering, is highly correlated with sea surface wave-slope variance, which is then related to wind-speed through various empirical relationships (Cox and Munk, 1954; Hu et al., 2008). New HSRL-2 cloud retrieval products include cloud top height, cloud top extinction, and cloud top lidar ratio at horizontal resolutions of 75 m, 150 m, and 150 m, respectively (Hair et al., forthcoming). Relevant to ocean-air interactions such as marine biogenic emissions (Corral et al., 2022a), ocean subsurface particulate backscatter coefficients at 532 nm are estimated at a depth of 10 m (Schulien et al., 2017) and made available for selected flights.

Figure 5 provides a visualization of many of the aforementioned HSRL-2 data products for a representative flight (RF157 on 18 May 2022). Figure 5a shows profiles of aerosol backscatter (532 nm) for the entire flight from Bermuda to NASA LaRC in southeastern Virginia. Note the horizontal and vertical variability of aerosol particles throughout the flight. The labeled boxes indicate regions where subsets of HSRL-2 data products are shown in the corresponding small boxes below Figure 5a; these are shown for clouds (5b), boundary layer and lower troposphere aerosols (5c), and an elevated aerosol layer (5d). These small boxes provide brief visualizations of these various data products. Blue dots in Figure 5b show (left subplot) cloud top height and (right subplot) cloud top extinction, averaged over the first optical depth, for this region. Figure 5c shows HSRL-2 products including mixed layer height (blue dots), surface wind speed (black line), aerosol type, aerosol depolarization (UV (355 nm), VIS (532 nm), IR (1064 nm)), and backscatter Ångström exponents corresponding to spherical and nonspherical particles (dust, crystalline sea salt) in the boundary layer and lower troposphere. Figure 5d shows HSRL-2 products in the aerosol layer between 4.5-6.5 km including aerosol backscatter (UV (355 nm), VIS (532 nm), IR (1064 nm)), backscatter Ångström exponents (VIS/UV and IR/VIS), lidar ratios (UV and VIS), aerosol extinction (UV, VIS), extinction Ångström exponent (UV/VIS), and total column AOT (UV, VIS) (indicated by the blue and green lines in bottom of right figure).

3.3 Research scanning polarimeter (RSP)

Retrievals of aerosol, cloud, and surface reflectance properties were provided by the Research Scanning Polarimeter (RSP), which is a passive, downward-looking polarimeter, with nine spectral bands (band centers: 410, 470, 550, 670, 865, 960, 1590, 1880, and 2260 nm) that scans its 14 mrad instantaneous field of view (~100 m) along the King Air ground track (Cairns et al., 2003). Each RSP scan views the earth over an angular range of ±55° from nadir (~ 140 views) every 0.8 seconds providing radiance and linear polarization measurements in all nine spectral bands. Each scan includes stability, dark reference, and calibration checks. A few decisions in flight planning and execution aimed to enhance RSP data quality: (i) as much as possible to keep the aircraft stable (e.g., yaw and roll); (ii) unless there was a high priority reason to fly under cirrus clouds, plan the typically joint flights for days with minimal cirrus clouds forecast above the flight track, to allow for more accurate determination of the incoming solar radiation; and (iii) fly as close as possible to the solar principal plane (i.e., azimuthally toward or away from the Sun) based on the scientific benefits of observing sunglint and maximizing the range of scattering angles observed including in the range from 135 to 165 degrees for the polarimetric cloud bow retrievals. The public data archive contains readme files provided by the RSP team for their Level 1C and Level 2 cloud and aerosol products, including important details about biases and uncertainties that data users should consult.

Because of the scanning nature whereby the RSP views areas behind and ahead of the plane, data are re-ordered in archived Level 1C files such that rather than being time-ordered, the data are sorted so that all the viewing angles that see the same nadir scene are put together. In cloud and cloud-free scenes, this amounts to data being aggregated to the cloud top and surface, respectively. Data from the Level 1C files are then used to develop Level 2 data files housing the aerosol and cloud data variables shown in Table 3. The RSP is ideally suited for characterizing warm cloud properties owing to the high angular density of observations per scene, with the polarized observations of the cloud bow allowing the retrieval of information about the droplet size distribution and also the detection and characterization of drizzle (Alexandrov et al., 2012b). Spectral bands in the regions where liquid and ice absorb (1.59 and 2.26 μm, respectively) also allow the RSP to obtain bi-spectral retrievals of droplet sizes, using the same technique as applied to satellite instruments such as the Moderate Resolution Imaging Spectroradiometer (MODIS) and the Visible Infrared Imaging Radiometer Suite (VIIRS). The primary cloud properties retrieved include cloud flag/test, cloud top altitude, cloud top phase index, cloud optical thickness, and cloud droplet size distribution (i.e., effective radius and variance). The cloud flag/test indicates whether a cloud was detected underneath the aircraft. A multi-angle parallax approach is used to estimate cloud top heights (Sinclair et al., 2017). The cloud top phase index variable indicates whether there is liquid at cloud top (Van Diedenhoven et al., 2012). Multi-angle polarimetry is used to retrieve effective radius and variance of the drop size distribution at cloud top for both liquid and mixed-phase clouds (Alexandrov et al., 2012b; Alexandrov et al., 2012a) and, for observations close to the solar principal plane, the drop size distribution itself (Alexandrov et al., 2012b; Alexandrov et al., 2012a). These multi-angle polarimetric retrievals have been validated against in situ observations (Adebiyi et al., 2020; Alexandrov et al., 2018) and found to be much more robust against artifacts than bi-spectral retrievals (Fu et al., 2022). Bi-spectral retrievals were also conducted for effective radius and cloud optical thickness (Nakajima and King, 1990). Column water vapor amount is provided above either the surface (cloud-free scenes) or cloud top (cloud scenes) (Sinclair et al., 2019).

Level 2 aerosol products (Stamnes et al., 2018; Schlosser et al., 2022) for both the fine and coarse mode include aerosol optical depth, aerosol size distribution parameters (effective radius/variance and number concentration), single scattering albedo (SSA), real part of the refractive index, and also ocean properties (ocean diffuse attenuation coefficient, ocean hemispherical backscatter coefficient, chlorophyll-a concentration, surface wind speed) are reported in these files based on a model for open ocean waters (Chowdhary et al., 2006). An aerosol layer height is also retrieved from the RSP observations (e.g., Wu et al., 2016), but we note that the HSRL-2 sensor provides far greater detail regarding the vertical distribution of aerosol particles.

3.4 Joint HSRL-2 and RSP retrieval products

Vertically-resolved N_a is derived for the first time using the vertically-resolved extinction backscatter coefficient [1/m] measured by HSRL-2 at 532 nm, combined with the column-averaged aerosol extinction cross-section for the fine-mode aerosol retrieved by RSP at 532 nm. The details of this combined lidar-polarimeter algorithm and comparisons against in-situ N_a are provided in Schlosser et al. (2022). Forthcoming work will summarize additional joint retrieval products that will be archived for public use once they are developed, including retrievals of N_d, liquid water content (LWC), and autoconversion rate at cloud top.

3.5 Dropsondes

The National Center for Atmospheric Research (NCAR) Airborne Vertical Atmospheric Profiling System (AVAPS) was deployed on the King Air to release dropsondes to obtain vertical distributions of pressure, wind (u, v, w components), static air and dew point temperature, and relative humidity (RH). Note, the horizontal wind components are measured directly, while the vertical wind is estimated using the dropsonde fall velocity. Manual releases were done using a dropsonde launch tube relying on NCAR NRD41 mini sondes, which have been summarized elsewhere and used in recent airborne campaigns such as the Organization of Tropical East Pacific Convection (OTREC) (Vömel et al., 2021) and the in-progress Investigation of Microphysics and Precipitation for Atlantic Coast-Threatening Snowstorms (IMPACTS). An extensive summary of the AVAPS system performance and quality control procedures during ACTIVATE is provided by Vömel et al. (in review).

Table 1 summarizes the number of dropsondes released per deployment, with a total of 785 providing full profiles of all variables with good parachute performance. Table 2 additionally shows the number of such full profiles per flight. The dropsondes provided vertical profiles between approximately the surface and ~9 km, which was the typical flight level of the King Air. However, releases were sometimes as low as ~5.2 km. Usually between 2-4 dropsondes were used per statistical survey flight with spatial separation such that each one gave a representative view of the atmospheric column in different portions of the flight. Process study flights involved more dropsondes (up to 23 in RF173 on 11 June 2022) to do more detailed characterization warranted for model intercomparison studies such as for cold air outbreaks (Chen et al., 2022; Li et al., 2022; Seethala et al., 2021) and summertime cumulus cloud systems (Li et al., in preparation).

3.6 Airborne camera images

Airborne camera images are useful for a variety of data analysis applications, and were collected by a nadir-facing camera mounted beneath the airplane and forward-facing camera mounted in the aircraft cockpit. One important application is the development of cloud masks to identify the presence of clouds above and below the aircraft, as detailed in sect. 5.4, which has been demonstrated already for the nadir camera on the King Air (Nied et al., 2023). Table 4 summarizes the camera details on the King Air, with different types of cameras used in nadir (Garmin VIRB Ultra 30 for RF1-RF61; AXIS F-1005-E for RF62 and onwards) and forward (GoPro for RF1-RF40; AXIS F-1005-E for RF41 and onwards) configuration throughout ACTIVATE. Photos taken with these cameras were stitched with UTC time stamps and archived as mp4 videos. Playback can be sped up on most MP4 viewers for faster viewing.

4 HU-25 Falcon measurements

Table 5 summarizes the instrument payload on the HU-25 Falcon with Table S1 summarizing instrument performance for each flight. Figure 6 shows visually the exterior probes and the interior layout of the Falcon. As noted earlier, a subset of instruments were not operated in the Winter 2021 deployment (RF48-61 from 4 March to 2 April 2021) to accommodate a power issue on the Falcon. Those instruments were deemed to be the lowest priority in terms of satisfying the three baseline ACTIVATE objectives summarized in sect. 2.1.

4.1 Applanix navigational data

Similar to the King Air, basic navigational and aircraft motion data (calendar day, time, latitude, longitude, GPS altitude, ground speed, vertical speed, true heading, track/drift/pitch/roll angle) were obtained with an Applanix 610 system with the exception that data were obtained natively at 20 Hz resolution and then averaged to 1 Hz resolution for archival. Data at 20

Hz resolution are available upon request. Similar to the King Air, Applanix data were recorded internally and on the real time data system and post-processed to obtain increased accuracy and precision via Applanix's proprietary software.

4.2 Diode Laser Hygrometer and trace gases

Three different instruments were used to measure trace gases including water vapor ($H_2O(v)$), CO_2, CH_4, CO, and O_3. The Diode Laser Hygrometer (DLH) is an open path, near infrared absorption spectrometer (Diskin et al., 2002) with its optical path entirely outside the Falcon cabin between a window in the cabin and a retroreflector affixed to the instrumentation pylon on the starboard wing. The round-trip beam path was on the order of 8 m with a vertical extent of ~1.5 m and a longitudinal extent of ~2 m, which, coupled with the optical data acquisition rate, define the limit on the temporal/spatial resolution of the measurement. DLH reported water vapor through 1 Hz and 20 Hz data products, but data are available upon request as fast as 60 Hz depending on airspeed. DLH data are available in clouds, but there was occasional data loss in very dense clouds due to a backscatter artifact. There was also occasional data loss caused by ice formation on the retroreflector, which prevented sufficient optical power from reaching the detector to make a measurement. These data were detected and removed, which reduces the water vapor data available within clouds and during/following icing. In addition to the primary DLH data product, water vapor mixing ratio, DLH water vapor data are converted to relative humidity with respect to both liquid water and ice using the on-board in situ measurements of ambient pressure and temperature described in sect. 4.3.

The other two instruments were located entirely within the cabin in a trace gas rack and were extractive, sampling from fuselage-mounted inlets to measure concentrations internally. A PICARRO G2401-m measured CO_2, CH_4, and CO at 0.4 Hz resolution (Digangi et al., 2021) using a modified Rosemount total air temperature probe gas inlet (Buck Research Instruments, LLC) mounted on the crown collocated with the aerosol inlets (Fig. 6a). These measurements were calibrated hourly during flight with a 1-minute single point calibration and weekly during deployments on the ground with a three-point calibration, with all standards traceable to WMO X2019 (CO_2), WMO X2004A (CH_4), and WMO X2014A (CO) scales. Some data from the PICARRO were omitted due to inlet leaks predominantly at high altitude (i.e., RF1-9 on 14-27 February 2020). O_3 was measured at 0.5 Hz by a 2B Technologies Inc. O_3 monitor (Model 205) using a forward-facing J-probe inlet mounted on the Falcon nadir panel and relied on a custom sampling apparatus to enhance data quality at high altitude (Wei et al., 2021). O_3 data were zeroed for 1 minute with a KI filter hourly in-flight to account for baseline drifts to ensure high data quality, and the monitor was calibrated before and after each deployment with a NIST-traceable standard (Model 305, 2B Technologies Inc.). The O_3 data are vulnerable to altitude/pressure dependence that is accounted for based on these routine calibrations, but it is cautioned that there could be residual effects about which interested data users can consult the instrument team. Details about instrument team contact information are discussed in sect. 7.

The trace gas mixing ratios can be used in conjunction with back-trajectory analysis to link air masses to source regions and can also be used in studies of wet scavenging and aqueous production as both CO and CH_4 can be considered conserved tracer species. For example, CO and CH_4 are well correlated with a similar relative enhancement ratio for much of the ACTIVATE dataset, consistent with the hypothesis that the observed air was influenced by urban emissions with relative pollutant levels dependent on the degree of dilution. However, there were occasionally periods where the enhancement factor differed, with CO enhancements much greater than CH_4 in relation to the typical enhancement ratios during the campaign. This is consistent with less efficient forms of combustion, such as biomass burning, with incidences of this observed briefly during several flights when near the coast and for longer segments offshore during two flights, RF28 (26 August 2020) and RF38 (23 September 2020). Enhancement ratios of O_3 and CO also can be used effectively to infer chemical information about the airmass. One example is early during the Winter 2022 deployment (Jan-Feb) when O_3 and CO were inversely correlated, consistent with NO_x titration of O_3 in a VOC-limited chemistry regime. As the flights moved farther toward spring, this correlation became weaker (March), then reversed to become a roughly positive correlation between the species (May/June). This is consistent with the switch to a NO_x-limited regime of O_3 photochemistry as VOC emissions increase with the warmer temperatures and the growth of MBL heights further diluting the anthropogenic NO_x emissions; this highlights another unique advantage of the routine, long-duration measurements of the ACTIVATE dataset.

4.3 Fast-response three dimensional winds and state parameters

High resolution in situ measurements of three dimensional winds (u, v, w components), temperature and pressure were obtained using the Turbulent Air Motion Measurement System (TAMMS) (Thornhill et al., 2003). The system has been installed on the NASA P-3 for over 20 years. This is the first time it was integrated onto the NASA HU-25. The raw data were recorded between 100 and 200 Hz with a UEIPAC-300 real time controller (United Electronics Industries, Inc.) and then averaged down to 20 Hz for archiving and analysis work. Five flush-mounted ports (0.417 cm diameter) were positioned in a cruciform pattern on the nose of the HU-25 in order to not have any interference in the airflow around the aircraft. The angle of attack was derived from the vertically positioned ports whereas the slideslip angle was obtained from the horizontally aligned ports. The center tap was a backup for the dynamic (impact) pressure measurement. High time resolution and high precision pressure transducers (Honeywell PPT-2 and Rosemount) were placed as close as possible to the pressure ports to minimize time delays.

Whereas the five-port pressure system helps determine the speed of the air relative to the aircraft, the speed of the aircraft relative to the earth was obtained with inertial/GPS data measured via the Applanix 610. Aircraft velocity components are a blended solution using the inertial and GPS data via a Kalman filtering technique (e.g., Brunke et al., 2022). The u and v components are zonal and meridional, respectively, while w is the vertical wind speed (positive is upwards). The three dimensional winds are computed using the full version of the well-established air motion equations (Lenschow, 1986).

The total air temperature, from which the ambient air temperature and true airspeed were calculated, was measured by the non-deiced version of the Rosemount Model 102 total air temperature sensor with a fast-response sensing element (E102E4AL, > 5 Hz response). The pressures (total, static, and impact (dynamic)) were obtained with a Rosemount pressure transducer and a Rosemount Micro Air Data Transducer (model 2014MA1A) that was tied into the co-pilot's pressure port to minimize the pressure defect. An ancillary measurements of the infrared (IR) surface temperature was also included in the TAMMS instrument suite of measurements. IR surface temperature was obtained from a downlooking Heitronics KT-15 Infrared Thermometer.

Multiple dedicated calibration flights during each deployment year were performed in order to establish the primary calibration coefficients necessary to ensure the highest data quality. Calibrations were done at different altitudes above the boundary layer in clean homogenous air masses to determine:

- Angle of attack slope and offset – via speed variations
- Sideslip slope – via crabbing the HU-25 with wings level
- Pressure defect – via along wind reverse headings
- Heading offset (sideslip offset) – via cross wind reverse headings

These calibration results were then applied to the final data along with any time lag adjustments (Brunke et al., 2022). The Applanix data were also post-processed to reduce the velocity and position errors. The error in positioning for the final data was reduced to less than 1 m. The calibration data were repeatable from year to year and allowed for a final and consistent set of calibration coefficients to be utilized for all the variables except for the heading offset. That value changed between deployments due to the removal and re-installation of the Applanix on the HU-25.

There are several caveats that a potential user should be aware of prior to using these data. For the three-dimensional winds, users should nominally restrict use to times when the HU-25 is flying straight and level as significant changes in pitch, roll, and altitude can introduce artifacts and noise into the winds calculation. If non-straight/level times are needed for analysis, users are advised to consult with the TAMMS instrument team and at the very least look at the data in great detail to look for correlations with pitch or roll that are adversely influencing the derived winds. In addition, care should be taken when averaging the horizontal winds as the averaging should be done to the u and v components and then the wind speed and direction should be recomputed post averaging. When looking at fine scale details such as turbulent fluxes via eddy correlation or the average updraft velocity under clouds, users are advised to consider using time windows that overlap by 50% in order to increase statistics. The time window length should be sufficiently long to capture all the eddy sizes that contribute to the turbulent fluxes. Assuming the typical ACTIVATE leg length of 3 minutes and an average airspeed of 100 m s^{-1}, a segment of 512 samples can resolve eddy sizes of up to 1.28 km and if not overlapped then 7 full segments can be averaged together to compute the average turbulent fluxes. If the suggested overlap of 50% is used then 13 full segments can be averaged together to increase statistics significantly.

4.4 Aerosol characterization

In situ measurements of aerosol properties were conducted with the Langley Aerosol Research Group Experiment (LARGE) instrument package used in previous NASA campaigns such as Studies of Emissions and Atmospheric Composition, Clouds and Climate Coupling by Regional Surveys ($SEAC^4RS$) (Toon et al., 2016) and the Cloud, Aerosol and Monsoon Processes

Philippines Experiment ($CAMP^2Ex$) (Reid et al., 2023). The majority of aerosol measurements were conducted with instruments integrated inside the fuselage and air provided by two manually-switched inlets mounted on the Falcon's exterior crown (top of Fig. 6a). An isokinetic Clarke-style shrouded solid double diffuser inlet (Brechtel Manufacturing Inc. [BMI]) was relied on during cloud-free scenes for aerosol characterization (Mcnaughton et al., 2007) whereas a counterflow virtual impactor (CVI; BMI) was used while in clouds (Shingler et al., 2012) for measurements of droplet residual particles (i.e., particles remaining after droplet evaporation). An inlet flag data product is archived indicating which inlet (i.e., the CVI or the isokinetic inlet) was used at a given time for the HR-ToF-AMS and LAS instruments (described below), whereas all other LARGE instruments summarized in this section only sampled downstream of the isokinetic inlet. Those instruments that are not switched to the CVI require in-cloud filtering to remove periods potentially biased by droplet shattering artifacts (discussed in sect. 4.4.5). The upper-size limit for all bulk observations (unless otherwise noted below) is governed by the isokinetic inlet performance (Mcnaughton et al., 2007) with a nominal cutoff point at 5 µm diameter (Table 5); note though that this cutoff diameter is for ambient RH conditions while the final in situ aerosol measurements will be more representative of dried (and thus smaller particles) conditions owing to heating during inlet transmission. All LARGE measurements are archived at 1 Hz time resolution (unless otherwise noted) and at standard temperature and pressure (STP; 273.15 K and 1013.25 mb). The LARGE measurements can be categorized into optical, microphysical, and chemical, which are described in order next.

4.4.1 Optical

Dry scattering and absorption coefficients were measured at three wavelengths using a nephelometer (TSI Inc. Model 3563; 450, 550, 700 nm) (Ziemba et al., 2013) and a particle soot absorption photometer (PSAP; Radiance Research; 470, 532, 660 nm) (Mason et al., 2018), respectively. Scattering coefficient measurements have been corrected for angular truncation (Anderson and Ogren, 1998) and absorption coefficients were corrected using guidance from Virkkula (2010). A measurement of aerosol hygroscopic growth factor, f(RH), was calculated in the form of the ratio of total light scattering at high and low RH. Scattering measurements were made by two independent nephelometers in parallel; one at low RH (i.e., generally less than 40%) and one at high RH (controlled targeting 85%) using a custom Nafion humidifier (Ziemba et al., 2013). These measurements allow calculation of the hygroscopicity gamma parameter, which is then used with the dry scattering coefficient to calculate scattering at any RH up to saturation. The f(RH) data archived are calculated specifically between 20% and 80% RH. f(RH) is only reported for conditions when 550 nm scattering coefficients (at both high and low RH) exceeded 5.0 Mm^{-1} and controlled RH was between 72% and 92%.

A 1 µm cyclone was utilized upstream of both nephelometers for 2021-2022 flights and thus the scattering coefficients and f(RH) represent submicrometer aerosol in contrast to PSAP data, which represent bulk aerosol; the nephelometer data in 2020 correspond to an upper cutoff point of 5 µm. For the 2021-2022 datasets, we recommend using FCDP microphysical data (which are measured at ambient RH and described in sect. 4.5) and Mie Theory assumptions to calculate ambient extinction for the supermicrometer particle population. The scattering and absorption coefficient data are used to compute secondary properties including scattering and absorption Angstrom exponents and single scattering albedo (SSA) discussed in sect. 4.4.4.

4.4.2 Microphysical

Total N_a was measured with two independent condensation particle counters (CPCs). One CPC was sensitive to all particles with diameter greater than 3 nm (TSI Inc. Model 3776) and the other only to particles with diameter greater than 10 nm (TSI Inc. Model 3772). The difference in number concentration between the two CPCs is informative about ultrafine, and presumably newly formed, particles between 3 and 10 nm for data users interested in research into particle nucleation (Corral et al., 2022b). Non-volatile particle concentrations (for particles with diameter greater than 10 nm) were recorded by an additional Model 3772 CPC that was coupled to a 350° C thermodenuder. The CPC concentrations are useful for assessing the evolution of the full aerosol population, for understanding particles sources and formation processes, and to provide "closure" checks on the integrated size distribution data.

Dry aerosol size distributions are measured by different instruments for varying diameter windows. The ultrafine/Aitken-mode window between 3-100 nm diameter is measured with a scanning mobility particle sizer (SMPS; Model 3085 DMA, Model 3776 CPC, and Model 3088 Neutralizer; TSI Inc.), which classifies particles based on their electrical mobility diameters. The accumulation-mode diameter window extending from 100 to 5000 nm is captured based on optical diameters using a laser aerosol spectrometer (LAS, TSI Inc. Model 3340) (Froyd et al., 2019). The LAS was calibrated using mono-disperse ammonium sulfate particles (i.e., with a refractive index of 1.52) to optimize relevance to ambient aerosol particles (Shingler et al., 2016), and both sizing instruments were spot-checked frequently to ensure long-term stability using NIST-traceable polystyrene latex spheres at appropriate sizes. Independent empirical size-dependent corrections have been applied to both the SMPS and LAS datasets that allow "stitching" the distributions at 100 nm; excellent closure is demonstrated for most ambient conditions by adding integrated SMPS and LAS number concentrations compared to total CPC concentrations. A demonstration of this is provided in Fig. 7 for RF12 on 29 February 2020. While the LAS provides 1 Hz data, the SMPS data are at lower time resolution (~45 s) and require caution to interpret when concentrations are rapidly changing in-flight. Droplet residual LAS particle size distributions are archived (using the inlet flag) during CVI in-cloud sampling periods. Interpretation of these data has not been demonstrated previously but should provide supplementary information to compositional analysis towards improving our understanding of cloud processing. The LAS-CVI data require the use of the InletFlag (0 = isokinetic; 1 = CVI) for separation of the two categories of data.

Cloud condensation nuclei (CCN) concentrations and spectra for submicrometer particles were measured with a CCN spectrometer (Droplet Measurement Technologies [DMT] Inc.) using both constant and scanning flow techniques (Moore and Nenes, 2009). The reported CCN concentration depends on the instrument supersaturation, which is also reported in the data files. For the 2020 dataset, the instrument supersaturation was linearly scanned between approximately 0.2-0.7% supersaturation with a single upscan or downscan consisting of 60 seconds. For the 2021 and 2022 datasets, the instrument supersaturation was held constant at approximately 0.4% supersaturation for each flight. Data users are encouraged to consult the data files for the precise, calibrated instrument supersaturation corresponding to each data point.

4.4.3 Chemical

Non-refractory mass concentrations of sulfate, nitrate, ammonium, chloride, organics, and numerous mass spectral markers (mass-to-charge ratio [m/z] 42, 43, 44, 55, 57, 58, 60, 79, 91) were measured by a High Resolution Time of Flight Aerosol Mass Spectrometer (HR-ToF-AMS; Aerodyne) (Decarlo et al., 2008). The nominal vacuum aerodynamic diameter window of the AMS was 60 to 600 nm. As summarized for ACTIVATE already (Dadashazar et al., 2022a), the 1 Hz fast-MS mode AMS data were averaged to 30 s time resolution for the data archive. A brief overview of what types of species the aforementioned m/z mass spectral markers represent is as follows: 42 (amines, $C_2H_4N^+$), 43 (mixed hydrocarbons, $C_3H_7^+$ or $C_2H_3O^+$), 44 (oxidized hydrocarbons, CO_2^+), 55 (aliphatic hydrocarbons, $C_4H_7^+$), 57 (aliphatic hydrocarbons, $C_4H_9^+$), 58 (sea salt/marine, $NaCl^+$), 60 (biomass burning, $C_2H_4O_2^+$), 79 (methanesulfonate/marine, $CH_3SO_2^+$), 91 (aromatic hydrocarbons, C_7H_7). The AMS is operated using a custom pressure-controlled inlet (at 500 torr) and all mass concentrations are reported at STP. The overall AMS ionization efficiency was calibrated using mono-disperse 400 nm ammonium nitrate particles throughout the 3-year measurement period, and a collection efficiency value of unity was applied to all data based on comparison to simultaneously measured PILS-based sulfate mass concentrations. AMS-CVI data are reported in separate files as compared to other AMS data from cloud-free air sampling. The AMS-CVI data include only relative mass fractions. The CVI was extensively characterized previously by Shingler et al. (2012), with a demonstration of the utility of AMS-CVI data during ACTIVATE provided by Dadashazar et al. (2022a).

Water-soluble ionic composition was measured by a particle-into-liquid sampler (PILS; BMI) coupled to offline ion chromatography (Sorooshian et al., 2006; Crosbie et al., 2020). The time resolution varied between 5 and 7 minutes depending on the deployment. The PILS data represent bulk aerosol between approximately 50 and 5000 nm, including the following ions: anions = chloride, nitrite, bromide, nitrate, sulfate, oxalate; cations = sodium, ammonium, dimethylamine, potassium, magnesium, calcium. Details of the ion chromatography instrument and analysis methods for anion and cation speciation are provided in recent ACTIVATE studies (Corral et al., 2022a; Gonzalez et al., 2022). The PILS was operated without denuders and thus users should account for this aspect of the data when interpreting concentrations for semi-volatile species such as ammonium for which there may be positive biases due to gas-phase contributions.

4.4.4 Secondary aerosol products

The archived "optical" and "microphysical" files are useful starting points for data users interested in summary statistics and special calculated parameters. For example, the "optical" files include data for submicrometer dry scattering (450, 550, 700 nm) and calculated extinction (532 nm) coefficients, total aerosol absorption coefficient (470, 532, 660 nm), f(RH) and its associated gamma parameter at 550 nm, aerosol scattering (450/700 nm) and absorption (470/660 nm) Angstrom Exponents, and SSA (at 450, 550, 700 nm). Note that the submicrometer designation applies to 2021-2022 flights and that 2020 flights correspond to bulk aerosol (< 5 μm). The extinction parameter was calculated by summing submicrometer scattering and bulk absorption, with scattering data at 550 nm adjusted to 532 nm using the measured Angstrom Exponent. Since scattering is typically the dominant component of extinction and absorption is assumed to be dominated by brown carbon and black carbon in continental outflow, archived optical properties calculated using a combination of nephelometer and PSAP measurements (i.e., extinction coefficient and SSA) should be treated as representing submicrometer aerosol. Care should be taken for cases suspected to be influenced by absorbing dust, which do not satisfy the assumptions above. The gamma parameter allows one to estimate scattering at any RH (Ziemba et al., 2013); scattering coefficient, extinction coefficient, scattering Angstrom Exponent, and SSA are all provided in archived files at ambient RH. Note that ambient scaling assumes that there is no absorption enhancement due to humidification, since we do not have the necessary information regarding the particle mixing state to calculate those enhancements accurately. The “microphysical” files provide the CPC concentrations along with sub- and supermicrometer number, surface area, and volume concentrations from the LAS with the assumption of spherical particles. During data processing, additional filters are applied to the 1 Hz data such as thresholding and smoothing to obtain secondary products such as SSA, which can introduce gaps that do not exist in the raw data. Caution should be taken when averaging ratio-based values such as SSA as this can introduce unrealistic values in the data.

4.4.5 Data usage notes

Additional notes on data usage are provided here with the reminder that data users should always also consult with ICARTT data file headers (files described more in sect. 7) for guidance on data usage. Mass loadings and concentrations are all reported at standard temperature and pressure. Conversion factors at 1 Hz resolution are provided in the ICARTT data files for data users interested to convert the data back to ambient temperature and pressure conditions. The latter step is important for users aiming to compare in situ data to remote sensing data because the remote sensors retrieve information at ambient conditions.

Aerosol measurements are vulnerable to contamination due to cloud droplet shatter on the sampling inlet when aircraft fly in clouds or precipitation below a cloud; this usually is manifested in unrealistically high particle number concentrations often with high-frequency variability as measured by either of the CPCs. It is recommended that data users use strict criteria to only use aerosol data in cloud-free conditions. As one example, a recent ACTIVATE study used aerosol data only when cloud liquid water content (LWC) was less than 0.001 g m^{-3} (Schlosser et al., 2022). However, users concerned about more confidently separating cloud hydrometeors from coarse aerosol should consult with instrument teams operating the probes described in sect. 4.5 and/or develop the types of analyses (e.g., joint histograms) that compare different variables like LWC and N_d to see more clearly where clusters emerge for coarse aerosol and how to better separate them from cloud droplets (see Fig. 2 of Schlosser et al., 2022).

Since it is a differencing technique, the AMS can produce negative mass concentrations in clean conditions which should be retained in statistical calculations whenever possible. Removal of such points during a level leg for instance can positively bias the resulting value for the leg averaged value.

Owing to the relatively long time resolution of the PILS (5-7 min) and the ‘smearing’ of data without step function responses in composition (Crosbie et al., 2020), data users should use caution with how the data are used for their applications. More specifically, PILS data are unreliable for vertically-resolved depictions of ionic composition due to the short amount of time spent during most level legs during ACTIVATE (~3 min) and the fact that spiral and slant profiles were usually shorter than the time needed to collect a PILS sample. In contrast, the data are well-suited for statistical assessments of concentrations and chemical ratios relying on many flights of data as demonstrated by Hilario et al. (2021).

4.5 Wing-mounted probes (aerosol and cloud droplet size distributions)

Four optical probes were used to characterize aerosol and cloud droplet size distributions extending from 0.5 to 1465 μm. All such data are reported at ambient conditions (temperature, pressure, RH), which requires caution when trying to compare these aerosol data to dry aerosol measurements described in sect. 4.4. A DMT Cloud Droplet Probe (CDP; 2-50 μm) was mounted on the crown of the aircraft fuselage, while a Cloud and Aerosol Spectrometer probe (CAS; 0.5-50 μm) was mounted on the starboard wing (Fig. 6a). Both instruments measure the scattered light pulses as coarse mode aerosol particles and cloud droplets pass through a laser beam, where the count rate and light intensity are related to the particle number and size, respectively. Particle concentration is computed by multiplying the measured count rate by a sample volume that is the product of the probe sample area and the aircraft true airspeed (TAS). The CDP sample area was experimentally measured by DMT to be 0.323 mm^2, while an assumed sample area for the CAS of 0.25 mm^2 was used. In addition, cloud liquid water content (LWC), effective variance, and effective radius were calculated assuming spherical particles with unit density. The CAS is able to measure particles between 0.5-2 μm but its shrouded inlet may make the instrument susceptible to in-cloud droplet shatter, unlike the open path CDP. The CAS data are archived at 1 Hz, while the CDP data are archived at >= 1 Hz depending on the deployment. For 2020, it was observed that 1 Hz data made it hard to distinguish cloud centers and edges, so the data sampling rate was increased for subsequent years of flights.

On the port side wing (Fig. 6a) was a Fast Cloud Droplet Probe (FCDP; 3-50 μm) and a Two-Dimensional Stereo (2D-S; 29-1465 μm), both of which are manufactured by SPEC Inc. The FCDP is a forward scattering probe with a rapid sampling rate of 25 ns to enable single particle detection for all particles. Its fast electronics and other features like a small pinhole for coincidence reduction imply lower uncertainties in particle sizing and counting (Baumgardner et al., 2017; Kirschler et al., 2022; Kleine et al., 2018; Knop et al., 2021; Voigt et al., 2021). Archived FCDP data include aerosol and droplet number size distributions, LWC, effective diameter, and median volume diameter. Extensive processing and corrections to the FCDP data are described in Kirschler et al. (2022). Meanwhile, the CDP and CAS data have not been similarly corrected to date, which may introduce biases particularly for high cloud droplet number environments exceeding 500 cm^{-3} (Lance, 2012).

The Two-Dimensional Stereo (2D-S) optical array probe from SPEC Inc. relies on 128 photodiodes to produce shadow images of single particles (Lawson and Baker, 2006; Lawson et al., 2019). Archived 2D-S data include cloud number size distributions for liquid/ice/total, liquid and ice water content, ice flag, effective diameter for liquid/ice/total, median volume diameter for liquid and total. 2D-S images are provided on request, which can be illustrative of hydrometeor shapes (liquid droplets versus ice) and coarse aerosol types such as bioaerosols. The probe has two identical arms that are perpendicular with 785 nm wavelength lasers associated with each to generate a diffraction pattern for traversing particles. The recorded ensemble of ‘slices’ obtained rapidly by triggered photodiodes help generate 2D images of particles (Knollenberg, 1970). The 2D-S used on the Falcon is described in detail by Kirschler et al. (2022), who note that with the fast response time of 41 ns, the 2D-S has less uncertainty for characterizing spheroids, and is in the middle of the range for ice particles, compared to other optical array probes (Baker and Lawson, 2006; Gurganus and Lawson, 2018; Lawson and Baker, 2006; Bansmer et al., 2018). For data users interested in stitching together 2D-S size distributions with the other probes like FCDP, the method discussed by Kirschler et al. (2022) is a suitable option to confront the overlap of the two probes between 16-51.3 µm. They did an overlap calculation for the diameter space between the lower FCDP bin bound at 27 µm and the higher 2D-S bin bound at 39.9 µm. Linear interpolation can be applied using the next 2D-S bin and proportionality between the last FCDP bin and the new 2D-S bin. Examples of FCDP and 2D-S data products are shown in sect. 6 for a representative case flight.

In terms of data usage notes, a few factors should be considered by users:

- Consider that the scattered light spectrometers in use are designed for cloud measurements and uncertainties increase in the case of aerosol measurements. For instance, the sizing for these probes is calibrated assuming water droplets with a corresponding refractive index; thus, if coarse mode dust, biological particles, and/or sea salt particles are present, there will be sizing biases due to the varying refractive indices and possible aspherical shapes of these aerosol types relative to water droplets.
- The use of the 2D-S horizontal arm is preferable, as the vertical arm did not operate properly in all flights and was disabled in those cases. The data locations are marked accordingly in the vertical arm.
- If the particle size distributions of the FCDP and 2D-S shall be combined, it is recommended not to make the transition above 30 µm, because the measurement area difference of the instruments increases quadratically with size and causes a non-negligible statistical difference, which can manifest itself in unfilled size bins.
- Precipitation particles occur in a considerably lower number than ordinary cloud droplets and accordingly the statistics in abundance are lower for the 2D-S in this case, which is reflected in an increased measurement uncertainty. This should be accounted for when comparing in-situ precipitation measurements with remote sensing platforms and models.

4.6 Cloud water composition

A special aspect of ACTIVATE was the focus on cloud water measurements due to the extensive amount of time the Falcon spent in clouds. Cloud water samples were also collected using the Axial Cyclone Cloud water Collector (AC3), which was characterized and described in detail by Crosbie et al. (2018). The AC3 was mounted on the Falcon’s exterior crown close to the CVI (top of Fig. 6a). The AC3 extracted cloud water from the air stream when the aircraft was in cloud. A shutter was used at the inlet of the AC3 when the Falcon was out of cloud to reduce contamination. Cloud water was collected by vacuum through a Teflon sampling line inside the Falcon and deposited in 15 mL HDPE centrifuge tubes. Samples were stored in a refrigerator post-flight and then analyzed subsequently with ion chromatography (IC), a pH meter, and inductively coupled plasma mass spectrometry (ICP-MS). Owing to varying liquid volume in each sample vial, the top priority was IC analysis, followed by ICP-MS, and finally pH. The variable volume was due to different periods of time the aircraft was in cloud per vial, varying amounts of cloud LWC during sample collection, and other AC3 performance factors (Crosbie et al., 2018). For context, 70% (90%) of the 535 total vials were collected within 6 minutes (13 minutes).

The details of the three analytical methods used at the University of Arizona and quality control details such as collection of sample blanks are described elsewhere for interested readers (Corral et al., 2022a; Gonzalez et al., 2022; Stahl et al., 2021). The IC was able to speciate and quantify the following ions in order of elution: anions = glycolate, acetate, formate, methanesulfonate, pyruvate, glyoxylate, chloride, nitrite, bromide, nitrate, glutarate, adipate, succinate, maleate, sulfate, oxalate, phthalate; cations = sodium, ammonium, dimethylamine, potassium, magnesium, calcium. ICP-MS elements detected include: Li, Be, B, Na, Mg, Al, S, Cl, K, Ca, Ti, V, Cr, Mn, Fe, Co, Ni, Cu, Zn, Ge, As, Br, Rb, Sr, Y, Zr, Nb, Mo, Ru, Rh, Pd, Ag, Cd, Sn, Sb, Te, I, Cs, Ba, Ce, Hf, Ta, W, Re, Os, Ir, Pt, Au, Hg, Tl, Pb, Th, U.

Cloud water species concentrations from the IC and ICP-MS are reported in aqueous units (mg L^{-1}), and for conversion to air equivalent units (μg m^{-3}) data users can apply their own specific criteria. For context, past ACTIVATE studies have conducted the conversion with knowledge of cloud LWC as derived from the FCDP by using the average LWC during periods of sample collection when LWC exceeded a threshold of 0.02 g m^{-3} (Corral et al., 2022a; Gonzalez et al., 2022). Aqueous concentrations can be multiplied by the aforementioned mean LWC value during sample collection divided by the density of water. In environments dominated by broken and more vertically developed cumulus clouds, cloud water in edges or tenuous clouds is ineffectively captured. To combat this, Crosbie et al. (2022) used a threshold of 0.1 g m^{-3} and provide a sensitivity analysis for combining cloud water with microphysical data.

4.7 Forward camera imagery

Depending on the application of Falcon data, forward camera imagery can be critical to visually determine the conditions the aircraft was flying through at a given time. Camera details were already discussed in sect. 3.6 and summarized in Table 4. All videos start based on the takeoff times listed in Table 2 and continue until the landing time. However, a significant number of the files end before landing (sometimes up to 15 minutes) due to the fact that the last file did not close properly once the power was turned off. The files were recorded at 2 second resolution for 2020 and 1 second for 2021 and 2022.

4.8 Merge files

Specific to the Falcon aircraft are “merge files” on the publicly available data archive (sect. 7) that are created at different time resolutions of interest (e.g., 1, 5, 10, 15, 30, 60 s, or matching an individual data product start and stop times). The aim of these files is to accommodate data analysis efforts by synthesizing different time resolutions among instruments in the aircraft payload as well as sampling location. An online merge tool puts different in situ datasets on a common time base using weighted time averages of each dataset. The final archived time base can either be a time series with constant interval between points or based on an individual dataset's time stamps. The merge tool accounts for data points that have missing or limit of detection data codes by skipping over them to not bias the resultant values. The merge files have been converted into netCDF file format (.nc) at 1 s and 60 s time resolutions for 2020 (2021 and 2022 forthcoming) to be more conducive to modelling and analysis applications by providing more machine-actionable metadata as well as metadata provided by individual instrument teams. We caution that it is difficult to consider any version of the merge files as "final" due to the potential for instrument PIs to submit new data sometimes months or even years after flights are completed. However, once new data are submitted, the merge files are typically generated within a month.

5 Complementary data products

5.1 Flight reports

Each individual flight has an archived flight report drafted and reviewed by flight scientists and pilots, which can serve as a useful resource for data users aiming to learn more about special features in a particular flight. A caveat is that these reports incorporate notes from scientists and pilots during flight without any post-flight data analysis to provide extra evidence for certain documented features such as sources of dust or biomass burning. It is recommended to consult these files and the "special notes" column of Table 2 to see if relevant details are provided fitting a particular interest for a data user such as instances of mixed-phase clouds, satellite underflights, or air mass types of interest like dust or biomass burning. Of particular importance in the flight reports is inclusion of flight tracks overlaid on satellite imagery to show cloud conditions.

5.2 Falcon flight leg index files

The repeated nature of stairstepping legs flown by the Falcon motivated the need for a way to identify leg types as a function of time. This can aid in analysis of data across multiple flights focused on statistics as a function of leg type. To address this, an individual file was generated per flight day that the Falcon flew identifying 14 different leg types with start and stop times per leg in flight (i.e., a single file contains two flights for double flight days). Ten digit indices are provided describing the deployment number, flight number, flight type (process study versus statistical survey), leg type, ensemble number, and ensemble type (cloud-free or cloud). The 14 leg types identified include (see also Fig. 2): takeoff and landing, transit leg (usually after takeoff and before landing), ACB, BCB, BCT, ACT, MinAlt, Ascent, Descent, Slant/Spiral (i.e., dedicated soundings covering a significant vertical distance beyond what ascents and descents cover during typical stairstepping), BBL, ABL, RS, Other (any other leg not defined otherwise). It is important to note that leg types are assigned based on the intention of the leg as determined by the flight scientist and not a description of the data that was collected during that period. For example, an ACB leg could have been flown in a region of scattered cloud above the nominal bases yet resulted in no cloud penetrations. Also, process study flights with numerous legs at different levels in cloud may have the legs between ACB and BCT called "Other" (e.g., RF173 on 11 June 2022) and in some cases two legs very close to cloud top can be called BCT such as RF13 on 1 March 2020 (Fig. 3b). We caution that the usage of these leg files is ideal for analyses depending on large amounts of statistics but that for more detailed case studies and/or for higher confidence of legs in or out of cloud for a certain percentage of time of the leg it is important to look at as much data as possible to best understand the environmental conditions during a typical leg. An example of why this is important is for leg types in the immediate vicinity of clouds owing to the sometimes low cloud fraction and the changing structure of clouds, including sometimes multiple layers of clouds. For applications requiring high confidence in where a plane was relative to clouds, forward camera videos (Table 4) are very helpful.

5.3 Aircraft collocation product

To address the challenge of geographical and temporal collocation for two separate measurement platforms, a data collocation product (i.e., collocation mask) is available. This product is broadly applicable for any research where data from a secondary platform are required to be within some required spatio-temporal difference with the primary platform. To accommodate different needs, data files are archived when considering either the King Air or the Falcon as the primary platform.

Within the contents of each file are the primary platform's 1 Hz time series and collocated secondary platform time segments along with the corresponding horizontal distance (in km) between each aircraft at each time segment. A collocated time segment is one where the secondary platform is nearest to the primary platform within 15 km and 30 minutes. If there are multiple separate time segments, that means there were points where the two platforms flew outside of 15 km and back within the 30-minute time segment. Each period was checked, and the nearest collocated time stamp is provided with the corresponding horizontal separation (in km) between the platforms. There are a maximum of 10 collocated segments allowed for each 1 second time step. This product will be described in greater detail in forthcoming work (Schlosser et al., in review).

5.4 Cloud detection neural network algorithm

Above-aircraft clouds impact the downwelling and upwelling radiation fields by the King Air aircraft, and thus impact the measurements of airborne passive sensors and their retrieval products, such as the retrieved aerosol and cloud optical and microphysical products. For ACTIVATE, the forward-facing camera on the King Air (sect. 3.6) was used to create a manual cloud mask product indicating whether or not a cloud is present above the aircraft. In order to automate this process, the cloud detection neural network (CDNN) algorithm was developed to detect above-aircraft clouds efficiently and automatically using the camera images. The CDNN uses convolutional neural networks to find clouds using forward-viewing camera images. A center-top crop of the forward-facing camera's field of view is used to identify clouds closer in proximity to the aircraft. However, this crop may not be fully optimized such that clouds that are too far away to impact passive sensors onboard the aircraft may still be flagged as contaminated by above-aircraft clouds. Also, clouds that are not directly visible in the forward-facing camera, such as above-aircraft clouds behind the aircraft that are nonetheless blocking the sun, are unable to be detected.

The description of the CDNN, its performance, and the resulting archived ACTIVATE cloud mask product results are detailed in Nied et al. (2023).

5.5 MERRA-2 data along flight tracks

The Modern-Era Retrospective analysis for Research and Applications, version 2 (MERRA-2) (Gelaro et al., 2017) is NASA's latest reanalysis generated with the Goddard Earth Observing System, version 5 (GEOS-5) atmospheric data assimilation system (Rienecker, 2008). It has a horizontal resolution of 0.5˚ × 0.625˚ with 72 vertical levels from the surface to 0.01 hPa. Its aerosol reanalysis (Buchard et al., 2017; Randles et al., 2017) uses the GEOS-5 Goddard Aerosol Assimilation System (Buchard et al., 2015), which utilizes the Goddard Chemistry, Aerosol, Radiation, and Transport model (GOCART) (Chin et al., 2002) to simulate 15 externally mixed aerosol tracers: hydrophobic and hydrophilic black carbon (BC) and organic carbon (OC), dust (five size bins), sea salt (five size bins), and sulfate. GOCART includes wind speed-dependent emissions for dust and sea salt, fossil fuel combustion, biomass burning and biofuel emissions for primary sulfate and carbonaceous aerosols, and additional biogenic sources for organic carbon. Secondary sulfate is formed by chemical oxidation of SO_2 and DMS. Volcanic SO_2 emissions are included. The major sinks for aerosol particles are gravitational settling, dry deposition, and wet removal due to stratiform and convective precipitation. MERRA-2 assimilates AOD from ground and satellite-based remote sensing sensors, including the Advanced Very High Resolution Radiometer (AVHRR), the Aerosol Robotic Network (AERONET), the Multi-angle Imaging Spectroradiometer (MISR), and the Moderate Resolution Imaging Spectroradiometer (MODIS/Terra and MODIS/Aqua). MERRA-2 aerosol data have been evaluated by Randles et al. (2017) for AODs and by Buchard et al. (2017) for aerosol vertical distribution and absorption.

We have archived a data product that samples MERRA-2 for selected 3-D fields along the Falcon flight tracks during the ACTIVATE deployments (Table 6). We interpolate the original MERRA-2 three hour instantaneous 3-D fields to the latitude, longitude, and pressure altitude of the aircraft every 60 seconds along the flight track. Data files for February-March and August-September 2020 are archived and the product files for subsequent years are being generated for archival at the same location (details of accessibility in sect. 7). These sampled MERRA-2 data facilitate the comparison between aircraft measurements and reanalysis and provide quantities that are not measured during ACTIVATE (such as SO_2 concentration; Corral et al., 2022b). They are also useful for doing statistical analysis of aircraft in-situ data in comparison with reanalysis as well as model evaluation.

5.6 FLEXPART back trajectory products

The Lagrangian transport and dispersion model, FLEXPART (FLEXible PARTicle dispersion model, https://www.flexpart.eu/) (Pisso et al., 2019; Eckhardt, 2008), is used to simulate transport pathways of air masses associated with ACTIVATE aircraft measurements. In its backward mode, FLEXPART calculates trajectories of a multitude of particles and simulates advection, convection, and turbulent dispersion of the particles during the transport period. Detailed descriptions about FLEXPART transport schemes and parameterizations can be found in the literature (Eckhardt, 2008; Zhang et al., 2014).

All FLEXPART simulations were driven by the Global Forecast System Analysis (GFS-ANL 003, 1˚ × 1˚, 26 levels, 3 hourly; https://www.ncei.noaa.gov/data/global-forecast-system/access/grid-003-1.0-degree/analysis). FLEXPART version 9.2 was used for the ACTIVATE February-March and August-September 2020 deployments. For 2021 and 2022 campaigns, FLEXPART v10.4 (Pisso et al., 2019) was used to accommodate the recent upgrade in the GFS-ANL data as well as to gain better capacity in simulating turbulence in the boundary layer. The purpose of this simulation series is to depict general transport pathways from a large-scale perspective. Model configurations here (e.g., output frequency, boundary layer turbulence) are not prioritized for small-scale analysis. The FLEXPART trajectory products for both 2020 and 2021 campaigns are now available to assist with the analyses of aerosol sources and aging history associated with aircraft measurements; 2022 files are forthcoming.

In the FLEXPART backward mode, a plume of passive particles is released from the aircraft location and advected and dispersed backwards in time. For each 60-second merged aircraft measurement every 10 minutes, FLEXPART initiates 10,000 passive particles at the sampling location and calculates backwards for 10 days. The released particles represent the air masses (plume) intercepted by the aircraft. For a completed backward simulation, the total residence time (RT) of the plume in a given 1°×1° grid cell can be calculated by summing the time duration of all particles that have been resident in the cell during the 10-day transport. If a large fraction of particles passes through a surface grid cell multiple times, the grid cell would accumulate a long residence time, and emissions therein would have a large contribution to the plume intercepted by the aircraft. The horizontal distribution of vertically integrated residence times (Fig. 8a) can be readily used to determine a trajectory-like transport pathway, while the vertical distribution of RT (Fig. 8b) can clearly indicate plume transport height and acquisition of surface emissions.

For each of the six ACTIVATE deployment periods, two types of files can be found in the ACTIVATE data. One type includes trajectory plots associated with aircraft data of every 10 minutes. For each trajectory, a map plot and a vertical plot of RT distributions are included. Examples are shown in Fig. 8 for aircraft measurements at 19:22 UTC during the second flight of 1 March 2020 that is discussed in more detail in sect. 6. These plots are generated for quick-look purpose to visualize transport pathways, and the plot quality is thus constrained to limit total file size.

The other file type includes original FLEXPART output for 10-day backward trajectories released every 10 minutes along flight tracks. Each netCDF file contains gridded specific residence time (RT, "s m^3 kg^{-1}") of all released particles. RT is saved in such a unit instead for time ("s") so that it can be easily multiplied by any upwind source / emission ("kg m^{-3} s^{-1}") to calculate source contributions affecting the receptor point. For example, FLEXPART RT can be used to calculate a time series of tracer concentrations at the receptor contributed by a certain emission source (e.g., anthropogenic or biomass burning) by multiplying the residence time in the lowest 300 m by the emission flux.

Uncertainties in transport pathways simulated by FLEXPART can be due to the parameterizations representing temporally and spatially unresolved transport processes (Stohl et al., 2010). In terms of vertical transport processes, boundary layer mixing and convective updrafts are both treated in FLEXPART using information from the driving meteorology. Time-varying planetary boundary layer (PBL) height determines the vertical mixing of air parcels. In FLEXPART, PBL height is calculated using the Richardson number concept based on the wind and temperature fields (Vogelezang and Holtslag, 1996). Another highly parameterized sub-grid process is cloud convection. FLEXPART redistributes air parcels vertically in convection-activated grids using the approach of Emanuel and Živković-Rothman (1999), which determines air parcel displacement in up- and down-drafts based on temperature and humidity fields. Model results with such schemes have been tested and validated using surface and in situ measurements (Brioude et al., 2013; Stohl et al., 1998).

5.7 MODIS, GOES-16, MERRA-2

To assist data analysis efforts for ACTIVATE that can benefit from contextual satellite and reanalysis data for overlapping and prior time periods, various satellite and reanalysis data products are archived with a common format and spatial resolution. The dataset is comprised of products generated at 2 spatial resolutions: 1˚ × 1˚ and 2 km (satellite pixel resolution). 1˚ × 1˚ data correspond to aerosol and cloud properties derived from MODIS Aqua (Level 3 product), paired with MERRA-2 meteorological parameters re-gridded to the same resolution. Satellite pixel-level cloud properties are from the Advanced Baseline Imager (ABI) on the 16^{th} Geostationary Operational Environmental Satellite (GOES-16), with continuous spatiotemporal sampling of the ACTIVATE domain. While the Level 3 products are intended for understanding the large-scale and climatological features of the study region, the pixel-level GOES-16 retrievals are valuable for monitoring the spatiotemporal evolution of the cloud fields during research flights. Merged satellite-reanalysis daily files combine 3D meteorological fields from MERRA-2 (already described in sect. 5.5) with daytime aerosol and cloud properties derived from MODIS on Aqua (~ 1:30 pm overpass time) for the January 2009-July 2022 period and the domain defined by the 84.5˚W-30.5˚W, 10.5˚N-59.5˚N box. MODIS cloud retrievals are taken from the Cloud and the Earth's Radiant Energy System (CERES) Edition 4 (Minnis et al., 2021) level 3 Single Scanner Footprint (SSF1deg-Day), gridded at 1˚ × 1˚ resolution. CERES-MODIS cloud properties in the merged file are cloud amount, cloud effective pressure, cloud effective temperature, cloud effective height, cloud particle effective radius (ice and liquid) derived using the 3.7 μm channel, water path (ice and liquid), cloud optical depth, and liquid cloud droplet number concentration estimated following Painemal (2018). MODIS aerosol optical depths (Levy et al., 2013) at 1˚ × 1˚ resolution for 7 wavelengths (0.47 μm, 0.55 μm, 0.66 μm, 0.86 μm, 1.24 μm, 1.63 μm, and 2.13 μm) are obtained from the MODIS Level 3 Atmospheric Gridded Product Collection 6 (MYD08_D3). Examples of ACTIVATE applications of this dataset include climatological characterization of the atmospheric circulation and cloud field (Painemal et al., 2021), assessment of the meteorological factors that modulate clouds and aerosol variability and their implications for aerosol-cloud interactions (Dadashazar et al., 2021b), and description of the synoptic-scale processes that give rise to boundary layer cloud variability (Painemal et al., 2023).

MERRA-2 meteorological parameters at 0.625˚ × 0.5˚ resolution are spatially collocated with MODIS via nearest neighbor interpolation. We selected MERRA-2 products at 18:00 UTC as it is the closest match to the Aqua overpass time for the northwest Atlantic. In addition, 15 isobaric levels are stored, corresponding to (units of hPa): 1000, 975, 950, 925, 900, 875, 850, 825, 800, 775, 750, 725, 700, 650, 600. MERRA-2 3D fields (longitude × latitude × vertical level) include: air temperature, RH, sea level pressure, edge heights, eastward wind, northward wind, vertical pressure velocity; and 2D fields (at a fixed vertical level) are: surface skin temperature, 2-m eastward wind, 2-m northward wind, and lifting condensation level.

Cloud retrievals GOES-16 ABI are derived using the NASA Satellite ClOud and Radiation Property System (SatCORPS) algorithms (Minnis et al., 2008; Minnis et al., 2021). SatCORPS algorithms have been adapted from those for CERES-MODIS to take advantage of radiometric channels similar to those of MODIS and other Earth-orbiting satellites (Minnis et al., 2021). Additional consistency between MODIS and GOES-16 is achieved by calibrating GOES-16 visible radiance against its Aqua-MODIS counterpart following Doelling et al. (2018). GOES-16 cloud retrievals are produced every 20 minutes during the ACTIVATE deployment. Files are archived for two regions covering the ACTIVATE flight tracks: a small domain (78˚W-60˚W, 29˚N-46˚N), and a large domain (93˚W-49˚W, 18˚N-55˚N). Cloud properties for the small domain are produced at the native resolution of the infrared channels, that is, 2 km at nadir. For the large domain, 2-km cloud properties are subsampled every other pixel to achieve a spatial resolution of 4 km. Cloud products derived from GOES-16 include cloud mask and phase, temperature, height and pressure, particle effective radius (ice and liquid), water path (ice and liquid), and optical depth. The ability of GOES-16 products of resolving the diurnal cycle at a relatively high spatial resolution makes the retrievals particularly useful for describing the evolution of the cloud fields during the research flights (GOES-16 snapshots are included in the flight reports described in Sect. 5.1). GOES-16 products have been used in the context of ACTIVATE for validating mesoscale simulations of clouds (Chen et al., 2022b), assessing the evolution of liquid water path in large eddy simulation (LES) experiments (Li et al., 2022), and for quantifying the cloud-top entrainment rate and its role in the CCN budget (Tornow et al., 2022). In addition, GOES-16 retrievals are well suited for matching with the aircraft tracks to complement in-situ observations, and for Lagrangian studies.

6 Case flight example

The afternoon joint flight on 1 March 2020 is highly representative of the majority of the ACTIVATE flight dataset in terms of how the aircraft flew and the science that was targeted. This section aims to share representative data collected to summarize how the aforementioned data products in Sections 3-5 can be visualized and used; this day of flights was also summarized during an open data workshop that was recorded and archived at https://asdc.larc.nasa.gov/news/activate-data-webinar-materials. While this flight was a canonical type of ACTIVATE flight due to it being a statistical survey, the actual conditions presented qualified this as an excellent flight day as anticipated from the weather forecasting meeting on the previous day. This is because of forecasted cold air outbreak (CAO) indicators of boundary layer instability (Papritz et al., 2015; Painemal et al., 2021; Fletcher et al., 2016) coinciding with strong, cold, northwesterly winds and "cloud streets" (Dadashazar et al., 2021b). The day was forecasted also to have high cloud fraction and no high level cirrus and mid-tropospheric cloud layers that would negatively impact remote sensing objectives. Forecasting analysis conducted the previous day suggested there would be a broken to overcast low cloud deck (deepening to the east) with a western edge moving farther offshore throughout the day. GEOS forward processing data hinted at fairly low aerosol loading, with increasing sea salt concentrations offshore. Actual conditions were consistent with forecasted information.

The first joint flight of 1 March 2020 was a process study flight (Fig. 3a) since the aircraft transited to an area of high interest and conducted maneuvers deviating from the ensemble approach shown in Fig. 2. More specifically, the Falcon conducted stacked level legs (a "wall") approximately perpendicular to the estimated boundary layer winds while the King Air flew a large circle encompassing the wall location followed by an overpass of the extended axis of the Falcon wall. This particular flight has also been simulated and discussed in recent studies (Chen et al., 2022a; Li et al., 2022; Tornow et al., 2022). Both aircraft returned to the base of operations (Newport News) to refuel and then returned to the same region as the morning, flying a downwind survey that started at the wall center point and extended as far as fuel permitted (Fig. 9a). The downwind survey leg allowed for a semi-Lagrangian characterization of the air mass evolution and also resampled the air mass from the morning flight. Both flights captured elements of the cloud morphology common to CAOs, but the afternoon flight characterized the evolution from the upwind clear region to scattered cumulus transforming into a thicker and more extensive layer before finally transitioning into open-cellular stratocumulus organization. This can be seen from flight tracks overlaid on GOES-16 visible imagery (Fig. 9a).

Shown already in Fig. 8 were FLEXPART simulation results pertaining to air mass trajectories arriving at the point of the Falcon during this flight at 19:22 UTC. Figure 10 shows the level of detail possible with dropsondes, with the markings of where the two were launched shown in Fig. 9a with nadir camera imagery from the King Air at those times in Fig. 9b. Representative data from the HSRL-2 in the form of vertical 'curtains' of aerosol backscatter as a function of flight time are shown in Fig. 9c; these data show higher aerosol loading is located in the MBL closest to the ocean surface. This panel shows the altitude of the Falcon while flying below the King Air aircraft as well as the locations where the dropsondes were launched from the King Air.

Figure 11 summarizes selected variables measured by the Falcon in time series format. The dashed vertical black bars denote the beginning of either clear or cloud ensembles. The first ensemble begins right after the high altitude transit after takeoff and was a clear ensemble with the following legs in order (MinAlt, ABL, BBL, RS, MinAlt). That ensemble was followed by three consecutive cloud ensembles with the first two containing the nominal order of legs described in sect. 2.2 while the third ensemble was truncated at MinAlt owing to the absence of clouds, which is clearly visible in Fig. 9a with clear conditions closer to the coast. The vertical gray shaded bars make use of leg index files (sect. 5.2) and distinguish the two level-leg types in cloud including ACB (above cloud base) and BCT (below cloud top). Clearly those periods are marked by enhancements in N_d and LWC as measured by the FCDP, but note that cloud penetrations also occur outside of designated cloud legs, such as during altitude transitions. Many of the other plotted variables associated with trace gases, aerosol particles, temperature, and wind data show interesting structure that at least partly have dependence on aircraft altitude, which can be teased out in these forms of multi-panel time series depictions as in Fig. 11 that can aid data users. Aerosol microphysical data have been screened to remove data collected in clouds and, in the case of the LAS (which was used to determine number concentration above 100 nm), using the inlet flag variable to remove CVI data from this illustration. Note that AMS data are archived separately for isokinetic and CVI time periods, so this screening is not necessary for the AMS. An important note with the aerosol composition data is that the PILS data for Na^+, used here as a proxy for sea salt that the AMS cannot provide, have coarser time resolution than the AMS. Also, some PILS data may potentially include influence from cloud periods and thus may not be suitable for certain applications. If data users want aerosol data without any cloud contamination, they should only use PILS data in cloud-free areas such as clear ensembles and transit periods. For interested readers, a figure analogous to Fig. 7 is shown in Fig. S1 for this case flight too to demonstrate again how to conduct closure types of analyses between different data parameters such as aerosol number concentration in this case.

Lastly, Fig. 12 provides a summary of cloud probe products specifically from the FCDP and 2D-S combination probe from the Falcon's port side wing. Figure 12a shows a time series of cloud droplet size distributions from the FCDP combined with 2D-S. Sections with cloud penetrations are clearly visible with enhanced number concentrations above 10 µm. Also evident from the time series are periods with noticeable number concentrations below 10 µm during periods without clouds, which is indicative of coarse aerosol particles such as sea salt. Figure 12b shows various forms of size distributions that data users can produce from FCDP alone, in addition to the 2D-S/FCDP combination and 2D-S horizontal ice and liquid products. The stitched size distribution for 2D-S/FCDP was explained briefly in sect. 4.5 and described more extensively by Kirschler et al. (2022). The 2D-S imagery in Fig. 12c covers a 20 second period that nicely represents a broad variety of large particle shapes, including liquid droplets and rimed ice particles.

7 Data/code availability and file format

NASA's Atmospheric Science Data Center (ASDC) plays a key role in data curation, dissemination, and long-term preservation of ACTIVATE data. It archives the latest versions of publication quality data, including observational, derived, and value-added data products. It also houses contextual information to facilitate data use by the research community at large, in addition to documentation for maintaining reprocessing capability and openness. Digital Object Identifiers (DOIs) are assigned at both the project-level and data product (collection) level for ACTIVATE. All data from the King Air and Falcon, including complementary data products from sect. 5, unless otherwise stated, are publicly archived on ASDC's Distributed Active Archive Center (DAAC; ACTIVATE Science Team, 2020) and accessible through the ACTIVATE landing page: https://asdc.larc.nasa.gov/project/ACTIVATE, with each data file containing data from one flight or one calendar day. Various tabs at that webpage include different data products (collections) with their unique DOI codes, which are summarized in Table 7 along with other resources described in this paper. The open data workshop content listed in Table 7 is especially important to guide new data users through each step of the process to access and visualize data beginning with establishing a free account at earthdata.nasa.gov and then proceeding to download ACTIVATE data with the Sub-Orbital Order Tool (SOOT; https://asdc.larc.nasa.gov/soot/power-user). ACTIVATE data are also available to download via Earthdata Search: https://search.earthdata.nasa.gov/search?fpj=ACTIVATE.

Most files are in a special format called ICARTT files (Northup et al., 2017), which is traditionally used by NASA and other agencies for airborne data. Falcon in-situ observations are reported in ICARTT format, while remote sensing data uses a combination of ICARTT format and HDF format. It is critical for any data user aiming to use airborne science data to review the ICARTT file headers that provide guidance for how to both use and interpret data from individual instruments.

File names constitute the following details in order: campaign, instrument, sampling method, start date, revision number, and the (optional) end date. Publication-quality data include a revision number in their file name (R0+) and are time synced to the platform time standard (DLH instrument time for Falcon and GPS time for King Air). The contents of each ICARTT file include data notes in a README tab including contact information for the instrument data (i.e., instrument principal investigator [PI] name and data manager [DM]), PI institution, campaign name, start date of data collection, the most recent data revision date, the number of variables, data flags, instrument details and description of the data, and revision log. The revision log lists the identifier of the current data revision and lists the previous revisions and their relative status. Each instrument will have its own unique column headers based on what was being measured.

While the instrument teams have time synchronized datasets with one another to account for different sampling techniques (e.g., varying times for sample air to travel from an inlet to instruments), it is possible that a variation of a few seconds can occur. No post-submission time alignment is done by the data management team, merge process, or ASDC DAAC and thus data users should use diligence when using multiple datasets together to do some intercomparisons and confirm temporal variations of related parameters match one another without obvious systematic shifts.

8 Conclusions

A collection of airborne datasets is introduced here that serves as a resource for investigations of aerosol-cloud-meteorology interactions, along with studies more interested in measurements of exclusively just trace gases, aerosol particles, clouds, precipitation, and/or atmospheric state parameters. The datasets cover the northwest Atlantic extending from the coastal area of the mid-Atlantic states and New England to much farther offshore around the vicinity of Bermuda where more remote marine conditions are present that are less perturbed by continental emissions. The data span all seasons with collection periods between November-June and August-September for 2020 through 2022. This paper is a potential user's guide to availability and access of ACTIVATE data products. Of particular interest to most data users of the Falcon data is likely the merged dataset of variables generated at different time resolutions of interest (e.g., 1, 5, 10, 15, 30, 60 s, or matching an individual data product start and stop times). Data products and codes have also been developed to help users for joint analysis of data between the two aircraft based on specific criteria of interest related to time and space separation.

Appendix A: Summary of abbreviations

Abbreviation	Definition
2D-S	Two-Dimensional Stereo
ABI	Advanced Baseline Imager

ABL	Above boundary layer top
AC3	Axial cyclone cloud water collector
ACB	Above cloud base
ACE-ENA	Aerosol and Cloud Experiments in the Eastern North Atlantic
ACT	Above cloud top
ACTIVATE	Aerosol Cloud meTeorology Interactions oVer the western ATlantic Experiment
AERONET	Aerosol Robotic Network
AMS	Aerosol mass spectrometer
AOD	Aerosol optical depth
ASDC	Atmospheric Science Data Center
ASTER	Advanced Spaceborne Thermal Emission and Reflection Radiometer
AVAPS	Airborne Vertical Atmospheric Profiling System
AVHRR	Advanced Very High Resolution Radiometer
BBL	Below boundary layer top
BC	Black carbon
BCB	Below cloud base
BCT	Below cloud top
BLEACH	Bermuda boundary Layer Experiment on the Atmospheric Chemistry of Halogens
BMI	Brechtel Manufacturing Inc.
CALIPSO	Cloud-Aerosol Lidar and Infrared Pathfinder Satellite Observations
CAMP2Ex	Cloud, Aerosol and Monsoon Processes Philippines Experiment
CAO	Cold air outbreak
CAS	Cloud and aerosol spectrometer
CCN	Cloud condensation nuclei
CDNN	Cloud detection neural network
CDP	Cloud droplet probe
CERES	Cloud and the Earth’s Radiant Energy System
CH4	Methane
CN	Condensation nuclei
CO	Carbon monoxide
CO2	Carbon dioxide
CPC	Condensation particle counter
CVI	Counterflow virtual impactor
DAAC	Distributed Active Archive Center
DJF	December-January-February
DLH	Diode laser hygrometer
DM	Data manager
DMT	Droplet Measurement Technologies
DOI	Digital object identifier

EVS-3	Earth venture suborbital - 3
f(RH)	Ratio of total light scattering between high and low RHs
FCDP	Fast cloud droplet probe
FLEXPART	FLEXible PARTicle dispersion model
GEOS-5	Goddard Earth Observing System, version 5
GOCART	Goddard Chemistry, Aerosol, Radiation, and Transport model
GOES	Geostationary Operational Environmental Satellite
GPS	Global positioning system
H2O(v)	Water vapor
HDF	Hierarchical data format
HSRL-2	High Spectral Resolution Lidar - generation 2
IC	Ion chromatography
ICARTT	International Consortium for Atmospheric Research on Transport and Transformation
ICP-MS	Inductively coupled plasma mass spectrometry
IMPACTS	Investigation of Microphysics and Precipitation for Atlantic Coast-Threatening Snowstorms
IR	Infrared
JJA	June-July-August
LaRC	Langley Research Center (NASA)
LARGE	Langley Aerosol Research Group Experiment
LAS	Laser Aerosol Spectrometer
LES	Large eddy simulation
LWC	Liquid water content
MAE	Mean absolute error
MAPE	Mean absolute percentage error
MBL	Marine boundary layer
MERRA-2	Modern-Era Retrospective analysis for Research and Applications, version 2
MinAlt	Minimum altitude the Falcon can fly at
MISR	Multi-angle Imaging Spectroradiometer
MLH	Mixed-layer height
MODIS	Moderate Resolution Imaging Spectroradiometer
Na	Aerosol particle number concentration
NAAMES	North Atlantic Aerosols and Marine Ecosystems Study
NASA	National Aeronautics and Space Administration
NCAR	National Center for Atmospheric Research
Nd	Cloud droplet number concentration
netCDF	Network Common Data Form
NOx	Nitrogen oxides
O3	Ozone
OC	Organic carbon

ODR	Orthogonal distance regression
OTREC	Organization of Tropical East Pacific Convection
PBL	Planetary boundary layer
PILS	Particle-into-liquid sampler
PI	Principal investigator
PPT	Precision pressure transducers
PSAP	Particle soot absorption photometer
RF	Research flight
RH	Relative humidity
RS	Remote sensing
RSP	Research scanning polarimeter
RT	Residence time
SatCORPS	Satellite ClOud and Radiation Property System
SEAC4RS	Studies of Emissions and Atmospheric Composition, Clouds and Climate Coupling by Regional Surveys
SMPS	Scanning mobility particle sizer
SO2	Sulfur dioxide
SOOT	Sub-Orbital Order Tool
SSA	Single scattering albedo
SSF	Single Scanner Footprint
STP	Standard temperature and pressure
TAMMS	Turbulent Air Motion Measurement System
TAS	True airspeed
UTC	Coordinated Universal Time
VIIRS	Visible Infrared Imaging Radiometer Suite
VOC	Volatile organic compound

Author contributions

Conceptualization, resources, funding acquisition, supervision: AS, JWH, RCF, XZ

Writing – original draft preparation: AS

Project administration: MK

Data curation: GC, JMK, KEP, MEB, MAS, NJ, SL

Formal analysis, investigation, methodology, software, validation, visualization: All authors

Writing - reviewing and editing: All authors

Competing interests

The authors declare that they have no conflict of interest.

Disclaimer

Publisher's note: Copernicus Publications remains neutral with regard to jurisdictional claims in published maps and institutional affiliations.

Acknowledgements

The authors thank pilots and aircraft maintenance personnel of NASA Langley Research Services Directorate for successful execution of ACTIVATE flights. The work was funded by ACTIVATE, a NASA Earth Venture Suborbital-3 (EVS-3) investigation funded by NASA's Earth Science Division and managed through the Earth System Science Pathfinder Program Office.

Financial support

University of Arizona investigators were supported by the National Aeronautics and Space Administration grant no. 80NSSC19K0442. C.V. and S.K. thank funding by the Deutsche Forschungsgemeinschaft (DFG, German Research Foundation) – TRR 301 – Project-ID 428312742 and SPP 1294 HALO under contract VO 1504/7-1. National Institute of Aerospace investigators were supported by NASA grant 80NSSC19K0389. J.S.S. was supported by an appointment to the NASA Postdoctoral Program at NASA Langley Research Center, administered by Oak Ridge Associated Universities under contract with NASA. University of Miami gratefully acknowledges financial support through NASA grant 80NSSC19K0390. The Pacific Northwest National Laboratory (PNNL) is operated for DOE by Battelle Memorial Institute under contract DE-AC05-76RLO1830.

References

ACTIVATE Science Team: Aerosol Cloud meTeorology Interactions oVer the western ATlantic Experiment Data [dataset], doi.org/10.5067/SUBORBITAL/ACTIVATE/DATA001, 2020.

Adebiyi, A. A., Zuidema, P., Chang, I., Burton, S. P., and Cairns, B.: Mid-level clouds are frequent above the southeast Atlantic stratocumulus clouds, Atmos. Chem. Phys., 20, 11025-11043, 10.5194/acp-20-11025-2020, 2020.

Aldhaif, A. M., Lopez, D. H., Dadashazar, H., Painemal, D., Peters, A. J., and Sorooshian, A.: An Aerosol Climatology and Implications for Clouds at a Remote Marine Site: Case Study Over Bermuda, Journal of Geophysical Research: Atmospheres, 126, e2020JD034038, https://doi.org/10.1029/2020JD034038, 2021.

Alexandrov, M. D., Cairns, B., and Mishchenko, M. I.: Rainbow Fourier transform, Journal of Quantitative Spectroscopy and Radiative Transfer, 113, 2521-2535, https://doi.org/10.1016/j.jqsrt.2012.03.025, 2012a.

Alexandrov, M. D., Cairns, B., Emde, C., Ackerman, A. S., and van Diedenhoven, B.: Accuracy assessments of cloud droplet size retrievals from polarized reflectance measurements by the research scanning polarimeter, Remote Sensing of Environment, 125, 92-111, https://doi.org/10.1016/j.rse.2012.07.012, 2012b.

Alexandrov, M. D., Cairns, B., Sinclair, K., Wasilewski, A. P., Ziemba, L., Crosbie, E., Moore, R., Hair, J., Scarino, A. J., Hu, Y., Stamnes, S., Shook, M. A., and Chen, G.: Retrievals of cloud droplet size from the research scanning polarimeter data: Validation using in situ measurements, Remote Sensing of Environment, 210, 76-95, https://doi.org/10.1016/j.rse.2018.03.005, 2018.

Anderson, T. L. and Ogren, J. A.: Determining Aerosol Radiative Properties Using the TSI 3563 Integrating Nephelometer, Aerosol Science and Technology, 29, 57-69, 10.1080/02786829808965551, 1998.

Avey, L., Garrett, T. J., and Stohl, A.: Evaluation of the aerosol indirect effect using satellite, tracer transport model, and aircraft data from the International Consortium for Atmospheric Research on Transport and Transformation, Journal of Geophysical Research: Atmospheres, 112, https://doi.org/10.1029/2006JD007581, 2007.

Baker, B. and Lawson, R. P.: Improvement in Determination of Ice Water Content from Two-Dimensional Particle Imagery. Part I: Image-to-Mass Relationships, Journal of Applied Meteorology and Climatology, 45, 1282-1290, 10.1175/jam2398.1, 2006.

Bansmer, S. E., Baumert, A., Sattler, S., Knop, I., Leroy, D., Schwarzenboeck, A., Jurkat-Witschas, T., Voigt, C., Pervier, H., and Esposito, B.: Design, construction and commissioning of the Braunschweig Icing Wind Tunnel, Atmos. Meas. Tech., 11, 3221-3249, 10.5194/amt-11-3221-2018, 2018.

Baumgardner, D., Abel, S. J., Axisa, D., Cotton, R., Crosier, J., Field, P., Gurganus, C., Heymsfield, A., Korolev, A., Krämer, M., Lawson, P., McFarquhar, G., Ulanowski, Z., and Um, J.: Cloud Ice Properties: In Situ Measurement Challenges, Meteorological Monographs, 58, 9.1-9.23, 10.1175/amsmonographs-d-16-0011.1, 2017.

Behrenfeld, M. J., Moore, R. H., Hostetler, C. A., Graff, J., Gaube, P., Russell, L. M., Chen, G., Doney, S. C., Giovannoni, S., Liu, H. Y., Proctor, C., Bolalios, L. M., Baetge, N., Davie-Martin, C., Westberry, T. K., Bates, T. S., Bell, T. G., Bidle, K. D., Boss, E. S., Brooks, S. D., Cairns, B., Carlson, C., Halsey, K., Harvey, E. L., Hu, C. M., Karp-Boss, L., Kleb, M., Menden-Deuer, S., Morison, F., Quinn, P. K., Scarino, A. J., Anderson, B., Chowdhary, J., Crosbie, E., Ferrare, R., Haire, J. W., Hu, Y. X., Janz, S., Redemann, J., Saltzman, E., Shook, M., Siegel, D. A., Wisthaler, A., Martine, M. Y., and Ziemba, L.: The North Atlantic Aerosol and Marine Ecosystem Study (NAAMES): Science Motive and Mission Overview, Front Mar Sci, 6, 2019.

Bellouin, N., Quaas, J., Gryspeerdt, E., Kinne, S., Stier, P., Watson-Parris, D., Boucher, O., Carslaw, K. S., Christensen, M., Daniau, A.-L., Dufresne, J.-L., Feingold, G., Fiedler, S., Forster, P., Gettelman, A., Haywood, J. M., Lohmann, U., Malavelle, F., Mauritsen, T., McCoy, D. T., Myhre, G., Mülmenstädt, J., Neubauer, D., Possner, A., Rugenstein, M., Sato, Y., Schulz, M., Schwartz, S. E., Sourdeval, O., Storelvmo, T., Toll, V., Winker, D., and Stevens, B.: Bounding Global Aerosol Radiative Forcing of Climate Change, Reviews of Geophysics, 58, e2019RG000660, https://doi.org/10.1029/2019RG000660, 2020.

Brioude, J., Arnold, D., Stohl, A., Cassiani, M., Morton, D., Seibert, P., Angevine, W., Evan, S., Dingwell, A., Fast, J. D., Easter, R. C., Pisso, I., Burkhart, J., and Wotawa, G.: The Lagrangian particle dispersion model FLEXPART-WRF version 3.1, Geosci. Model Dev., 6, 1889-1904, 10.5194/gmd-6-1889-2013, 2013.

Brunke, M. A., Cutler, L., Urzua, R. D., Corral, A. F., Crosbie, E., Hair, J., Hostetler, C., Kirschler, S., Larson, V., Li, X.-Y., Ma, P.-L., Minke, A., Moore, R., Robinson, C. E., Scarino, A. J., Schlosser, J., Shook, M., Sorooshian, A., Lee Thornhill, K., Voigt, C., Wan, H., Wang, H., Winstead, E., Zeng, X., Zhang, S., and Ziemba, L. D.: Aircraft Observations of Turbulence in Cloudy and Cloud-Free Boundary Layers Over the Western North Atlantic Ocean From ACTIVATE and Implications for the Earth System Model Evaluation and Development, Journal of Geophysical Research: Atmospheres, 127, e2022JD036480, https://doi.org/10.1029/2022JD036480, 2022.

Buchard, V., da Silva, A. M., Colarco, P. R., Darmenov, A., Randles, C. A., Govindaraju, R., Torres, O., Campbell, J., and Spurr, R.: Using the OMI aerosol index and absorption aerosol optical depth to evaluate the NASA MERRA Aerosol Reanalysis, Atmos. Chem. Phys., 15, 5743-5760, 10.5194/acp-15-5743-2015, 2015.

Buchard, V., Randles, C. A., da Silva, A. M., Darmenov, A., Colarco, P. R., Govindaraju, R., Ferrare, R., Hair, J., Beyersdorf, A. J., Ziemba, L. D., and Yu, H.: The MERRA-2 Aerosol Reanalysis, 1980 Onward. Part II: Evaluation and Case Studies, J Clim, 30, 6851-6872, 10.1175/jcli-d-16-0613.1, 2017.

Burton, S. P., Ferrare, R. A., Hostetler, C. A., Hair, J. W., Rogers, R. R., Obland, M. D., Butler, C. F., Cook, A. L., Harper, D. B., and Froyd, K. D.: Aerosol classification using airborne High Spectral Resolution Lidar measurements – methodology and examples, Atmos. Meas. Tech., 5, 73-98, 10.5194/amt-5-73-2012, 2012.

Burton, S. P., Hostetler, C. A., Cook, A. L., Hair, J. W., Seaman, S. T., Scola, S., Harper, D. B., Smith, J. A., Fenn, M. A., Ferrare, R. A., Saide, P. E., Chemyakin, E. V., and Müller, D.: Calibration of a high spectral resolution lidar using a Michelson interferometer, with data examples from ORACLES, Appl. Opt., 57, 6061-6075, 10.1364/AO.57.006061, 2018.

Cairns, B., Russell, E., LaVeigne, J., and Tennant, P.: Research scanning polarimeter and airborne usage for remote sensing of aerosols, Optical Science and Technology, SPIE's 48th Annual Meeting, SPIE2003.

Chen, J., Wang, H., Li, X., Painemal, D., Sorooshian, A., Lee Thornhill, K., Robinson, C., and Shingler, T.: Impact of Meteorological Factors on the Mesoscale Morphology of Cloud Streets during a Cold Air Outbreak over the Western North Atlantic, Journal of the Atmospheric Sciences, 10.1175/jas-d-22-0034.1, 2022a.

Chen, J., Wang, H., Li, X., Painemal, D., Sorooshian, A., Thornhill, K. L., Robinson, C., and Shingler, T.: Impact of Meteorological Factors on the Mesoscale Morphology of Cloud Streets during a Cold-Air Outbreak over the Western North Atlantic, Journal of the Atmospheric Sciences, 79, 2863-2879, 10.1175/jas-d-22-0034.1, 2022b.

Chin, M., Ginoux, P., Kinne, S., Torres, O., Holben, B. N., Duncan, B. N., Martin, R. V., Logan, J. A., Higurashi, A., and Nakajima, T.: Tropospheric Aerosol Optical Thickness from the GOCART Model and Comparisons with Satellite and Sun Photometer Measurements, Journal of the Atmospheric Sciences, 59, 461-483, 10.1175/1520-0469(2002)059<0461:Taotft>2.0.Co;2, 2002.

Chowdhary, J., Cairns, B., and Travis, L. D.: Contribution of water-leaving radiances to multiangle, multispectral polarimetric observations over the open ocean: bio-optical model results for case 1 waters, Appl. Opt., 45, 5542-5567, 10.1364/AO.45.005542, 2006.

Christensen, M. W., Gettelman, A., Cermak, J., Dagan, G., Diamond, M., Douglas, A., Feingold, G., Glassmeier, F., Goren, T., Grosvenor, D. P., Gryspeerdt, E., Kahn, R., Li, Z., Ma, P. L., Malavelle, F., McCoy, I. L., McCoy, D. T., McFarquhar, G., Mülmenstädt, J., Pal, S., Possner, A., Povey, A., Quaas, J., Rosenfeld, D., Schmidt, A., Schrödner, R., Sorooshian, A., Stier, P., Toll, V., Watson-Parris, D., Wood, R., Yang, M., and Yuan, T.: Opportunistic experiments to constrain aerosol effective radiative forcing, Atmos. Chem. Phys., 22, 641-674, 10.5194/acp-22-641-2022, 2022.

Corral, A. F., Braun, R. A., Cairns, B., Gorooh, V. A., Liu, H., Ma, L., Mardi, A. H., Painemal, D., Stamnes, S., van Diedenhoven, B., Wang, H., Yang, Y., Zhang, B., and Sorooshian, A.: An Overview of Atmospheric Features Over the Western North Atlantic Ocean and North American East Coast – Part 1: Analysis of Aerosols, Gases, and Wet Deposition Chemistry, Journal of Geophysical Research: Atmospheres, 126, e2020JD032592, https://doi.org/10.1029/2020JD032592, 2021.

Corral, A. F., Choi, Y., Collister, B. L., Crosbie, E., Dadashazar, H., DiGangi, J. P., Diskin, G. S., Fenn, M., Kirschler, S., Moore, R. H., Nowak, J. B., Shook, M. A., Stahl, C. T., Shingler, T., Thornhill, K. L., Voigt, C., Ziemba, L. D., and Sorooshian, A.: Dimethylamine in cloud water: a case study over the northwest Atlantic Ocean, Environmental Science: Atmospheres, 10.1039/D2EA00117A, 2022a.

Corral, A. F., Choi, Y., Crosbie, E., Dadashazar, H., DiGangi, J. P., Diskin, G. S., Fenn, M., Harper, D. B., Kirschler, S., Liu, H., Moore, R. H., Nowak, J. B., Scarino, A. J., Seaman, S., Shingler, T., Shook, M. A., Thornhill, K. L., Voigt, C., Zhang, B., Ziemba, L. D., and Sorooshian, A.: Cold Air Outbreaks Promote New Particle Formation Off the U.S. East Coast, Geophysical Research Letters, 49, e2021GL096073, https://doi.org/10.1029/2021GL096073, 2022b.

Cox, C. and Munk, W.: Measurement of the Roughness of the Sea Surface from Photographs of the Sun's Glitter, J. Opt. Soc. Am., 44, 838-850, 10.1364/JOSA.44.000838, 1954.

Crosbie, E., Brown, M. D., Shook, M., Ziemba, L., Moore, R. H., Shingler, T., Winstead, E., Thornhill, K. L., Robinson, C., MacDonald, A. B., Dadashazar, H., Sorooshian, A., Beyersdorf, A., Eugene, A., Collett Jr, J., Straub, D., and Anderson, B.: Development and characterization of a high-efficiency, aircraft-based axial cyclone cloud water collector, Atmos. Meas. Tech., 11, 5025-5048, 10.5194/amt-11-5025-2018, 2018.

Crosbie, E., Shook, M. A., Ziemba, L. D., Anderson, B. E., Braun, R. A., Brown, M. D., Jordan, C. E., MacDonald, A. B., Moore, R. H., Nowak, J. B., Robinson, C. E., Shingler, T., Sorooshian, A., Stahl, C., Thornhill, K. L., Wiggins, E. B., and Winstead, E.: Coupling an online ion conductivity measurement with the particle-into-liquid sampler: Evaluation and modeling using laboratory and field aerosol data, Aerosol Science and Technology, 54, 1542-1555, 10.1080/02786826.2020.1795499, 2020.

Crosbie, E., Ziemba, L. D., Shook, M. A., Robinson, C. E., Winstead, E. L., Thornhill, K. L., Braun, R. A., MacDonald, A. B., Stahl, C., Sorooshian, A., van den Heever, S. C., DiGangi, J. P., Diskin, G. S., Woods, S., Bañaga, P., Brown, M. D., Gallo, F., Hilario, M. R. A., Jordan, C. E., Leung, G. R., Moore, R. H., Sanchez, K. J., Shingler, T. J., and Wiggins, E. B.: Measurement report: Closure analysis of aerosol–cloud composition in tropical maritime warm convection, Atmos. Chem. Phys., 22, 13269-13302, 10.5194/acp-22-13269-2022, 2022.

Dadashazar, H., Corral, A. F., Crosbie, E., Dmitrovic, S., Kirschler, S., McCauley, K., Moore, R., Robinson, C., Schlosser, J. S., Shook, M., Thornhill, K. L., Voigt, C., Winstead, E., Ziemba, L., and Sorooshian, A.: Organic enrichment in droplet residual particles relative to out of cloud over the northwestern Atlantic: analysis of airborne ACTIVATE data, Atmos. Chem. Phys., 22, 13897-13913, 10.5194/acp-22-13897-2022, 2022a.

Dadashazar, H., Alipanah, M., Hilario, M. R. A., Crosbie, E., Kirschler, S., Liu, H., Moore, R. H., Peters, A. J., Scarino, A. J., Shook, M., Thornhill, K. L., Voigt, C., Wang, H., Winstead, E., Zhang, B., Ziemba, L., and Sorooshian, A.: Aerosol Responses to Precipitation Along North American Air Trajectories Arriving at Bermuda, Atmos. Chem. Phys., 2021, 1-34, 10.5194/acp-2021-471, 2021a.

Dadashazar, H., Crosbie, E., Choi, Y., Corral, A. F., DiGangi, J. P., Diskin, G. S., Dmitrovic, S., Kirschler, S., McCauley, K., Moore, R. H., Nowak, J. B., Robinson, C. E., Schlosser, J., Shook, M., Thornhill, K. L., Voigt, C., Winstead, E. L., Ziemba, L. D., and Sorooshian, A.: Analysis of MONARC and ACTIVATE Airborne Aerosol Data for Aerosol-Cloud Interaction Investigations: Efficacy of Stairstepping Flight Legs for Airborne In Situ Sampling, Atmosphere, 13, 1242, 10.3390/atmos13081242, 2022b.

Dadashazar, H., Painemal, D., Alipanah, M., Brunke, M., Chellappan, S., Corral, A. F., Crosbie, E., Kirschler, S., Liu, H., Moore, R. H., Robinson, C., Scarino, A. J., Shook, M., Sinclair, K., Thornhill, K. L., Voigt, C., Wang, H., Winstead, E., Zeng, X., Ziemba, L., Zuidema, P., and Sorooshian, A.: Cloud drop number concentrations over the western North Atlantic Ocean: seasonal cycle, aerosol interrelationships, and other influential factors, Atmos. Chem. Phys., 21, 10499-10526, 10.5194/acp-21-10499-2021, 2021b.

Davis, K. J., Gamage, N., Hagelberg, C. R., Kiemle, C., Lenschow, D. H., and Sullivan, P. P.: An Objective Method for Deriving Atmospheric Structure from Airborne Lidar Observations, Journal of Atmospheric and Oceanic Technology, 17, 1455-1468, https://doi.org/10.1175/1520-0426(2000)017<1455:AOMFDA>2.0.CO;2, 2000.

DeCarlo, P. F., Dunlea, E. J., Kimmel, J. R., Aiken, A. C., Sueper, D., Crounse, J., Wennberg, P. O., Emmons, L., Shinozuka, Y., Clarke, A., Zhou, J., Tomlinson, J., Collins, D. R., Knapp, D., Weinheimer, A. J., Montzka, D. D., Campos, T., and Jimenez, J. L.: Fast airborne aerosol size and chemistry measurements above Mexico City and Central Mexico during the MILAGRO campaign, Atmos. Chem. Phys., 8, 4027-4048, 10.5194/acp-8-4027-2008, 2008.

DiGangi, J. P., Choi, Y., Nowak, J. B., Halliday, H. S., Diskin, G. S., Feng, S., Barkley, Z. R., Lauvaux, T., Pal, S., Davis, K. J., Baier, B. C., and Sweeney, C.: Seasonal Variability in Local Carbon Dioxide Biomass Burning Sources Over Central and Eastern US Using Airborne In Situ Enhancement Ratios, Journal of Geophysical Research: Atmospheres, 126, e2020JD034525, https://doi.org/10.1029/2020JD034525, 2021.

Diskin, G., Podolske, J., Sachse, G., and Slate, T.: Open-path airborne tunable diode laser hygrometer, International Symposium on Optical Science and Technology, https://doi.org/10.1117/12.453736, 2002.

Doelling, D., Haney, C., Bhatt, R., Scarino, B., and Gopalan, A.: Geostationary Visible Imager Calibration for the CERES SYN1deg Edition 4 Product, Remote Sensing, 10, 288, 2018.

Durkee, P. A., Noone, K. J., and Bluth, R. T.: The Monterey Area Ship Track Experiment, Journal of the Atmospheric Sciences, 57, 2523-2541, https://doi.org/10.1175/1520-0469(2000)057<2523:TMASTE>2.0.CO;2, 2000.

Eckhardt, S. S., A.; Sodemann, H.; Frank, A.; Seibert, P.,; Wotawa, G.: The Lagrangian particle dispersion model FLEXPART version 8.0, Norwegian Institute of Air Research, 2008.

Emanuel, K. A. and Živković-Rothman, M.: Development and Evaluation of a Convection Scheme for Use in Climate Models, Journal of the Atmospheric Sciences, 56, 1766-1782, 10.1175/1520-0469(1999)056<1766:Daeoac>2.0.Co;2, 1999.

Fast, J. D., Gustafson Jr, W. I., Berg, L. K., Shaw, W. J., Pekour, M., Shrivastava, M., Barnard, J. C., Ferrare, R. A., Hostetler, C. A., Hair, J. A., Erickson, M., Jobson, B. T., Flowers, B., Dubey, M. K., Springston, S., Pierce, R. B., Dolislager, L., Pederson, J., and Zaveri, R. A.: Transport and mixing patterns over Central California during the carbonaceous aerosol and radiative effects study (CARES), Atmos. Chem. Phys., 12, 1759-1783, 10.5194/acp-12-1759-2012, 2012.

Fletcher, J., Mason, S., and Jakob, C.: The Climatology, Meteorology, and Boundary Layer Structure of Marine Cold Air Outbreaks in Both Hemispheres, J Clim, 29, 1999-2014, 10.1175/jcli-d-15-0268.1, 2016.

Froyd, K. D., Murphy, D. M., Brock, C. A., Campuzano-Jost, P., Dibb, J. E., Jimenez, J. L., Kupc, A., Middlebrook, A. M., Schill, G. P., Thornhill, K. L., Williamson, C. J., Wilson, J. C., and Ziemba, L. D.: A new method to quantify mineral dust and other aerosol species from aircraft platforms using single-particle mass spectrometry, Atmos. Meas. Tech., 12, 6209-6239, 10.5194/amt-12-6209-2019, 2019.

Fu, D., Di Girolamo, L., Rauber, R. M., McFarquhar, G. M., Nesbitt, S. W., Loveridge, J., Hong, Y., van Diedenhoven, B., Cairns, B., Alexandrov, M. D., Lawson, P., Woods, S., Tanelli, S., Schmidt, S., Hostetler, C., and Scarino, A. J.: An evaluation of the liquid cloud droplet effective radius derived from MODIS, airborne remote sensing, and in situ measurements from CAMP2Ex, Atmos. Chem. Phys., 22, 8259-8285, 10.5194/acp-22-8259-2022, 2022.

Gelaro, R., McCarty, W., Suárez, M. J., Todling, R., Molod, A., Takacs, L., Randles, C. A., Darmenov, A., Bosilovich, M. G., Reichle, R., Wargan, K., Coy, L., Cullather, R., Draper, C., Akella, S., Buchard, V., Conaty, A., da Silva, A. M., Gu, W., Kim, G.-K., Koster, R., Lucchesi, R., Merkova, D., Nielsen, J. E., Partyka, G., Pawson, S., Putman, W., Rienecker, M., Schubert, S. D., Sienkiewicz, M., and Zhao, B.: The Modern-Era Retrospective Analysis for Research and Applications, Version 2 (MERRA-2), J Clim, 30, 5419-5454, 10.1175/jcli-d-16-0758.1, 2017.

Gonzalez, M. E., Corral, A. F., Crosbie, E., Dadashazar, H., Diskin, G. S., Edwards, E.-L., Kirschler, S., Moore, R. H., Robinson, C. E., Schlosser, J. S., Shook, M., Stahl, C., Thornhill, K. L., Voigt, C., Winstead, E., Ziemba, L. D., and Sorooshian, A.: Relationships between supermicrometer particle concentrations and cloud water sea salt and dust concentrations: analysis of MONARC and ACTIVATE data, Environmental Science: Atmospheres, 10.1039/D2EA00049K, 2022.

Gurganus, C. and Lawson, P.: Laboratory and Flight Tests of 2D Imaging Probes: Toward a Better Understanding of Instrument Performance and the Impact on Archived Data, Journal of Atmospheric and Oceanic Technology, 35, 1533-1553, 10.1175/jtech-d-17-0202.1, 2018.

Hair, J. W., Hostetler, C. A., Cook, A. L., Harper, D. B., Ferrare, R. A., Mack, T. L., Welch, W., Izquierdo, L. R., and Hovis, F. E.: Airborne High Spectral Resolution Lidar for profiling aerosol optical properties, Appl. Opt., 47, 6734-6752, 10.1364/AO.47.006734, 2008.

Hilario, M. R. A., Crosbie, E., Bañaga, P. A., Betito, G., Braun, R. A., Cambaliza, M. O., Corral, A. F., Cruz, M. T., Dibb, J. E., Lorenzo, G. R., MacDonald, A. B., Robinson, C. E., Shook, M. A., Simpas, J. B., Stahl, C., Winstead, E., Ziemba, L. D., and Sorooshian, A.: Particulate Oxalate-To-Sulfate Ratio as an Aqueous Processing Marker: Similarity Across Field Campaigns and Limitations, Geophysical Research Letters, 48, e2021GL096520, https://doi.org/10.1029/2021GL096520, 2021.

Hu, Y., Stamnes, K., Vaughan, M., Pelon, J., Weimer, C., Wu, D., Cisewski, M., Sun, W., Yang, P., Lin, B., Omar, A., Flittner, D., Hostetler, C., Trepte, C., Winker, D., Gibson, G., and Santa-Maria, M.: Sea surface wind speed estimation from space-based lidar measurements, Atmos. Chem. Phys., 8, 3593-3601, 10.5194/acp-8-3593-2008, 2008.

Kirschler, S., Voigt, C., Anderson, B., Campos Braga, R., Chen, G., Corral, A. F., Crosbie, E., Dadashazar, H., Ferrare, R. A., Hahn, V., Hendricks, J., Kaufmann, S., Moore, R., Pöhlker, M. L., Robinson, C., Scarino, A. J., Schollmayer, D., Shook, M. A., Thornhill, K. L., Winstead, E., Ziemba, L. D., and Sorooshian, A.: Seasonal updraft speeds change cloud droplet number concentrations in low-level clouds over the western North Atlantic, Atmos. Chem. Phys., 22, 8299-8319, 10.5194/acp-22-8299-2022, 2022.

Kleine, J., Voigt, C., Sauer, D., Schlager, H., Scheibe, M., Jurkat-Witschas, T., Kaufmann, S., Kärcher, B., and Anderson, B. E.: In Situ Observations of Ice Particle Losses in a Young Persistent Contrail, Geophysical Research Letters, 45, 13,553-513,561, https://doi.org/10.1029/2018GL079390, 2018.

Knollenberg, R. G.: The Optical Array : An Alternative to Scattering or Extinction for Airborne Particle Size Determination, Journal of Applied Meteorology (1962-1982), 9, 86-103, 1970.

Knop, I., Bansmer, S. E., Hahn, V., and Voigt, C.: Comparison of different droplet measurement techniques in the Braunschweig Icing Wind Tunnel, Atmos. Meas. Tech., 14, 1761-1781, 10.5194/amt-14-1761-2021, 2021.

Lance, S.: Coincidence Errors in a Cloud Droplet Probe (CDP) and a Cloud and Aerosol Spectrometer (CAS), and the Improved Performance of a Modified CDP, Journal of Atmospheric and Oceanic Technology, 29, 1532-1541, 10.1175/jtech-d-11-00208.1, 2012.

Lawson, R. P. and Baker, B. A.: Improvement in Determination of Ice Water Content from Two-Dimensional Particle Imagery. Part II: Applications to Collected Data, Journal of Applied Meteorology and Climatology, 45, 1291-1303, 10.1175/jam2399.1, 2006.

Lawson, R. P., Woods, S., Jensen, E., Erfani, E., Gurganus, C., Gallagher, M., Connolly, P., Whiteway, J., Baran, A. J., May, P., Heymsfield, A., Schmitt, C. G., McFarquhar, G., Um, J., Protat, A., Bailey, M., Lance, S., Muehlbauer, A., Stith, J., Korolev, A., Toon, O. B., and Krämer, M.: A Review of Ice Particle Shapes in Cirrus formed In Situ and in Anvils, Journal of Geophysical Research: Atmospheres, 124, 10049-10090, https://doi.org/10.1029/2018JD030122, 2019.

Leaitch, W. R., Banic, C. M., Isaac, G. A., Couture, M. D., Liu, P. S. K., Gultepe, I., Li, S.-M., Kleinman, L., Daum, P. H., and MacPherson, J. I.: Physical and chemical observations in marine stratus during the 1993 North Atlantic Regional Experiment: Factors controlling cloud droplet number concentrations, Journal of Geophysical Research: Atmospheres, 101, 29123-29135, https://doi.org/10.1029/96JD01228, 1996.

Leaitch, W. R., Lohmann, U., Russell, L. M., Garrett, T., Shantz, N. C., Toom-Sauntry, D., Strapp, J. W., Hayden, K. L., Marshall, J., Wolde, M., Worsnop, D. R., and Jayne, J. T.: Cloud albedo increase from carbonaceous aerosol, Atmos. Chem. Phys., 10, 7669-7684, 10.5194/acp-10-7669-2010, 2010.

Lenschow, D. H.: Probing the Atmospheric Boundary Layer, American Meteorological Society, Boston, 1986.

Levy, R. C., Mattoo, S., Munchak, L. A., Remer, L. A., Sayer, A. M., Patadia, F., and Hsu, N. C.: The Collection 6 MODIS aerosol products over land and ocean, Atmos. Meas. Tech., 6, 2989-3034, 10.5194/amt-6-2989-2013, 2013.

Li, X.-Y., Wang, H., Chen, J., Endo, S., George, G., Cairns, B., Chellappan, S., Zeng, X., Kirschler, S., Voigt, C., Sorooshian, A., Crosbie, E., Chen, G., Ferrare, R. A., Gustafson, W. I., Hair, J. W., Kleb, M. M., Liu, H., Moore, R., Painemal, D., Robinson, C., Scarino, A. J., Shook, M., Shingler, T. J., Thornhill, K. L., Tornow, F., Xiao, H., Ziemba, L. D., and Zuidema, P.: Large-Eddy Simulations of Marine Boundary Layer Clouds Associated with Cold-Air Outbreaks during the ACTIVATE Campaign. Part I: Case Setup and Sensitivities to Large-Scale Forcings, Journal of the Atmospheric Sciences, 79, 73-100, 10.1175/jas-d-21-0123.1, 2022.

Mason, B., Wagner, N. L., Adler, G., Andrews, E., Brock, C. A., Gordon, T. D., Lack, D. A., Perring, A. E., Richardson, M. S., Schwarz, J. P., Shook, M. A., Thornhill, K. L., Ziemba, L. D., and Murphy, D. M.: An intercomparison of aerosol absorption measurements conducted during the SEAC4RS campaign, Aerosol Science and Technology, 52, 1012-1027, 10.1080/02786826.2018.1500012, 2018.

McNaughton, C. S., Clarke, A. D., Howell, S. G., Pinkerton, M., Anderson, B., Thornhill, L., Hudgins, C., Winstead, E., Dibb, J. E., Scheuer, E., and Maring, H.: Results from the DC-8 Inlet Characterization Experiment (DICE): Airborne Versus Surface Sampling of Mineral Dust and Sea Salt Aerosols, Aerosol Science and Technology, 41, 136-159, 10.1080/02786820601118406, 2007.

Mechoso, C. R., Wood, R., Weller, R., Bretherton, C. S., Clarke, A. D., Coe, H., Fairall, C., Farrar, J. T., Feingold, G., Garreaud, R., Grados, C., McWilliams, J., de Szoeke, S. P., Yuter, S. E., and Zuidema, P.: Ocean–Cloud–Atmosphere–Land Interactions in the Southeastern Pacific: The VOCALS Program, Bulletin of the American Meteorological Society, 95, 357-375, https://doi.org/10.1175/BAMS-D-11-00246.1, 2014.

Minnis, P., Nguyen, L., Palikonda, R., Heck, P., Spangenberg, D., Doelling, D., Ayers, J. K., Smith, W., Khaiyer, M., Trepte, Q., Avey, L., Chang, F.-L., Yost, C., Chee, T., and Szedung, S.-M.: Near-real time cloud retrievals from operational and research meteorological satellites, SPIE Remote Sensing, SPIE2008.

Minnis, P., Sun-Mack, S., Chen, Y., Chang, F. L., Yost, C. R., Smith, W. L., Heck, P. W., Arduini, R. F., Bedka, S. T., Yi, Y., Hong, G., Jin, Z., Painemal, D., Palikonda, R., Scarino, B. R., Spangenberg, D. A., Smith, R. A., Trepte, Q. Z., Yang, P., and Xie, Y.: CERES MODIS Cloud Product Retrievals for Edition 4—Part I: Algorithm Changes, IEEE Transactions on Geoscience and Remote Sensing, 59, 2744-2780, 10.1109/TGRS.2020.3008866, 2021.

Moore, R. H. and Nenes, A.: Scanning Flow CCN Analysis—A Method for Fast Measurements of CCN Spectra, Aerosol Science and Technology, 43, 1192-1207, 10.1080/02786820903289780, 2009.

Nakajima, T. and King, M. D.: Determination of the Optical Thickness and Effective Particle Radius of Clouds from Reflected Solar Radiation Measurements. Part I: Theory, Journal of Atmospheric Sciences, 47, 1878-1893, 10.1175/1520-0469(1990)047<1878:Dotota>2.0.Co;2, 1990.

Nied, J., Jones, M., Seaman, S., Shingler, T., Hair, J., Cairns, B., Gilst, D. V., Bucholtz, A., Schmidt, S., Chellappan, S., Zuidema, P., Van Diedenhoven, B., Sorooshian, A., and Stamnes, S.: A cloud detection neural network for above-aircraft clouds using airborne cameras, Frontiers in Remote Sensing, 4, 10.3389/frsen.2023.1118745, 2023.

Northup, E., Chen, G., Aikin, K., and Webster, C.: ICARTT File Format Standards V2.0, https://www.earthdata.nasa.gov/esdis/esco/standards-and-references/icartt-file-format, 2017.

Painemal, D.: Global Estimates of Changes in Shortwave Low-Cloud Albedo and Fluxes Due to Variations in Cloud Droplet Number Concentration Derived From CERES-MODIS Satellite Sensors, Geophysical Research Letters, 45, 9288-9296, https://doi.org/10.1029/2018GL078880, 2018.

Painemal, D., Corral, A. F., Sorooshian, A., Brunke, M. A., Chellappan, S., Afzali Gorooh, V., Ham, S.-H., O'Neill, L., Smith Jr., W. L., Tselioudis, G., Wang, H., Zeng, X., and Zuidema, P.: An Overview of Atmospheric Features Over the Western North Atlantic Ocean and North American East Coast—Part 2: Circulation, Boundary Layer, and Clouds, Journal of Geophysical Research: Atmospheres, 126, e2020JD033423, https://doi.org/10.1029/2020JD033423, 2021.

Painemal, D., S. Chellappan, W. Smith Jr., D. Spangenberg, J. Park, A. Ackerman, J. Chen, E. Crosbie, R. Ferrare, J. Hair, S. Kirschler, X-Y Li, A. McComiskey, R. Moore, K. Sanchez, A. Sorooshian, F. Tornow, C. Voigt, H. Wang, X. Zeng, L. Ziemba, P. Zuidema, and Winstead, E.: Wintertime synoptic patterns of midlatitude boundary layer clouds over the western North Atlantic: Climatology and insights from in-situ ACTIVATE observations,, J. Geophys. Res., 2023.

Papritz, L., Pfahl, S., Sodemann, H., and Wernli, H.: A Climatology of Cold Air Outbreaks and Their Impact on Air–Sea Heat Fluxes in the High-Latitude South Pacific, J Clim, 28, 342-364, 10.1175/jcli-d-14-00482.1, 2015.

Pisso, I., Sollum, E., Grythe, H., Kristiansen, N. I., Cassiani, M., Eckhardt, S., Arnold, D., Morton, D., Thompson, R. L., Groot Zwaaftink, C. D., Evangeliou, N., Sodemann, H., Haimberger, L., Henne, S., Brunner, D., Burkhart, J. F., Fouilloux, A., Brioude, J., Philipp, A., Seibert, P., and Stohl, A.: The Lagrangian particle dispersion model FLEXPART version 10.4, Geosci. Model Dev., 12, 4955-4997, 10.5194/gmd-12-4955-2019, 2019.

Randles, C. A., da Silva, A. M., Buchard, V., Colarco, P. R., Darmenov, A., Govindaraju, R., Smirnov, A., Holben, B., Ferrare, R., Hair, J., Shinozuka, Y., and Flynn, C. J.: The MERRA-2 Aerosol Reanalysis, 1980 Onward. Part I: System Description and Data Assimilation Evaluation, J Clim, 30, 6823-6850, 10.1175/jcli-d-16-0609.1, 2017.

Redemann, J., Wood, R., Zuidema, P., Doherty, S. J., Luna, B., LeBlanc, S. E., Diamond, M. S., Shinozuka, Y., Chang, I. Y., Ueyama, R., Pfister, L., Ryoo, J. M., Dobracki, A. N., da Silva, A. M., Longo, K. M., Kacenelenbogen, M. S., Flynn, C. J., Pistone, K., Knox, N. M., Piketh, S. J., Haywood, J. M., Formenti, P., Mallet, M., Stier, P., Ackerman, A. S., Bauer, S. E., Fridlind, A. M., Carmichael, G. R., Saide, P. E., Ferrada, G. A., Howell, S. G., Freitag, S., Cairns, B., Holben, B. N., Knobelspiesse, K. D., Tanelli, S., L'Ecuyer, T. S., Dzambo, A. M., Sy, O. O., McFarquhar, G. M., Poellot, M. R., Gupta, S., O'Brien, J. R., Nenes, A., Kacarab, M., Wong, J. P. S., Small-Griswold, J. D., Thornhill, K. L., Noone, D., Podolske, J. R., Schmidt, K. S., Pilewskie, P., Chen, H., Cochrane, S. P., Sedlacek, A. J., Lang, T. J., Stith, E., Segal-Rozenhaimer, M., Ferrare, R. A., Burton, S. P., Hostetler, C. A., Diner, D. J., Seidel, F. C., Platnick, S. E., Myers, J. S., Meyer, K. G., Spangenberg, D. A., Maring, H., and Gao, L.: An overview of the ORACLES (ObseRvations of Aerosols above CLouds and their intEractionS) project: aerosol–cloud–radiation interactions in the southeast Atlantic basin, Atmos. Chem. Phys., 21, 1507-1563, 10.5194/acp-21-1507-2021, 2021.

Reid, J. S., Maring, H. B., Narisma, G. T., van den Heever, S., Di Girolamo, L., Ferrare, R., Holz, R. E., Lawson, P., Mace, G. C., Simpas, J. B., Tanelli, S., Ziemba, L., van Diedenhoven, B., and al., e.: The coupling between tropical meteorology, aerosol lifecycle, convection, and radiation, during the Clouds, Aerosol and Monsoon Processes Philippines Experiment (CAMP2Ex), Bull Amer. Met. Soc., in press, 2023.

Rienecker, M. M. M. J. S. R. T. J. B. L. T. H.-C. L. W. G. M. S. R. D. K.: The GEOS-5 Data Assimilation System - Documentation of Versions 5.0.1, 5.1.0, and 5.2.0., National Aeronautics and Space Administration, Goddard Space Flight Center, Greenbelt, Maryland, 2008.

Scarino, A. J., Obland, M. D., Fast, J. D., Burton, S. P., Ferrare, R. A., Hostetler, C. A., Berg, L. K., Lefer, B., Haman, C., Hair, J. W., Rogers, R. R., Butler, C., Cook, A. L., and Harper, D. B.: Comparison of mixed layer heights from airborne high spectral resolution lidar, ground-based measurements, and the WRF-Chem model during CalNex and CARES, Atmos. Chem. Phys., 14, 5547-5560, 10.5194/acp-14-5547-2014, 2014.

Schlosser, J. S., Stamnes, S., Burton, S. P., Cairns, B., Crosbie, E., Van Diedenhoven, B., Diskin, G., Dmitrovic, S., Ferrare, R., Hair, J. W., Hostetler, C. A., Hu, Y., Liu, X., Moore, R. H., Shingler, T., Shook, M. A., Thornhill, K. L., Winstead, E., Ziemba, L., and Sorooshian, A.: Polarimeter + Lidar–Derived Aerosol Particle Number Concentration, Frontiers in Remote Sensing, 3, 10.3389/frsen.2022.885332, 2022.

Schulien, J. A., Behrenfeld, M. J., Hair, J. W., Hostetler, C. A., and Twardowski, M. S.: Vertically- resolved phytoplankton carbon and net primary production from a high spectral resolution lidar, Opt. Express, 25, 13577-13587, 10.1364/OE.25.013577, 2017.

Seethala, C., Zuidema, P., Edson, J., Brunke, M., Chen, G., Li, X.-Y., Painemal, D., Robinson, C., Shingler, T., Shook, M., Sorooshian, A., Thornhill, L., Tornow, F., Wang, H., Zeng, X., and Ziemba, L.: On Assessing ERA5 and MERRA2 Representations of Cold-Air Outbreaks Across the Gulf Stream, Geophysical Research Letters, 48, e2021GL094364, https://doi.org/10.1029/2021GL094364, 2021.

Shingler, T., Dey, S., Sorooshian, A., Brechtel, F. J., Wang, Z., Metcalf, A., Coggon, M., Mülmenstädt, J., Russell, L. M., Jonsson, H. H., and Seinfeld, J. H.: Characterisation and airborne deployment of a new counterflow virtual impactor inlet, Atmos. Meas. Tech., 5, 1259-1269, 10.5194/amt-5-1259-2012, 2012.

Shingler, T., Crosbie, E., Ortega, A., Shiraiwa, M., Zuend, A., Beyersdorf, A., Ziemba, L., Anderson, B., Thornhill, L., Perring, A. E., Schwarz, J. P., Campazano-Jost, P., Day, D. A., Jimenez, J. L., Hair, J. W., Mikoviny, T., Wisthaler, A., and Sorooshian, A.: Airborne characterization of subsaturated aerosol hygroscopicity and dry refractive index from the surface to 6.5 km during the SEAC4RS campaign, Journal of Geophysical Research: Atmospheres, 121, 4188-4210, https://doi.org/10.1002/2015JD024498, 2016.

Sinclair, K., van Diedenhoven, B., Cairns, B., Yorks, J., Wasilewski, A., and McGill, M.: Remote sensing of multiple cloud layer heights using multi-angular measurements, Atmos. Meas. Tech., 10, 2361-2375, 10.5194/amt-10-2361-2017, 2017.

Sinclair, K., van Diedenhoven, B., Cairns, B., Alexandrov, M., Moore, R., Crosbie, E., and Ziemba, L.: Polarimetric retrievals of cloud droplet number concentrations, Remote Sensing of Environment, 228, 227-240, https://doi.org/10.1016/j.rse.2019.04.008, 2019.

Sorooshian, A., Brechtel, F. J., Ma, Y., Weber, R. J., Corless, A., Flagan, R. C., and Seinfeld, J. H.: Modeling and Characterization of a Particle-into-Liquid Sampler (PILS), Aerosol Science and Technology, 40, 396-409, 10.1080/02786820600632282, 2006.

Sorooshian, A., MacDonald, A. B., Dadashazar, H., Bates, K. H., Coggon, M. M., Craven, J. S., Crosbie, E., Hersey, S. P., Hodas, N., Lin, J. J., Negrón Marty, A., Maudlin, L. C., Metcalf, A. R., Murphy, S. M., Padró, L. T., Prabhakar, G., Rissman, T. A., Shingler, T., Varutbangkul, V., Wang, Z., Woods, R. K., Chuang, P. Y., Nenes, A., Jonsson, H. H., Flagan, R. C., and Seinfeld, J. H.: A multi-year data set on aerosol-cloud-precipitation-meteorology interactions for marine stratocumulus clouds, Scientific Data, 5, 180026, 10.1038/sdata.2018.26, 2018.

Sorooshian, A., Corral, A. F., Braun, R. A., Cairns, B., Crosbie, E., Ferrare, R., Hair, J., Kleb, M. M., Hossein Mardi, A., Maring, H., McComiskey, A., Moore, R., Painemal, D., Scarino, A. J., Schlosser, J., Shingler, T., Shook, M., Wang, H., Zeng, X., Ziemba, L., and Zuidema, P.: Atmospheric Research Over the Western North Atlantic Ocean Region and North American East Coast: A Review of Past Work and Challenges Ahead, Journal of Geophysical Research: Atmospheres, 125, e2019JD031626, https://doi.org/10.1029/2019JD031626, 2020.

Sorooshian, A., Anderson, B., Bauer, S. E., Braun, R. A., Cairns, B., Crosbie, E., Dadashazar, H., Diskin, G., Ferrare, R., Flagan, R. C., Hair, J., Hostetler, C., Jonsson, H. H., Kleb, M. M., Liu, H., MacDonald, A. B., McComiskey, A., Moore, R., Painemal, D., Russell, L. M., Seinfeld, J. H., Shook, M., Smith, W. L., Thornhill, K., Tselioudis, G., Wang, H., Zeng, X., Zhang, B., Ziemba, L., and Zuidema, P.: Aerosol–Cloud–Meteorology Interaction Airborne Field Investigations: Using Lessons Learned from the U.S. West Coast in the Design of ACTIVATE off the U.S. East Coast, Bulletin of the American Meteorological Society, 100, 1511-1528, 10.1175/bams-d-18-0100.1, 2019.

Stahl, C., Crosbie, E., Bañaga, P. A., Betito, G., Braun, R. A., Cainglet, Z. M., Cambaliza, M. O., Cruz, M. T., Dado, J. M., Hilario, M. R. A., Leung, G. F., MacDonald, A. B., Magnaye, A. M., Reid, J., Robinson, C., Shook, M. A., Simpas, J. B., Visaga, S. M., Winstead, E., Ziemba, L., and Sorooshian, A.: Total organic carbon and the contribution from speciated organics in cloud water: airborne data analysis from the CAMP2Ex field campaign, Atmos. Chem. Phys., 21, 14109-14129, 10.5194/acp-21-14109-2021, 2021.

Stamnes, S., Hostetler, C., Ferrare, R., Burton, S., Liu, X., Hair, J., Hu, Y., Wasilewski, A., Martin, W., van Diedenhoven, B., Chowdhary, J., Cetinić, I., Berg, L. K., Stamnes, K., and Cairns, B.: Simultaneous polarimeter retrievals of microphysical aerosol and ocean color parameters from the "MAPP" algorithm with comparison to high-spectral-resolution lidar aerosol and ocean products, Appl. Opt., 57, 2394-2413, 10.1364/AO.57.002394, 2018.

Stohl, A., Hittenberger, M., and Wotawa, G.: Validation of the lagrangian particle dispersion model FLEXPART against large-scale tracer experiment data, Atmospheric Environment, 32, 4245-4264, https://doi.org/10.1016/S1352-2310(98)00184-8, 1998.

The Lagrangian particle dispersion model FLEXPART version 8.2: https://www.flexpart.eu/downloads/26, last access: 8 Febrauary 2023.

Sugimoto, N. and Lee, C. H.: Characteristics of dust aerosols inferred from lidar depolarization measurements at two wavelengths, Appl. Opt., 45, 7468-7474, 10.1364/AO.45.007468, 2006.

Thornhill, K. L., Anderson, B. E., Barrick, J. D. W., Bagwell, D. R., Friesen, R., and Lenschow, D. H.: Air motion intercomparison flights during Transport and Chemical Evolution in the Pacific (TRACE-P)/ACE-ASIA, Journal of Geophysical Research: Atmospheres, 108, https://doi.org/10.1029/2002JD003108, 2003.

Toon, O. B., Maring, H., Dibb, J., Ferrare, R., Jacob, D. J., Jensen, E. J., Luo, Z. J., Mace, G. G., Pan, L. L., Pfister, L., Rosenlof, K. H., Redemann, J., Reid, J. S., Singh, H. B., Thompson, A. M., Yokelson, R., Minnis, P., Chen, G., Jucks, K. W., and Pszenny, A.: Planning, implementation, and scientific goals of the Studies of Emissions and Atmospheric Composition, Clouds and Climate Coupling by Regional Surveys (SEAC4RS) field mission, Journal of Geophysical Research: Atmospheres, 121, 4967-5009, https://doi.org/10.1002/2015JD024297, 2016.

Tornow, F., Ackerman, A. S., Fridlind, A. M., Cairns, B., Crosbie, E. C., Kirschler, S., Moore, R. H., Painemal, D., Robinson, C. E., Seethala, C., Shook, M. A., Voigt, C., Winstead, E. L., Ziemba, L. D., Zuidema, P., and Sorooshian, A.: Dilution of Boundary Layer Cloud Condensation Nucleus Concentrations by Free Tropospheric Entrainment During Marine Cold Air Outbreaks, Geophysical Research Letters, 49, e2022GL098444, https://doi.org/10.1029/2022GL098444, 2022.

van Diedenhoven, B., Fridlind, A. M., Ackerman, A. S., and Cairns, B.: Evaluation of Hydrometeor Phase and Ice Properties in Cloud-Resolving Model Simulations of Tropical Deep Convection Using Radiance and Polarization Measurements, Journal of the Atmospheric Sciences, 69, 3290-3314, 10.1175/jas-d-11-0314.1, 2012.

Virkkula, A.: Correction of the Calibration of the 3-wavelength Particle Soot Absorption Photometer (3λ PSAP), Aerosol Science and Technology, 44, 706-712, 10.1080/02786826.2010.482110, 2010.

Vogelezang, D. H. P. and Holtslag, A. A. M.: Evaluation and model impacts of alternative boundary-layer height formulations, Boundary-Layer Meteorology, 81, 245-269, 10.1007/BF02430331, 1996.

Voigt, C., Kleine, J., Sauer, D., Moore, R. H., Bräuer, T., Le Clercq, P., Kaufmann, S., Scheibe, M., Jurkat-Witschas, T., Aigner, M., Bauder, U., Boose, Y., Borrmann, S., Crosbie, E., Diskin, G. S., DiGangi, J., Hahn, V., Heckl, C., Huber, F., Nowak, J. B., Rapp, M., Rauch, B., Robinson, C., Schripp, T., Shook, M., Winstead, E., Ziemba, L., Schlager, H., and Anderson, B. E.: Cleaner burning aviation fuels can reduce contrail cloudiness, Communications Earth & Environment, 2, 114, 10.1038/s43247-021-00174-y, 2021.

Vömel, H., Sorooshian, A., Robinson, C., Shingler, T. J., Thornhill, K. L., and Ziemba, L. D.: Dropsonde observations during the Aerosol Cloud meTeorology Interactions oVer the western ATlantic Experiment, Scientific Data, in review.

Vömel, H., Goodstein, M., Tudor, L., Witte, J., Fuchs-Stone, Ž., Sentić, S., Raymond, D., Martinez-Claros, J., Juračić, A., Maithel, V., and Whitaker, J. W.: High-resolution in situ observations of atmospheric thermodynamics using dropsondes during the Organization of Tropical East Pacific Convection (OTREC) field campaign, Earth Syst. Sci. Data, 13, 1107-1117, 10.5194/essd-13-1107-2021, 2021.

Wang, J., Wood, R., Jensen, M. P., Chiu, J. C., Liu, Y., Lamer, K., Desai, N., Giangrande, S. E., Knopf, D. A., Kollias, P., Laskin, A., Liu, X., Lu, C., Mechem, D., Mei, F., Starzec, M., Tomlinson, J., Wang, Y., Yum, S. S., Zheng, G., Aiken, A. C., Azevedo, E. B., Blanchard, Y., China, S., Dong, X., Gallo, F., Gao, S., Ghate, V. P., Glienke, S., Goldberger, L., Hardin, J. C., Kuang, C., Luke, E. P., Matthews, A. A., Miller, M. A., Moffet, R., Pekour, M., Schmid, B., Sedlacek, A. J., Shaw, R. A., Shilling, J. E., Sullivan, A., Suski, K., Veghte, D. P., Weber, R., Wyant, M., Yeom, J., Zawadowicz, M., and Zhang, Z.: Aerosol and Cloud Experiments in the Eastern North Atlantic (ACE-ENA), Bulletin of the American Meteorological Society, 103, E619-E641, 10.1175/bams-d-19-0220.1, 2022.

Wei, Y., Shrestha, R., Pal, S., Gerken, T., Feng, S., McNelis, J., Singh, D., Thornton, M. M., Boyer, A. G., Shook, M. A., Chen, G., Baier, B. C., Barkley, Z. R., Barrick, J. D., Bennett, J. R., Browell, E. V., Campbell, J. F., Campbell, L. J., Choi, Y., Collins, J., Dobler, J., Eckl, M., Fiehn, A., Fried, A., Digangi, J. P., Barton-Grimley, R., Halliday, H., Klausner, T., Kooi, S., Kostinek, J., Lauvaux, T., Lin, B., McGill, M. J., Meadows, B., Miles, N. L., Nehrir, A. R., Nowak, J. B., Obland, M., O'Dell, C., Fao, R. M. P., Richardson, S. J., Richter, D., Roiger, A., Sweeney, C., Walega, J., Weibring, P., Williams, C. A., Yang, M. M., Zhou, Y., and Davis, K. J.: Atmospheric Carbon and Transport – America (ACT-America) Data Sets: Description, Management, and Delivery, Earth and Space Science, 8, e2020EA001634, https://doi.org/10.1029/2020EA001634, 2021.

Wu, L., Hasekamp, O., van Diedenhoven, B., Cairns, B., Yorks, J. E., and Chowdhary, J.: Passive remote sensing of aerosol layer height using near-UV multiangle polarization measurements, Geophysical Research Letters, 43, 8783-8790, https://doi.org/10.1002/2016GL069848, 2016.

Zhang, B., Owen, R. C., Perlinger, J. A., Kumar, A., Wu, S., Val Martin, M., Kramer, L., Helmig, D., and Honrath, R. E.: A semi-Lagrangian view of ozone production tendency in North American outflow in the summers of 2009 and 2010, Atmos. Chem. Phys., 14, 2267-2287, 10.5194/acp-14-2267-2014, 2014.

Ziemba, L. D., Lee Thornhill, K., Ferrare, R., Barrick, J., Beyersdorf, A. J., Chen, G., Crumeyrolle, S. N., Hair, J., Hostetler, C., Hudgins, C., Obland, M., Rogers, R., Scarino, A. J., Winstead, E. L., and Anderson, B. E.: Airborne observations of aerosol extinction by in situ and remote-sensing techniques: Evaluation of particle hygroscopicity, Geophysical Research Letters, 40, 417-422, https://doi.org/10.1029/2012GL054428, 2013.

Zuidema, P., Redemann, J., Haywood, J., Wood, R., Piketh, S., Hipondoka, M., and Formenti, P.: Smoke and Clouds above the Southeast Atlantic: Upcoming Field Campaigns Probe Absorbing Aerosol's Impact on Climate, Bulletin of the American Meteorological Society, 97, 1131-1135, https://doi.org/10.1175/BAMS-D-15-00082.1, 2016.

Table 1. Overall summary of ACTIVATE flight metrics categorized by each of the six deployments between 2020 and 2022. Joint ensembles represent when both planes were in coordination and conducting the series of legs (in some combination) shown in Fig. 2. The number of dropsondes shown represent those with full profiles of all variables with good parachute performance. The threshold science mission goal for cloud ensembles required only 100 of the 200 to be with joint aircraft and the remainder to be at least with just the Falcon. The threshold science mission represents a descoped version of the baseline mission to satisfy the minimum science acceptable for the investment, while the baseline mission satisfies performance requirements necessary to achieve the full science objectives of the mission.

	Research Flights			Flight Hours		Joint Ensembles		Underflights			
	Falcon	King Air	Joint	Falcon	King Air	Cloudy	Clear	ASTER	CALIPSO	Process Study Flights	Dropsondes
Winter 2020 (14 Feb – 12 Mar)	22	17	17	73	59	43	28	1	-	2	59
Summer 2020 (13 Aug – 30 Sep)	18	18	18	60	67	58	36	1	3	2	107
Winter 2021 (27 Jan – 2 Apr)	17	19	15	56	66	47	25	1	3	-	100
Summer 2021 (13 May – 30 Jun)	32	32	32	106	108	103	74	1	1	2	150
Winter 2021-2022 (30 Nov – 29 Mar)	55	54	53	182	193	198	72	-	1	2	214
Summer 2022 (3 May – 18 Jun)	30	28	27	97	98	86	46	2	3	4	155
Sum	***174***	***168***	***162***	***574***	***592***	***535***	***281***	***6***	***11***	***12***	***785***
Threshold Mission Goal						***200***	***12***				
Baseline Mission Goal						***250***	***15***				

Table 2. Summary of ACTIVATE research flights with pertinent details associated with date, times, and special notes. Research flights 48-61 included a reduced operational Falcon payload due to an aircraft maintenance limitation. Deployments are separated by blank rows: Deployment 1 (RF1-RF22), Deployment 2 (RF23-RF40), Deployment 3 (RF41-RF61), Deployment 4 (RF62-RF93), Deployment 5 (RF94-RF148), Deployment 6 (RF149-RF179).

				King Air			HU-25 Falcon		
RF	Date	Joint/ Single	Flight Type	Take Off (UTC)	Land (UTC)	# Sondes	Take Off (UTC)	Land (UTC)	Special Notes
1	2/14/2020	Joint	Statistical Survey	17:04:42	20:35:34	4	17:01:23	20:04:20	Landed at Newport News and stationed there until end of Winter 2020 deployment
2	2/15/2020	Joint	Statistical Survey	16:42:19	19:55:40	4	16:48:20	19:58:02	Some precipitation and air traffic challenges affecting Falcon ensemble leg order
3	2/17/2020	Joint	Statistical Survey	16:04:11	19:18:04	4	16:02:55	19:18:35	Relatively cloud-free with relatively high number of clear ensembles
4	2/21/2020	Single-Falcon	Statistical Survey	N/A	N/A	0	18:37:28	21:55:03	King Air maintenance issue; spiral sounding and 'wall' pattern
5	2/22/2020	Single-Falcon	Statistical Survey	N/A	N/A	0	13:54:11	17:02:40	King Air maintenance; characterize area downwind of where the next flight focused on
6	2/22/2020	Single-Falcon	Statistical Survey	N/A	N/A	0	18:59:14	22:26:40	King Air maintenance; wall pattern focusing on air mass sampled in RF5 in morning; spiral soundings
7	2/23/2020	Single-Falcon	Statistical Survey	N/A	N/A	0	13:30:55	16:54:06	King Air maintenance; Notes of MBL being more shallow closer to land with colder water
8	2/23/2020	Single-Falcon	Statistical Survey	N/A	N/A	0	18:25:54	21:55:32	King Air maintenance; transited high to far east point to buy range and save fuel; descended for cloud wall and then stat surveys back to base; precip below cloud
9	2/27/2020	Joint	Statistical Survey	18:05:40	21:30:10	2	17:56:35	21:27:05	Falcon conducted multiple "racetrack" delay loops to improve spatial coordination with King Air
10	2/28/2020	Joint	Process Study	14:05:07	18:18:53	11	14:20:42	17:41:44	Complex cloud scene with multiple cloud types in a single column where "wall" and associated spiral sounding occurred; 11 dropsondes
11	2/28/2020	Joint	Statistical Survey	19:20:00	23:25:46	2	19:36:01	22:49:25	Captured the evolution of the complex cloud field in the previous flight within the circle
12	2/29/2020	Joint	Statistical Survey	14:28:32	17:46:31	2	13:51:55	17:37:27	Forecasted to be clear but was actually a good cloudy day; Falcon "racetrack" delay loop to improve coordination
13	3/1/2020	Joint	Process Study	13:37:05	17:22:45	11	13:31:37	17:04:24	Cold air outbreak with same flight plan as RF10; 11 dropsondes

14	3/1/2020	Joint	Statistical Survey	18:36:49	22:05:44	2	18:32:24	21:47:50	Captured the evolution of the complex cloud field in the previous flight within the circle
15	3/2/2020	Joint	Statistical Survey	16:55:22	20:10:15	2	16:54:05	20:02:28	Biomass burning sampled towards end of flight; changing cloud base heights and precipitation observed with Falcon trying to optimize levels to maximize time in cloud
16	3/6/2020	Joint	Statistical Survey	18:19:06	21:45:24	3	18:09:58	21:28:19	High cloud fraction
17	3/8/2020	Joint	Statistical Survey	14:17:09	17:09:00	2	13:48:48	17:00:21	Good cloud flight
18	3/8/2020	Joint	Statistical Survey	18:25:20	21:56:15	2	18:32:39	21:57:45	Nearly identical track to RF17 from morning; forecasted clear but there were clouds
19	3/9/2020	Joint	Statistical Survey	16:15:08	19:58:44	2	16:33:40	19:51:15	Observations of smoke on return to base (visual and from HSRL-2)
20	3/11/2020	Joint	Statistical Survey	12:39:30	15:47:06	2	12:44:39	15:40:26	Real-time maneuvering with new waypoints and altitude changes required in flight due to convective weather
21	3/12/2020	Joint	Statistical Survey	13:45:47	17:20:17	2	14:07:19	17:15:37	ASTER underflight; northern end of the ASTER track had reduced cirrus compared to southern end
22	3/12/2020	Joint	Statistical Survey	19:00:18	22:30:17	2	18:57:32	22:16:50	Convective weather and icing concerns caused some King Air deviations in flight track; precipitation observed
23	8/13/2020	Joint	Statistical Survey	13:55:26	17:24:09	5	14:04:50	17:26:11	Convective weather with lightning; potential cold pool area; gradient in CO_2 and CH_4 on the southern end of track due to presumed different air mass
24	8/17/2020	Joint	Statistical Survey	14:31:44	18:17:05	6	14:28:24	17:55:34	Smoke observed at high altitude
25	8/20/2020	Joint	Statistical Survey	14:01:57	17:35:37	5	13:59:39	17:23:26	Forecasted to have minimal low cloud but had good low cloud (similar to RF12); high N_d values; did special maneuvers to improve aircraft coordination during flight; low cloud LWC prevented cloud water collection
26	8/21/2020	Joint	Statistical Survey	13:59:46	17:33:17	5	14:01:30	17:11:51	Low cloud LWC prevented cloud water collection; King Air maneuvered to avoid flying in cirrus
27	8/25/2020	Joint	Statistical Survey	13:57:23	17:57:51	6	14:03:00	17:25:15	Less cloud vertical development compared to previous Summer 2020 flights; note of distinct sulfate layer above cloud tops; HSRL-2 observed high altitude aerosol layers; lack of cloud water due to low LWC

28	8/26/2020	Joint	Statistical Survey	13:54:06	17:41:47	6	13:52:27	17:08:11	CALIPSO underflight; smoke layers; unicorn aerosol module (described in sect. 2.4) with polluted conditions during Falcon vertical spiral sounding
29	8/28/2020	Joint	Statistical Survey	16:33:23	20:25:59	8	16:44:03	20:02:19	Falcon transited at high altitude at start and end to accommodate CALIPSO overpass location as it was a CALIPSO underflight; mostly cloud-free; smoke; unicorn aerosol module
30	9/2/2020	Joint	Statistical Survey	15:14:31	19:07:24	6	15:23:58	18:45:19	High variability in MBL height and cloud fraction, along with vertically developing clouds making it challenging to do all cloud ensemble legs in order
31	9/3/2020	Joint	Statistical Survey	14:33:04	18:13:51	6	14:43:47	17:50:43	Precipitation noted during flight; a higher aerosol scattering day than normal potentially due to smoke
32	9/10/2020	Joint	Statistical Survey	16:56:25	20:01:34	4	17:05:12	20:02:56	Generally cleaner conditions than normal with low N_a and N_d
33	9/11/2020	Joint	Statistical Survey	14:10:24	17:43:19	6	14:28:40	17:40:09	ASTER underflight; ATC challenges led to Falcon being higher than desired at times
34	9/15/2020	Joint	Statistical Survey	15:53:39	19:42:08	6	16:04:50	19:17:38	Smoke observed; higher cloud fraction and vertically constrained clouds as compared to previous Summer 2020 flights
35	9/16/2020	Joint	Process Study	15:49:49	19:33:10	0	15:58:52	19:26:54	Easterly winds at times allowed for sampling of cloud processed air closer to shore west of clouds and the wall pattern; notes of possible smoke in air
36	9/21/2020	Joint	Statistical Survey	16:03:45	20:01:10	5	16:15:11	19:36:09	High sea salt due to high winds; high number of cloud water samples (10)
37	9/22/2020	Joint	Statistical Survey	17:35:20	21:47:53	7	17:51:57	21:27:29	Relatively high N_d (in contrast with lower values previous day); significant aerosol gradients
38	9/23/2020	Joint	Statistical Survey	16:39:21	20:16:08	8	16:33:18	20:11:57	CALIPSO underflight; smoke influence from western N. America; relatively cloud-free day with low cirrus
39	9/29/2020	Joint	Process Study	14:04:03	18:02:49	13	14:01:18	17:22:08	King Air did a "Wheel and Spoke" pattern; Falcon wall had many vertical levels flown; 13 dropsondes
40	9/30/2020	Joint	Statistical Survey	15:59:23	19:38:21	5	16:07:38	19:31:33	Good N_d gradients; turbulent Falcon flight; dry conditions noted aloft typical of post-frontal conditions
41	1/27/2021	Single-Falcon	Statistical Survey	N/A	N/A	0	17:59:24	20:38:19	Extra high altitude work for instrument quality control checks; Pilot staffing limitations

									allow for single aircraft flights this week (RF41-43)
42	1/29/2021	Single-King Air	Statistical Survey	12:57:24	15:52:52	2	N/A	N/A	Cold air outbreak
43	1/29/2021	Single-Falcon	Statistical Survey	N/A	N/A	0	17:40:12	20:39:41	Cold air outbreak; flew in same area as morning flight; steam fog that visible atop ocean surface in a band near SST rise; turbulence observed; icing motivated descents to MinAlt for shedding; supercooled droplets to mixed phase as plane moved downwind; cloud base changes significant as crossed Gulf Stream edge; uptrend in SO_4 offshore and a significant change in the aerosol size distribution between MBL and the coastal PBL
44	2/3/2021	Joint	Statistical Survey	14:10:34	17:23:42	5	14:14:14	17:18:16	Captured transition from SCu clouds to open cell cloud field; possible Asian dust; icing was issue in BCT legs; cloud water collected near and below bases during precipitation
45	2/10/2021	Single-King Air	Statistical Survey	15:05:09	18:43:58	2	N/A	N/A	Falcon ground this and next two flights for maintenance issue
46	2/20/2021	Single-King Air	Statistical Survey	14:50:18	18:04:45	8	N/A	N/A	Cold air outbreak; characterized transition from clear to closed cell to open cell
47	2/21/2021	Single-King Air	Statistical Survey	14:28:01	18:23:45	10	N/A	N/A	Cold air outbreak; characterized transition from clear to closed cell to open cell
48	3/4/2021	Joint	Statistical Survey	17:44:46	20:50:07	6	17:47:39	20:46:46	CALIPSO underflight; first flight with reduced Falcon payload for Winter 2021 campaign
49	3/5/2021	Joint	Statistical Survey	13:43:52	17:11:24	5	13:40:51	17:07:59	Evolution of cold air outbreak cloud field potential high altitude aerosol layer due to dust; high cloud bases and cold clouds
50	3/5/2021	Joint	Statistical Survey	18:40:27	21:56:57	5	18:43:16	21:51:03	Characterized upwind aerosol data feeding the cloud field sampled in first flight; many notes from morning flight apply here too
51	3/8/2021	Joint	Statistical Survey	16:59:05	20:06:56	4	16:57:24	20:19:25	Cold air outbreak conditions; clouds were shallow overall, and appeared to be strongly affected by the overlying dry air; bases were high and the sub-cloud layer seemed to be well-mixed; aerosol gradient was notable with distance downwind; a couple adjacent tracks southwest of OXANA may allow for clear/cloudy contrast

52	3/9/2021	Joint	Statistical Survey	13:57:41	17:16:14	4	13:55:17	17:09:10	Flew around same area as previous day but this day was more cloud-free to allow for contrast; smoke observed close to land due to local burning; Falcon did some wind calibration work
53	3/12/2021	Joint	Statistical Survey	12:39:36	15:58:13	5	12:37:25	16:01:40	Smoke sampled over land and by coast
54	3/12/2021	Joint	Statistical Survey	17:23:19	20:52:59	5	17:19:52	20:47:35	CALIPSO underflight; similar flight plan as morning flight
55	3/20/2021	Joint	Statistical Survey	12:33:31	15:55:44	4	12:30:58	15:53:30	Interesting layer of depolarizing aerosol right above clouds near the end of flight - possible residual layer of sea salt in dry conditions and/or dust
56	3/23/2021	Joint	Statistical Survey	15:56:14	19:56:54	5	16:33:50	19:51:19	Falcon delayed takeoff due to ATC issues; Falcon did wind calibration work; relatively clean day with low aerosol and cloud drop number concentrations
57	3/29/2021	Joint	Statistical Survey	14:53:19	18:45:19	4	14:50:55	18:38:00	ASTER underflight; well defined inversion marking top of clouds; white caps visible most of the flight
58	3/30/2021	Joint	Statistical Survey	12:01:47	15:22:53	3	11:59:42	15:17:14	Good and consistent cloud conditions; thin aerosol layers above cloud deck
59	3/30/2021	Joint	Statistical Survey	17:02:08	20:38:53	5	17:04:52	20:42:23	CALIPSO underflight; relatively high absorption aerosol layer on return track; notable cloud boundary which appeared to be collocated with the Gulf Stream with clear sky over the colder water to the north
60	4/2/2021	Joint	Statistical Survey	12:29:48	16:07:44	9	12:32:40	16:01:06	Cold air outbreak: Deeper cloud structure along track, more precip than usual; sharp offshore N_d gradient
61	4/2/2021	Joint	Statistical Survey	17:25:18	21:07:29	9	17:29:15	21:02:28	Repeated morning track with similar features; last flight with reduced Falcon payload
62	5/13/2021	Joint	Statistical Survey	17:06:41	20:48:23	3	17:03:34	20:22:58	Mostly cloud-free; shorter flight than normal; major transition happened across the SST gradient; well-developed cloud line near the edge of the cloudy region.
63	5/14/2021	Joint	Statistical Survey	12:46:41	16:29:30	4	12:39:53	16:16:56	Complex cloud scene split into two layer maxima with a few clouds developing from the lower layer and connecting to the upper layer which had a more stratiform appearance and

									appeared to be detraining from the developed cumulus below
64	5/14/2021	Joint	Statistical Survey	17:49:41	21:17:03	4	17:41:38	21:14:15	Similar conditions to first flight this day. Falcon focused more on lower clouds as the higher clouds were less defined this flight
65	5/15/2021	Joint	Statistical Survey	17:43:00	21:10:34	4	17:40:20	21:04:18	Dynamic cloud scene with considerable convection
66	5/18/2021	Joint	Statistical Survey	15:30:18	19:03:09	4	15:28:14	18:54:28	Conditions similar to RF65; enhanced aerosol farther offshore compared to the coastal (over water) region
67	5/19/2021	Joint	Statistical Survey	12:31:12	15:55:48	5	12:27:04	15:49:56	Mostly clear air flight
68	5/19/2021	Joint	Statistical Survey	17:39:33	21:04:53	4	17:30:32	20:58:36	CALIPSO underflight; mostly clear air flight
69	5/20/2021	Joint	Statistical Survey	14:59:01	18:42:18	4	15:11:23	18:27:47	Smoke aerosol layers observed
70	5/21/2021	Joint	Statistical Survey	12:27:19	16:00:47	5	12:25:15	16:03:35	Possible cold pool near the turn point; possible smoke/dust aloft; excellent day for cloud water collection with many samples
71	5/21/2021	Joint	Statistical Survey	17:15:43	20:33:33	4	17:20:08	20:42:10	Large number cloud water samples; in some cases it appeared as the cloud was interacting with the surface as fog
72	5/25/2021	Joint	Statistical Survey	15:56:59	19:19:44	4	16:00:04	19:15:03	Nothing too notable; Falcon conducted a higher than normal ACT leg during the 3rd cloud ensemble because King Air noted an elevated aerosol by HSRL
73	5/26/2021	Joint	Statistical Survey	12:37:06	15:54:59	4	12:35:13	15:51:26	Clouds very complicated - it was impossible to follow the standard statistical survey plan; there was at times up to 4 separate layers of cloud and in places there were possible wave clouds which were not constrained to a consistent altitude range
74	5/26/2021	Joint	Statistical Survey	17:21:20	20:31:36	4	17:17:16	20:30:03	High aerosol variability with especially hazy conditions near land
75	6/1/2021	Joint	Statistical Survey	14:31:21	18:05:48	4	14:34:00	17:57:38	Shallow cumulus clouds over land on both the outbound and return legs
76	6/2/2021	Joint	Statistical Survey	12:31:07	15:55:10	4	12:36:32	15:47:25	Considerable convection and precipitation
77	6/2/2021	Joint	Process Study	17:25:19	20:29:11	12	17:22:55	20:41:00	Excellent summertime cumulus characterization flight; Falcon did ~7 legs in cloud during its wall pattern

78	6/5/2021	Joint	Statistical Survey	14:09:33	17:30:32	4	14:06:28	17:16:50	Low clouds/fog stayed too low and Falcon couldn't get underneath; good day for data above low cloud tops; interesting AMS organic features noted at low altitude; good candidate for in situ closure analysis for aerosol properties and comparisons with remote sensors
79	6/7/2021	Joint	Statistical Survey	12:31:53	15:59:51	4	12:28:55	15:52:01	Very shallow MBL noted
80	6/7/2021	Joint	Process Study	17:37:15	20:29:56	14	17:35:00	20:24:32	Multiple cloud levels probed by Falcon in a wall pattern with high number of cloud water samples
81	6/8/2021	Joint	Statistical Survey	12:31:27	15:46:28	4	12:28:28	15:51:21	Quick transition from drizzle near coastline to precipitation over the ocean; data suggested higher levels of coarse aerosol than normal
82	6/8/2021	Joint	Statistical Survey	17:28:09	21:02:26	4	17:31:19	20:58:49	Some aircraft issues made flying typical ensemble legs more challenging
83	6/15/2021	Joint	Statistical Survey	15:57:36	19:10:08	4	16:03:25	19:07:04	Low clouds were quite variable and did not form in a consistent altitude range with multiple cloud layers at times; clouds at one point were too low to allow Falcon to reach its usual low altitudes
84	6/16/2021	Joint	Statistical Survey	14:26:35	18:09:50	5	14:29:55	17:58:20	Uniform conditions during the flight; mostly cloud free
85	6/17/2021	Joint	Statistical Survey	14:30:34	17:29:12	4	14:28:35	17:37:00	ASTER underflight
86	6/22/2021	Joint	Statistical Survey	12:14:35	15:29:04	4	12:17:12	15:31:20	Shallow MBL with tenuous/small clouds; very hazy due to suspected high humidity and sea salt
87	6/24/2021	Joint	Statistical Survey	12:23:15	15:51:35	4	12:20:52	15:37:15	Clouds included significant stratiform cloud connected to embedded cumulus; widespread precipitation both in the sub-cloud environment and observed aloft originating from detraining layers; extensive precipitation challenged the ability to achieve sub-cloud aerosol sampling in many locations
88	6/26/2021	Joint	Statistical Survey	12:28:49	15:53:57	4	12:33:25	15:48:45	Subtropical high conditions; low aerosol concentrations noted
89	6/26/2021	Joint	Statistical Survey	17:25:01	20:49:35	5	17:20:51	20:42:23	Flight originally planned to be process study but changed to stat survey since targets did not build as desired; decent shallow cumulus sampling
90	6/28/2021	Joint	Statistical Survey	12:28:31	15:43:55	4	12:31:10	15:45:57	Mostly shallow cumulus with some developed regions that appeared to be organized as convergence lines/streets

91	6/29/2021	Joint	Statistical Survey	12:16:58	15:34:41	4	12:19:55	15:36:59	Very similar conditions as RF90
92	6/30/2021	Joint	Statistical Survey	12:21:16	15:40:27	4	12:23:54	15:41:41	Relatively low aerosol concentrations; patchy cumulus clouds
93	6/30/2021	Joint	Statistical Survey	17:09:17	20:30:05	5	17:13:33	20:33:48	Similar conditions as morning flight (RF92); crossed over a large discrete cloud clearing east of ZIBUT
94	11/30/2021	Joint	Statistical Survey	16:23:37	19:53:32	4	16:17:54	19:34:39	ATC issues kept Falcon higher than desired at times; well-defined boundary layer with energetic/mixed sub-cloud layer
95	12/1/2021	Joint	Statistical Survey	15:23:20	18:54:36	4	15:20:40	18:45:40	Similar conditions to RF94; cloud bases were high again with a deep well mixed sub-cloud layer; smoke in boundary layer near coast
96	12/7/2021	Joint	Statistical Survey	16:58:05	20:28:35	4	16:55:46	20:17:52	Complex cloud scene split into two layer maxima with a few clouds developing from the lower layer and connecting to the upper layer which had a more stratiform appearance and appeared to be detraining from the developed cumulus below
97	12/9/2021	Joint	Statistical Survey	12:47:48	16:12:26	5	12:52:54	15:54:40	Landed at Quonset State Airport; nice cloud conditions with transitions between open/closed cells; aerosol gradient during flight
98	12/9/2021	Joint	Statistical Survey	17:25:23	20:55:22	6	17:28:54	20:36:05	Return to LaRC from Quonset State Airport; similar conditions as RF97 in morning
99	12/10/2021	Joint	Statistical Survey	17:49:41	21:04:36	4	17:47:11	21:00:38	Military traffic during this flight prevented Falcon from doing most of its typical above cloud top (ACT) legs
100	1/11/2022	Joint	Statistical Survey	13:35:19	17:08:18	7	13:42:50	16:57:58	Cold air outbreak; did upwind work in clear air along with cloud work; P3 from IMPACTS mission flew in general vicinity this flight day
101	1/11/2022	Joint	Statistical Survey	18:34:09	22:05:19	6	18:38:34	21:47:02	Cold air outbreak; icing was more of an issue for Falcon this second flight of the day leading to more MinAlt flying to de-ice
102	1/12/2022	Joint	Statistical Survey	13:22:05	16:38:28	4	13:20:05	16:31:22	Marked gradient in drop number concentration along flight track that appeared to correlate with an increase in the prevalence of precipitating cells
103	1/12/2022	Joint	Statistical Survey	18:00:03	21:18:49	5	17:58:25	21:13:33	CALIPSO underflight; similar conditions to morning flight (RF102)

104	1/15/2022	Joint	Statistical Survey	12:56:34	16:36:53	6	12:50:36	16:29:28	Clouds thickened substantially from near overcast at ZIBUT with ice and liquid precip observed to the east and subsequent breakup of the overcast to broken but deeper cells
105	1/18/2022	Joint	Statistical Survey	13:17:57	16:55:03	8	13:24:32	16:36:33	Cold air outbreak; did upwind work in clear air along with cloud work (similar to RF100)
106	1/18/2022	Joint	Statistical Survey	18:32:53	22:21:00	5	18:31:15	21:54:40	Cold air outbreak; similar to RF101 where the second flight of the day continues sampling the cloud field probed in the morning flight; light precip widespread but with stronger showers associated with cores; strong N_d gradient
107	1/19/2022	Joint	Statistical Survey	13:14:08	16:40:51	4	13:19:53	16:34:10	Complex cloud scene with multiple cloud layers at times
108	1/19/2022	Joint	Statistical Survey	18:35:06	21:59:37	4	18:41:04	21:52:52	Similar conditions as morning flight (RF107)
109	1/24/2022	Joint	Statistical Survey	13:38:57	17:01:11	4	13:34:18	16:45:18	Sharp gradient in MBL height offshore especially once over warmer water where it rapidly deepened and was topped with small cumulus-like clouds
110	1/24/2022	Joint	Statistical Survey	18:15:53	21:39:35	4	18:21:33	21:29:36	Similar conditions as morning flight (RF109)
111	1/26/2022	Joint	Statistical Survey	13:10:52	16:51:45	4	12:56:10	16:28:48	Multiple cloud layers; aerosol layer above cloud at times; interesting AMS organic structure noted
112	1/26/2022	Joint	Statistical Survey	18:07:54	21:45:56	3	18:05:39	21:24:00	Markedly different conditions observed above cloud top during this flight compared to morning flight; dryer conditions in the lower free troposphere than the morning
113	1/27/2022	Joint	Statistical Survey	12:54:53	15:58:18	4	12:57:30	15:50:45	Landed at Providence Airport; very dry above cloud; considerable icing for Falcon during flight; decoupled layers noted
114	1/27/2022	Joint	Statistical Survey	17:32:31	20:58:31	4	17:34:28	20:43:00	Return to LaRC from Providence; cloud scene became even more complex than morning with more evidence of decoupling of the upper part of the cloud layer with sometimes 3 distinct strata; ice imagery data from 2D-S showed differences with morning flight
115	2/1/2022	Joint	Statistical Survey	13:22:28	16:40:01	4	13:24:43	16:31:43	Aerosol gradient observed; thicker regions of the clouds were precipitating and in some regions it was quite significant with visible showers below cloud base

116	2/2/2022	Joint	Statistical Survey	18:19:17	21:59:02	4	18:26:40	21:50:00	Mix of shallow cumulus with some deeper cells with showers and a possible cold pool crossing; MBL had decoupled structure
117	2/3/2022	Joint	Statistical Survey	13:25:51	16:43:35	4	13:23:47	16:34:23	Sub-cloud environment was warmer and more humid than normal
118	2/3/2022	Joint	Statistical Survey	18:10:48	21:24:52	4	18:08:29	21:28:10	Similar conditions as morning flight (RF117)
119	2/5/2022	Joint	Statistical Survey	13:44:32	17:05:26	3	13:42:26	16:58:58	Characterized the initial stages of the post-frontal environment as it advects offshore; a 2nd flight this day was planned but scrubbed due to maintenance issue
120	2/15/2022	Joint	Statistical Survey	13:34:04	17:06:08	4	13:31:40	16:48:02	Cumulus feeding an upper stratiform layer near the inversion; in thicker cloud regions, some mixed phase and precipitation observed with sub-cloud drizzle below the melting level; elevated aerosol by coast
121	2/15/2022	Joint	Statistical Survey	18:26:24	22:22:17	3	18:07:41	22:03:21	Similar conditions as morning flight (RF120)
122	2/16/2022	Joint	Statistical Survey	13:25:05	16:50:49	3	13:22:18	16:31:40	Clouds had the appearance of an overcast near the inversion with cumulus feeding from below; sulfate-rich aerosol
123	2/16/2022	Joint	Statistical Survey	18:24:32	22:03:02	3	18:28:10	21:59:34	Complex cloud and boundary layer structure; moisture profile near coast suggested marine air was previously lofted and then had become disconnected from the surface; N_d gradient offshore
124	2/19/2022	Joint	Statistical Survey	13:32:00	17:25:52	2	13:51:21	17:07:23	Multiple cloud layers; airspace restrictions (rocket launch from Wallops) affected areas we could fly
125	2/19/2022	Joint	Statistical Survey	18:36:30	22:06:48	3	18:34:55	22:01:19	Continued airspace restrictions; irregularly shaped particles detected by 2D-S
126	2/22/2022	Joint	Statistical Survey	13:58:48	17:15:43	3	13:34:25	16:55:03	Falcon ascended higher than normal at times to sample an aerosol layer aloft flagged by HSRL-2
127	2/22/2022	Joint	Statistical Survey	18:43:33	22:16:25	3	18:41:10	21:59:38	Areas sampled with relatively low aerosol/cloud number concentrations
128	2/26/2022	Joint	Statistical Survey	13:23:33	16:24:30	4	13:18:30	16:03:13	Landed at Providence Airport; extensive low cloud under a dense high cloud deck for most of the flight
129	2/26/2022	Single-Falcon	Statistical Survey	20:56:17	22:59:23	0	18:13:41	20:52:34	Return to LaRC from Providence; similar conditions as morning flight; due to a maintenance issue with King Air it flew back but could not collect data

130	3/2/2022	Joint	Statistical Survey	19:10:25	22:53:14	4	19:08:19	22:29:10	Unicorn aerosol module; aerosol enhancements above boundary layer
131	3/3/2022	Joint	Statistical Survey	13:32:56	16:58:32	3	13:30:32	16:52:08	Unicorn aerosol module; similar to RF130 there was relatively high AOD for the winter season with interesting aerosol structure throughout flight
132	3/3/2022	Joint	Statistical Survey	18:32:07	21:52:14	3	18:27:27	21:42:40	Sampled different airmasses during flight
133	3/4/2022	Joint	Statistical Survey	13:45:14	17:28:27	4	13:43:00	17:03:22	At the far turnpoint we crossed the convergence line that was flown the previous day
134	3/4/2022	Joint	Statistical Survey	18:42:03	22:22:29	3	18:32:00	21:54:27	Markedly different conditions from the morning flight and a good contrast case for two flights on same day
135	3/7/2022	Joint	Statistical Survey	13:28:48	16:51:59	3	13:25:44	16:44:18	On the way out, high aerosol loading above boundary layer with areas of elevated aerosol depolarization near the top of the residual layer
136	3/7/2022	Single-Falcon	Statistical Survey	N/A	N/A	0	18:39:20	21:57:41	King Air experienced maintenance issue prior to take off and was grounded; similar conditions to morning flight for Falcon
137	3/13/2022	Joint	Process Study	12:28:41	16:24:46	11	12:35:23	16:14:50	Excellent cold air outbreak day with marine boundary layer winds westerly/northwesterly and a 'transition' (from solid to open cloud field) within reach; Falcon conducted mini "walls" upwind, at, and downwind of the transition zone; steam fog observed
138	3/13/2022	Joint	Statistical Survey	17:32:47	21:22:10	3	17:36:37	20:48:16	Extending the line from morning flight farther upwind to characterize clear air
139	3/14/2022	Joint	Statistical Survey	12:32:35	15:52:52	3	12:35:48	15:45:45	Clouds had a decoupled appearance with small cumulus topping a deep mixed layer with some cumulus developing up to a more extensive stratiform near the inversion; drizzle observed; generally clean aerosol conditions this flight
140	3/14/2022	Joint	Statistical Survey	17:22:26	20:49:25	3	17:26:15	20:44:46	Similar conditions to RF139; smoke plume emanating from a woodland fire sampled on the inbound leg over North Carolina
141	3/18/2022	Joint	Statistical Survey	14:55:12	18:15:47	3	14:48:07	17:59:00	Lots of fog in the morning that prevented an earlier flight; clouds were sometimes too low to get under
142	3/22/2022	Joint	Statistical Survey	12:50:47	15:23:47	3	12:45:45	15:25:58	First flight to Bermuda; mostly cloud-free and indications of

									aerosol gradient offshore towards Bermuda
143	3/22/2022	Joint	Statistical Survey	17:12:14	21:00:01	4	17:36:21	21:12:02	Return from Bermuda to LaRC; owing to lack of a functional power cart at Bermuda, some Falcon instruments needed extra time to stabilize to collect good data this flight
144	3/26/2022	Joint	Statistical Survey	12:14:27	16:01:09	3	12:30:09	16:12:35	Dust, smoke, possibly pollen; unicorn aerosol module
145	3/26/2022	Joint	Statistical Survey	17:22:48	21:20:22	3	17:31:10	21:23:49	Similar aerosol conditions as RF145 but with higher cloud coverage
146	3/28/2022	Joint	Statistical Survey	16:52:05	20:49:49	4	16:49:41	20:19:50	Nothing too noteworthy documented other than it being a good data for added statistics
147	3/29/2022	Joint	Statistical Survey	12:41:46	16:34:31	4	12:34:53	16:21:04	Excellent cold air outbreak day; flew counterclockwise partly to help with aircraft coordination on the most important leg aligned with the boundary layer winds; did upwind aerosol characterization and cloud work
148	3/29/2022	Joint	Process Study	17:48:08	21:26:17	4	17:44:42	21:33:17	Similar conditions to morning flight; Falcon conducted mini "walls" like RF137
149	5/3/2022	Joint	Statistical Survey	13:45:00	16:56:25	4	13:48:45	16:51:01	Convective data with relatively high AOD and smoke aerosol (possibly from New Mexico area)
150	5/5/2022	Joint	Statistical Survey	12:27:06	15:46:26	4	12:23:27	15:41:20	Landed at Providence Airport; high number of cloud water samples collected as unbroken long sampling times in cloud were achieved
151	5/5/2022	Joint	Statistical Survey	17:10:28	20:40:49	4	17:14:06	20:30:32	Return to LaRC from Providence; similar to morning flight but with less extensive cloud coverage
152	5/10/2022	Joint	Statistical Survey	12:31:00	15:55:21	4	12:34:05	15:52:00	Pronounced 'pure' sea salt aerosol case; hard to get below clouds at times as they were low; drizzle was frequent
153	5/16/2022	Joint	Statistical Survey	12:21:28	15:40:39	4	12:24:44	15:37:17	Nothing too noteworthy documented other than it being a good data for added statistics
154	5/16/2022	Joint	Statistical Survey	17:11:51	20:38:43	4	17:15:35	20:29:09	Convective weather led to some flight deviations this flight
155	5/17/2022	Joint	Statistical Survey	14:04:10	17:32:00	3	13:50:37	17:00:08	Unicorn aerosol module
156	5/18/2022	Joint	Statistical Survey	12:27:10	15:25:35	4	12:25:31	15:28:34	Flight to Bermuda; offshore gradient in aerosol parameters

157	5/18/2022	Joint	Statistical Survey	17:02:45	21:12:33	4	17:25:45	20:55:33	Return from Bermuda to Langley; CALIPSO underflight; possible indications of bioaerosol
158	5/20/2022	Joint	Statistical Survey	13:33:43	16:55:37	4	13:38:25	16:58:14	Hazy day with indications of bioaerosol and multiple layers of aerosol
159	5/21/2022	Joint	Statistical Survey	12:09:49	15:14:00	5	12:13:30	15:06:39	To Bermuda
160	5/21/2022	Joint	Statistical Survey	16:51:03	20:30:27	5	17:07:18	20:19:46	Return from Bermuda to Langley; CALIPSO underflight
161	5/31/2022	Joint	Statistical Survey	12:33:39	16:09:35	3	12:36:07	15:56:16	Transit to Bermuda for 3-week deployment based in Bermuda
162	6/2/2022	Single-Falcon	Statistical Survey	N/A	N/A	0	11:19:14	14:19:17	King Air experienced maintenance issue prior to take off; Tudor Hill spiral
163	6/2/2022	Single-Falcon	Process Study	N/A	N/A	0	16:03:00	19:01:26	Falcon conducted wall patterns in both cloud and cloud-free air; Tudor Hill spiral
164	6/3/2022	Single-Falcon	Statistical Survey	N/A	N/A	0	12:48:53	15:10:51	Flight cut short as Falcon was needed to assist with King Air maintenance issue
165	6/5/2022	Joint	Statistical Survey	11:02:20	14:26:12	4	11:08:21	14:20:20	Flight executed early to avoid an approaching tropical storm
166	6/7/2022	Joint	Statistical Survey	11:17:40	15:00:14	5	11:38:43	15:02:09	Overpass of BIOS underwater glider; Tudor Hill spiral
167	6/7/2022	Joint	Statistical Survey	15:57:31	19:28:19	5	16:14:20	19:33:24	Uniform HSRL-2 data curtains for aerosol during flight; free troposphere mostly clean; Tudor Hill spiral
168	6/8/2022	Joint	Statistical Survey	12:56:12	16:14:14	5	13:12:41	16:08:58	ASTER underflight; fairly clean again in free troposphere like previous flight
169	6/8/2022	Joint	Statistical Survey	17:13:56	20:53:50	5	17:32:12	20:56:22	Tudor Hill spiral
170	6/10/2022	Joint	Statistical Survey	11:57:01	15:35:19	7	12:20:04	15:37:27	ASTER underflight; possible African dust; Tudor Hill spiral
171	6/10/2022	Joint	Process Study	17:08:55	21:13:31	16	17:30:18	20:51:35	Exceptional flight (one of the best) in that two adjacent Falcon walls were conducted with contrasts in cloud development along with varying degrees of dust influence
172	6/11/2022	Joint	Statistical Survey	12:00:01	13:55:07	4	12:24:00	16:00:54	Continued influence of what seems to be African dust; Tudor Hill spiral
173	6/11/2022	Joint	Process Study	17:09:36	20:55:48	23	17:24:10	20:45:27	More African dust; record number of dropsondes for an ACTIVATE flight (23); excellent wall profiles of 2 cloud systems
174	6/13/2022	Joint	Statistical Survey	11:15:17	14:55:27	3	11:43:05	14:59:05	Got into cleaner air farther removed from dust to allow for contrasting; Tudor Hill spiral
175	6/13/2022	Joint	Statistical Survey	16:26:06	19:59:59	5	16:49:10	20:16:30	CALIPSO underflight; Tudor Hill spiral

176	6/14/2022	Joint	Process Study	12:59:24	16:47:39	5	13:28:57	16:44:12	Dust influence again; Falcon conducted another wall pattern with high number of legs at different altitude in the cloud system
177	6/16/2022	Single-King Air	Statistical Survey	10:59:45	12:51:24	3	N/A	N/A	Falcon experienced maintenance issue prior to take off and stayed on ground
178	6/17/2022	Joint	Statistical Survey	12:57:16	16:47:22	8	13:25:31	16:57:04	Tudor Hill spiral
179	6/18/2022	Joint	Statistical Survey	11:56:10	15:37:35	5	12:05:15	15:23:37	Return from Bermuda; some flight deviations needed to account for thunderstorm activity

Table 3. Summary of King Air instrumentation and measurements. [§]Uncertainties, which represent a combination of measurement precision and accuracy, are presented for typical measurement conditions. *"*x* m / *y* m" indicates *x*-m vertical resolution and *y*-m horizontal resolution along track. [†]Cross-track by along-track. [‡] Non-imaging: along-track product with single cross-track elements for RSP. Products under

Measured/Retrieved Parameter	Resolution	Uncertainty[§]	Reference/Notes

development are omitted from this table and readers are referred to sect. 3 for more description.

Instrument and Relation to Objectives				
HSRL-2 (aerosol and cloud properties; prototype of possible satellite aerosol-cloud lidar retrievals)	Particulate Backscatter Profiles (355, 532, and 1064 nm)	30 m x 1 km*	0.2 $Mm^{-1}sr^{-1}$	Hair et al., 2008; Burton et al., 2015; Burton et al., 2018
	Particulate Depolarization (355, 532, and 1064 nm)	30 m x 1 km*	~ 2-5 %	See Burton et al. (2015) for details regarding aerosol depolarization uncertainties; uncertainty values are approximate and dependent on scattering levels
	Particulate Extinction Profiles (355 and 532 nm)	225 m x 6 km*	0.01 km^{-1}	
	Particulate Lidar Ratio (355 and 532 nm)	225 m x 6 km*	~10 %	Uncertainty values are approximate and dependent on scattering levels
	Ångstrom Exponent - Extinction (532/355 nm)	225 m x 6 km*	~10 %	Uncertainty values are approximate and dependent on scattering levels
	Ångstrom Exponent - Backscatter (532/355 nm, 1064/532 nm)	30 m x 1 km*	~10 %	Uncertainty values are approximate and dependent on scattering levels
	Aerosol Optical Depth (355, 532 nm)			
	1-D Full Column (Aircraft-to-Surface)	Integrated product x 6 km*	0.02	
	2-D Vertically Resolved (Altitude-Bin-to-Surface)	30 m x 6 km*	≤ 0.02	
	Mixed Layer Height	15 m x 1 km*	~100 m	Scarino et al., 2014
	Aerosol Type (Qualitative)	135 m x 6 km*	N/A	Burton et al., 2012
	Surface Wind Speed (10 m)	1.25 m x 1 km*	0.16 $m\ s^{-1}$ (± 1.94 $m\ s^{-1}$)	Dmitrovic et al., forthcoming
	Cloud Top Height (1-D)	1.25 m x 50 m*	~ 5 m	Hair et al., forthcoming; Cloud top height uncertainties are approximate and based upon a threshold of the backscatter
	Cloud Top Extinction	1.25 m x 50 m*	< 20 %	Still being evaluated; assumes liquid-phase only clouds
	Cloud Top Lidar Ratio (extinction-to-backscatter)	Integrated product x 50 m*	< 20 %	Still being evaluated; assumes liquid-phase only clouds
	10 m Ocean Subsurface Particulate Backscatter (532 nm)	N/A x 1 km*	< 10%	Schulien et al., 2017; Only available for select flights
RSP (aerosol and cloud properties; development of	Aerosol Fine-Mode Optical Depth (column)	100 m x 600 m†	0.04	Stamnes et al., 2018
	Aerosol Coarse-Mode Optical Depth (column)	100 m x 600 m†	0.02	Stamnes et al., 2018

combined lidar-polarimeter aerosol-cloud retrievals)	Aerosol Size: Fine-mode Effective Radius (column)	100 m x 600 m†,‡	0.02 µm	Stamnes et al., 2018
	Aerosol Size: Fine-Mode Effective variance (column)	100 m x 600 m†,‡	0.05	Stamnes et al., 2018
	Aerosol Size: Coarse-Mode Effective Variance (column)	100 m x 600 m†,‡	0.07	Stamnes et al., 2018
	Aerosol Fine-Mode Single Scatter Albedo (column)	100 m x 4 km†,‡	0.02	Stamnes et al., 2018
	Aerosol Fine-Mode Real Refractive Index (column)	100 m x 4 km†,‡	0.03	Stamnes et al., 2018
	Aerosol Particle Number Concentration	100 m x 4 km†,‡	10-70%	Schlosser et al., 2022
	Aerosol Top Height	100 m x 4 km†,‡	< 1 km	Wu et al., 2016
	Surface Wind Speed	100 m x 4 km†,‡	0.5 m s^{-1}	Stamnes et al., 2018
	Chlorophyll-a Concentration	100 m x 4 km†,‡	26%	Stamnes et al., 2018
	Ocean diffuse attenuation coefficient	100 m x 4 km†,‡	40%	Stamnes et al., 2018
	Ocean hemispherical backscatter coefficient	100 m x 4 km†,‡	10%	Stamnes et al., 2018
	Cloud Flag/Test	100 m x 100 m†,‡	10%	Comparisons with HSRL-2 cloud detection
	Cloud Top Phase Index	100 m x 600 m†,‡	10%	Van Diedenhoven et al., 2012
	Cloud Top Effective Radius	100 m x 600 m†,‡	1 µm/10%	Alexandrov et al., 2012a/b
	Cloud Top Effective Variance	100 m x 600 m†,‡	0.05/50%	Alexandrov et al., 2012a/b
	Cloud Mean Effective Radius	100 m x 600 m†,‡	20%	Alexandrov et al., 2012a/b
	Cloud Optical Depth	100 m x 600 m†,‡	10%	Nakajima and King, 1990
	Liquid Water Path	100 m x 600 m†,‡	25%	Uncertainties for optical depth and effective radius added in quadrature
	Columnar Water Vapor (Above Surface or Cloud)	100 m x 600 m†,‡	10%	Nielsen et al., forthcoming
	Cloud Top Height	100 m x 600 m†,‡	15%	Sinclair et al., 2017
	Cloud Droplet Number Concentration	100 m x 600 m†,‡	25%	Sinclair et al., 2019
	Cloud Albedo	100 m x 600 m†,‡	10%	Radiometric accuracy of 5%
Vaisala NRD41 Dropsonde (meteorological state)	Latitude/Longitude	/~11 m	NA	Vömel et al., 2021; Vömel et al., forthcoming
	Altitude		NA	
	GPS Altitude		NA	
	Pressure		0.5 hPa	
	Temperature		0.2°C	
	Dew Point Temperature			
	Relative Humidity		3%	
	Horizontal Wind (u and v components)		0.5 m s^{-1}	
	Vertical Wind		1 m s^{-1}	
Applanix 610 (Navigational)	Day and Time	1 s	NA	
	Latitude/Longitude	1 s	1.5 m/1.5 m	
	GPS Altitude	1 s	3 m	
	Ground Speed	1 s	0.03 m s^{-1}	

Vertical Speed	1 s	3 m s^{-1}
True Heading	1 s	0.03°
Track Angle	1 s	0.03°
Drift Angle	1 s	NA
Pitch Angle	1 s	0.005°
Roll Angle	1 s	0.005°

Table 4. Summary of camera details on the King Air and HU-25 Falcon. The first column represents the research flight number for which a certain set of cameras were installed to replace pre-existing ones with the same swap-out dates for the nadir and forward cameras. HFOV = horizontal field of view. The time resolution of the cameras was 1-2 seconds.

	King Air - Nadir Camera						King Air & HU-25 Falcon - Forward Camera					
RF	Make	Model	Lens	HFOV	Focal Length	Aperture	Make	Model	Lens	HFOV	Focal Length	Aperture
1	Garmin	VIRB Ultra 30	None	62	N/A	N/A	GoPro	Hero 6 Black	None	N/A	N/A	N/A
41	Garmin	VIRB Ultra 30	None	62	N/A	N/A	Axis	F-1005-E	None	113	2.8 mm	2
62	Axis	F-1005-E	None	113	2.8 mm	2	Axis	F-1005-E	None	113	2.8 mm	2
100	Axis	F-1005-E	M12 16mm F1.8	22	16 mm	1.8	Axis	F-1005-E	None	113	2.8 mm	2
149	Axis	F-1005-E	M12 6mm F1.9	56	6 mm	1.9	Axis	F-1005-E	None	113	2.8 mm	2

Table 5. Summary of HU-25 Falcon instrumentation and measurements.

Instrument	Measured Parameter	Uncertainty	Size Range (µm)	Time Resolution (s)	Reference/Notes
		Aerosol Particles			
BMI Counterflow Virtual Impactor vs. Isokinetic Inlet	Inlet Flag	NA	NA	1	
TSI-3776 Condensation Particle Counter (CPC)	Particle Concentration	10%	0.003 - 5	1	Moore et al., 2017
TSI-3772 CPC	Particle Concentration	10%	0.01 - 5	1	Moore et al., 2017
TSI-3772 with Thermal Denuder (350° C)	Nonvolatile (350°C) Particle Concentration	10%	0.01 - 5	1	Moore et al., 2017
TSI Scanning Mobility Particle Sizer (SMPS); Model 3085 DMA, Model 3776 CPC, and Model 3088 Neutralizer	Total and Nonvolatile Dry Aerosol Size Distributions	20%	0.003–0.1	45	Moore et al., 2017
TSI-3340 Laser Aerosol Spectrometer (LAS)		20%	0.1–5	1	Froyd et al., 2019
TSI-3563 Nephelometer	Dry Scattering Coefficient (450, 550, and 700 nm)	20%	<1 (2021-2022), < 5 (2020)	1	Ziemba et al., 2013
TSI-3563 Nephelometer with 80% humidification	f(RH) for Scattering (450, 550, and 700 nm)	20%	<1 (2021-2022), < 5 (2020)	1	Ziemba et al., 2013
Radiance Research Particle Soot Absorption Photometer (PSAP)	Aerosol Absorption (470, 532, and 660 nm)	15%	<5	1	Mason et al., 2018
Aerodyne HR-ToF-AMS	Non-refractory Chemically Resolved Mass Concentration	<50%	0.06-0.6	25	DeCarlo et al., 2008
DMT Cloud Condensation Nuclei (CCN) spectrometer	CCN Concentration and Spectra	10% 0.04 % SS	<5	1	Moore et al., 2009
BMI PILS Coupled to Offline Ion Chromatography	Water-Soluble Aerosol Chemical Composition	<20% (species dependent)	<5	300-420	Sorooshian et al., 2006
		Clouds			
DMT Cloud Droplet Probe (CDP)	Aerosol and Cloud Droplet Number Concentration, Liquid Water Content, Effective Radius/Variance	20%	2-50	1	Lance et al., 2012
DMT Cloud and Aerosol Spectrometer (CAS)	Aerosol and Cloud Droplet Number Concentration, Liquid Water Content, Effective Radius/Variance	20%	0.5-50	1	Baumgardner et al., 2001; Lance et al., 2012
SPEC Inc. Fast Cloud Droplet Probe (FCDP)	Aerosol and Cloud Droplet Number Size Distribution, Liquid Water Content, Effective Diameter, Median Volume Diameter	15-50%	3-50	1	Kirschler et al., 2022

SPEC Inc. Two-Dimensional Stereo (2D-S) Vertical-Arm	Cloud Number Size Distribution for Liquid/Ice/Total, Liquid and Ice Water Content, Ice Flag, Effective Diameter for Liquid/Ice/Total, Median Volume Diameter for Liquid and Total	15-60%	29–1465	1	Kirschler et al., in prep
SPEC Inc. Two-Dimensional Stereo (2D-S) Horizontal-Arm	same as 2D-S Vertical Arm	15-60%	29–1465	1	Kirschler et al., in prep
AC3 and offline chemistry	Cloud Water Chemical Composition	<20% (species dependent)	>8 (droplet diameter)	Function of cloud LWC	Crosbie et al., 2018
		Meteorological State Parameters and Trace Gases			
Applanix 610 (Navigational)	Day and Time	NA	N/A	1/0.05	
	Latitude/Longitude	1.5 m/1.5 m	N/A	1/0.05	
	GPS Altitude	3 m	N/A	1/0.05	
	Pressure Altitude	3 m	N/A	1/0.05	
	Ground Speed	0.03 m s^{-1}	N/A	1/0.05	
	Vertical Speed	3 m s^{-1}	N/A	1/0.05	
	True Heading	0.03°	N/A	1/0.05	
	True Air Speed	5%	N/A	1/0.05	
	Track Angle	0.03°	N/A	1/0.05	
	Drift Angle	NA	N/A	1/0.05	
	Pitch Angle	0.005°	N/A	1/0.05	
	Roll Angle	0.005°	N/A	1/0.05	
5-port pressure system (TAMMS)	3-D Winds	w: 10 cm/s	N/A	0.05	Thornhill et al., 2003
		u,v: 50 cm/s	N/A		
Rosemount 102 Sensor	Temperature	0.5°C	N/A	0.05	
Heitronics KT-15 Infrared Thermometer	Infrared Surface Temperature	5%	N/A	1 s	
Diode Laser Hygrometer (DLH)	Water Vapor	5% or 0.1 ppmv	N/A	<0.05	Diskin et al., 2002
Picarro model G2401-m	CO, CO_2, CH_4	5 ppb (CO)	N/A	2.5	DiGangi et al., 2021
		0.1 ppm (CO_2)		2.5	
		1 ppb (CH_4)		2.5	
2B Tech. Inc. model 205	O_3	6 ppb	N/A	2	Wei et al., 2021

Table 6. MERRA-2 data fields sampled along the Falcon flight tracks during ACTIVATE (see sect. 5.5). STP = standard temperature (0°C) and pressure (1013.25 hPa).

Variable Name	Unit	Field
Time_Stop	seconds	Number of seconds from 00:00 UTC
Lat_flight	deg	Latitude
Lon_flight	deg	Longitude
press_flight	hPa	Pressure calculated from aircraft pressure altitude
M2_CO	ppbv	Carbon monoxide volume mixing ratio
M2_O3	ppbv	Ozone volume mixing ratio
M2_DMS	ppbv	Dimethylsulphide volume mixing ratio
M2_SO2	ppbv	Sulphur dioxide volume mixing ratio
M2_MSA	µg.m^{-3}	Methanesulphonic acid concentration at STP
M2_SO4	µg.m^{-3}	Sulphate aerosol concentration at STP
M2_SS001	µg.m^{-3}	Sea salt concentration (bin 001, 0.03-0.1 µm) at STP
M2_SS002	µg.m^{-3}	Sea salt concentration (bin 002, 0.1-0.5 µm) at STP
M2_SS003	µg.m^{-3}	Sea salt concentration (bin 003, 0.5-1.5 µm) at STP
M2_SS004	µg.m^{-3}	Sea salt concentration (bin 004, 1.5-5 µm) at STP
M2_SS005	µg.m^{-3}	Sea salt concentration (bin 005, 5-10 µm) at STP
M2_DU001	µg.m^{-3}	Dust concentration (bin 001, 0.1-1.0 µm) at STP
M2_DU002	µg.m^{-3}	Dust concentration (bin 002, 1.0-1.5 µm) at STP
M2_DU003	µg.m^{-3}	Dust concentration (bin 003, 1.5-3.0 µm) at STP
M2_DU004	µg.m^{-3}	Dust concentration (bin 004, 3.0-7.0 µm) at STP
M2_DU005	µg.m^{-3}	Dust concentration (bin 005, 7.0-10 µm) at STP
M2_BCPHILIC	µg.m^{-3}	Hydrophilic black carbon concentration at STP
M2_BCPHOBIC	µg.m^{-3}	Hydrophobic black carbon concentration at STP
M2_OCPHILIC	µg.m^{-3}	Hydrophilic organic carbon (Particulate Matter) concentration at STP
M2_OCPHOBIC	µg.m^{-3}	Hydrophobic organic carbon (Particulate Matter) concentration at STP
M2_stdPTfac	1	Factor used to convert µg.m^{-3} at ambient conditions to µg.m^{-3} at STP
M2_RH	%	Relative humidity
M2_T	K	Air temperature
M2_QI	kg.kg^{-1}	Mass fraction of cloud ice water
M2_QL	kg.kg^{-1}	Mass fraction of cloud liquid water
M2_QV	kg.kg^{-1}	Specific humidity

Table 7. Summary of where to access different datasets and resources described in this paper.

Dataset/Resource	Paper Section	Website	DOI
All aircraft instrument data	3-4	https://asdc.larc.nasa.gov/project/ACTIVATE	10.5067/SUBORBITAL/ACTIVATE/DATA001
Falcon merge files	4.8	https://asdc.larc.nasa.gov/project/ACTIVATE/ACTIVATE_Merge_Data_1	10.5067/ASDC/SUBORBITAL/ACTIVATE_Merge_Data_1
Flight reports	5.1	https://asdc.larc.nasa.gov/project/ACTIVATE/pdocuments	N/A
Falcon leg index	5.2	https://asdc.larc.nasa.gov/project/ACTIVATE/ACTIVATE_MetNav_AircraftInSitu_Falcon_Data_1	10.5067/ASDC/ACTIVATE_MetNav_AircraftInSitu_Falcon_Data_1
Aircraft collocation product	5.3	Data: https://asdc.larc.nasa.gov/project/ACTIVATE/ACTIVATE_Miscellaneous_Data_1	10.5067/ASDC/SUBORBITAL/ACTIVATE_Miscellaneous_Data_1
Aircraft collocation product	5.3	Code: https://doi.org/10.6084/m9.figshare.20489442.v2	10.6084/m9.figshare.20489442.v2
Cloud detection neural network algorithm	5.4	https://asdc.larc.nasa.gov/project/ACTIVATE/ACTIVATE_Miscellaneous_Data_1	10.5067/ASDC/SUBORBITAL/ACTIVATE_Miscellaneous_Data_1
MERRA-2 along flight tracks	5.5	https://asdc.larc.nasa.gov/project/ACTIVATE/ACTIVATE_Model_Data_1	10.5067/ASDC/SUBORBITAL/ACTIVATE_Model_Data_1
FLEXPART trajectory data	5.6	https://asdc.larc.nasa.gov/ACTIVATE/ACTIVATE-FLEXPART_1	10.5067/ASDC/SUBORBITAL/ACTIVATE-FLEXPART_1
MODIS	5.7	https://asdc.larc.nasa.gov/project/ACTIVATE/ACTIVATE-MODIS-MERRA2_1	10.5067/ASDC/SUBORBITAL/ACTIVATE-MODIS-MERRA2_1
GOES-16	5.7	https://asdc.larc.nasa.gov/ACTIVATE/ACTIVATE-Satellite_1	10.5067/ASDC/SUBORBITAL/ACTIVATE-Satellite_1
MERRA-2	5.7	https://asdc.larc.nasa.gov/project/ACTIVATE/ACTIVATE-MODIS-MERRA2_1	10.5067/ASDC/SUBORBITAL/ACTIVATE-MODIS-MERRA2_1
Open data workshop recordings and slides	7	https://asdc.larc.nasa.gov/news/activate-data-webinar-materials	N/A

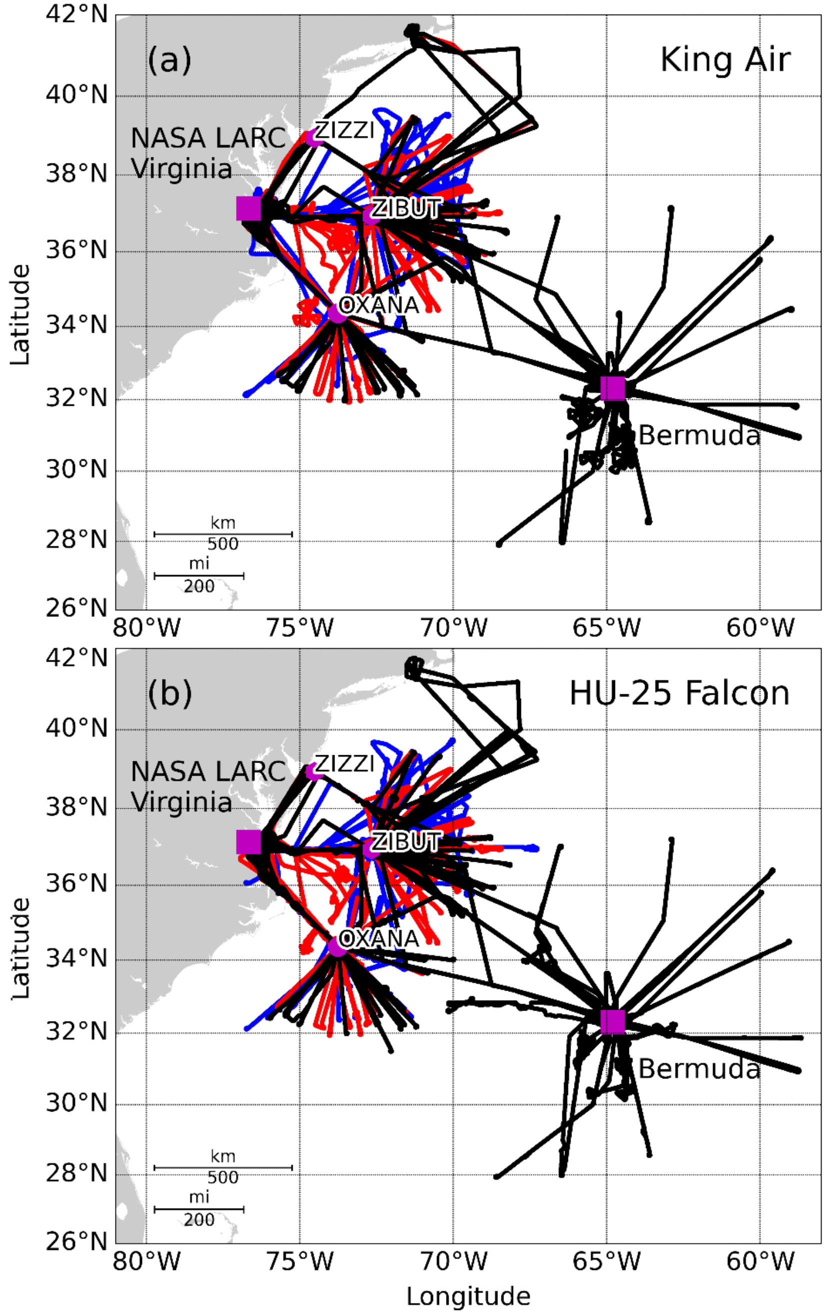

Figure 1: Flight tracks for the (a) King Air and (b) HU-25 Falcon across all three years of flights (blue = 2020, red = 2021, black = 2022). ZIBUT and OXANA are two waypoints used in most flights to adhere to air traffic control restrictions, while ZIZZI was less commonly used.

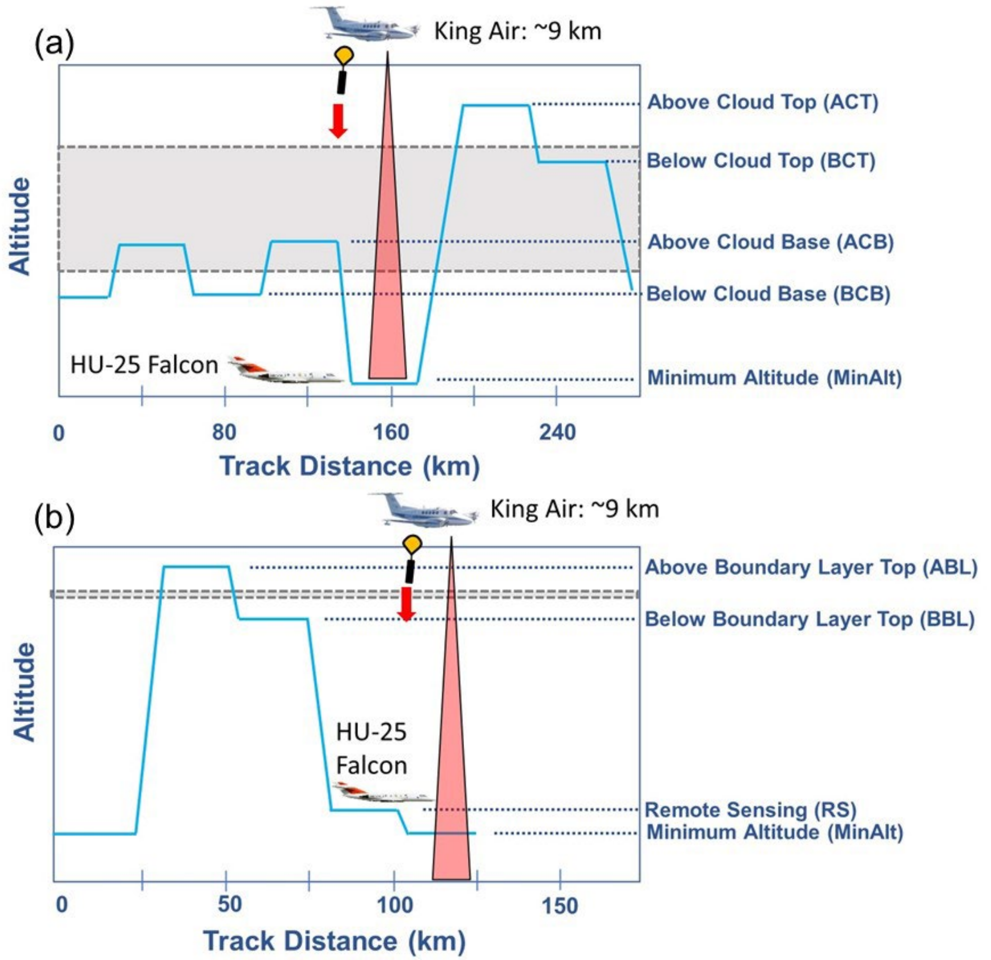

Figure 2: (a) Nominal flight pattern constituting a "cloud ensemble" as part of ACTIVATE flights whereby the Falcon conducts stairstepping (shown in light blue lines) at various levels (~3 min each usually) below, in, and immediately above boundary layer clouds. Note that MinAlt represents the lowest altitude the Falcon could operationally fly at (~150 m above sea level). The King Air flies overhead around ~9 km. The gray shaded area represents a cloud. Typical statistical survey flights included ~3 cloud ensembles. (b) Nominal flight pattern for "clear ensembles" whereby the Falcon stairsteps at levels immediately above and below the boundary layer top (represented by the horizontal gray bar) and legs near the Falcon's lowest operational altitude. The Remote Sensing leg was an additional leg just above the MinAlt leg to facilitate data comparisons between in situ Falcon instruments and King Air remote sensors very near the ocean surface. The vertical axes are compressed to show both aircraft.

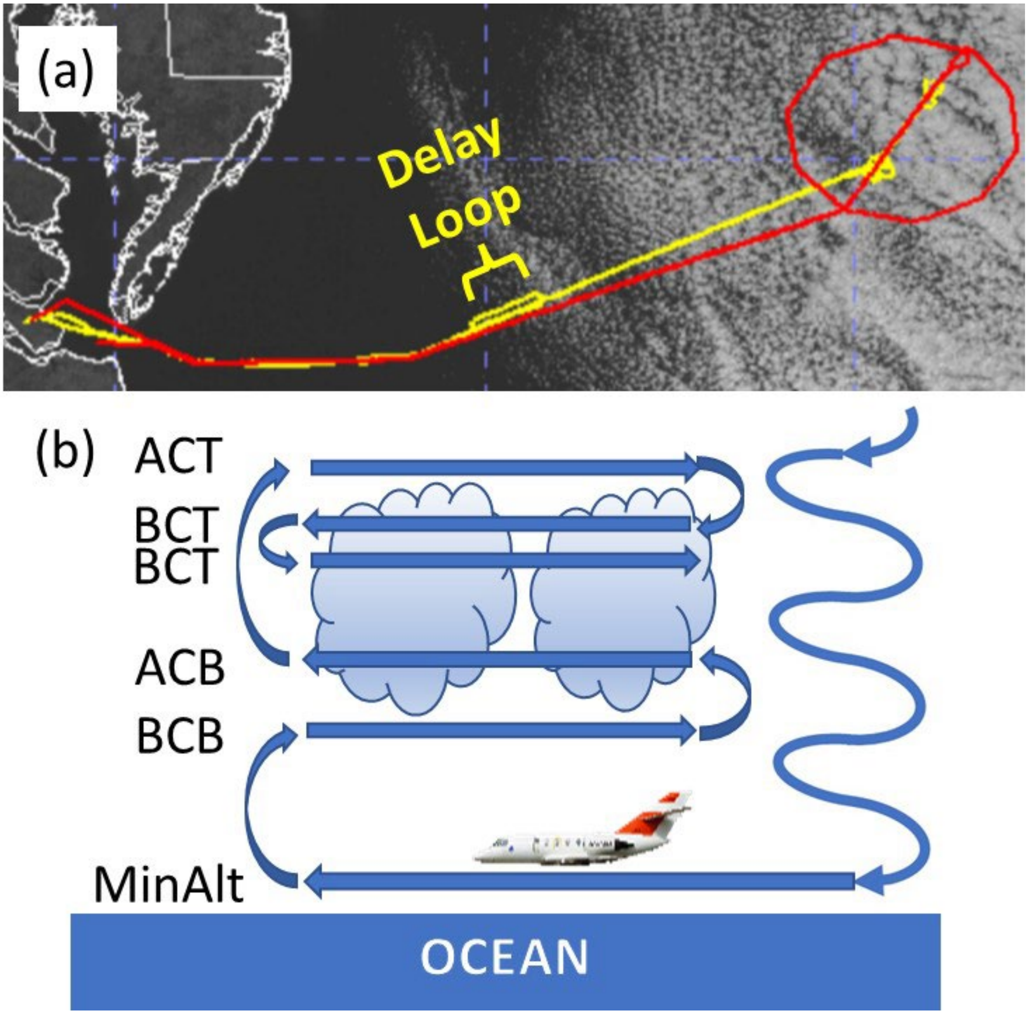

Figure 3: (a) Visual summary of Research Flight 13 (1 March 2020, L1) tracks for both the (yellow) Falcon and (red) King Air overlaid on GOES-16 imagery (UTC 15:21). Highlighted in the flight is a "delay loop" (described in sect. 2.4) executed by the Falcon to improve coordination with the King Air. (b) The generic Falcon pattern used in process study flights including stacked level legs ("wall") with spiral soundings before and after the wall; meanwhile the King Air (not shown in panel b) flies aloft characterizing the same area. In this flight, in place of a spiral sounding at the end of a wall, the Falcon conducted a slant descent from the last BCT leg to a subsequent MinAlt leg.

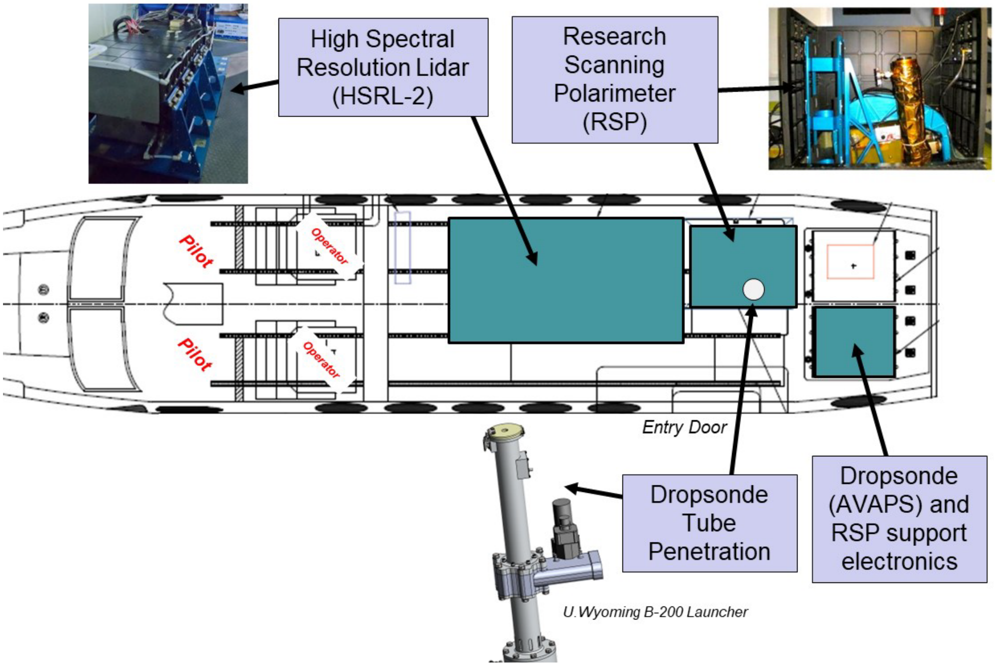

Figure 4: King Air interior layout.

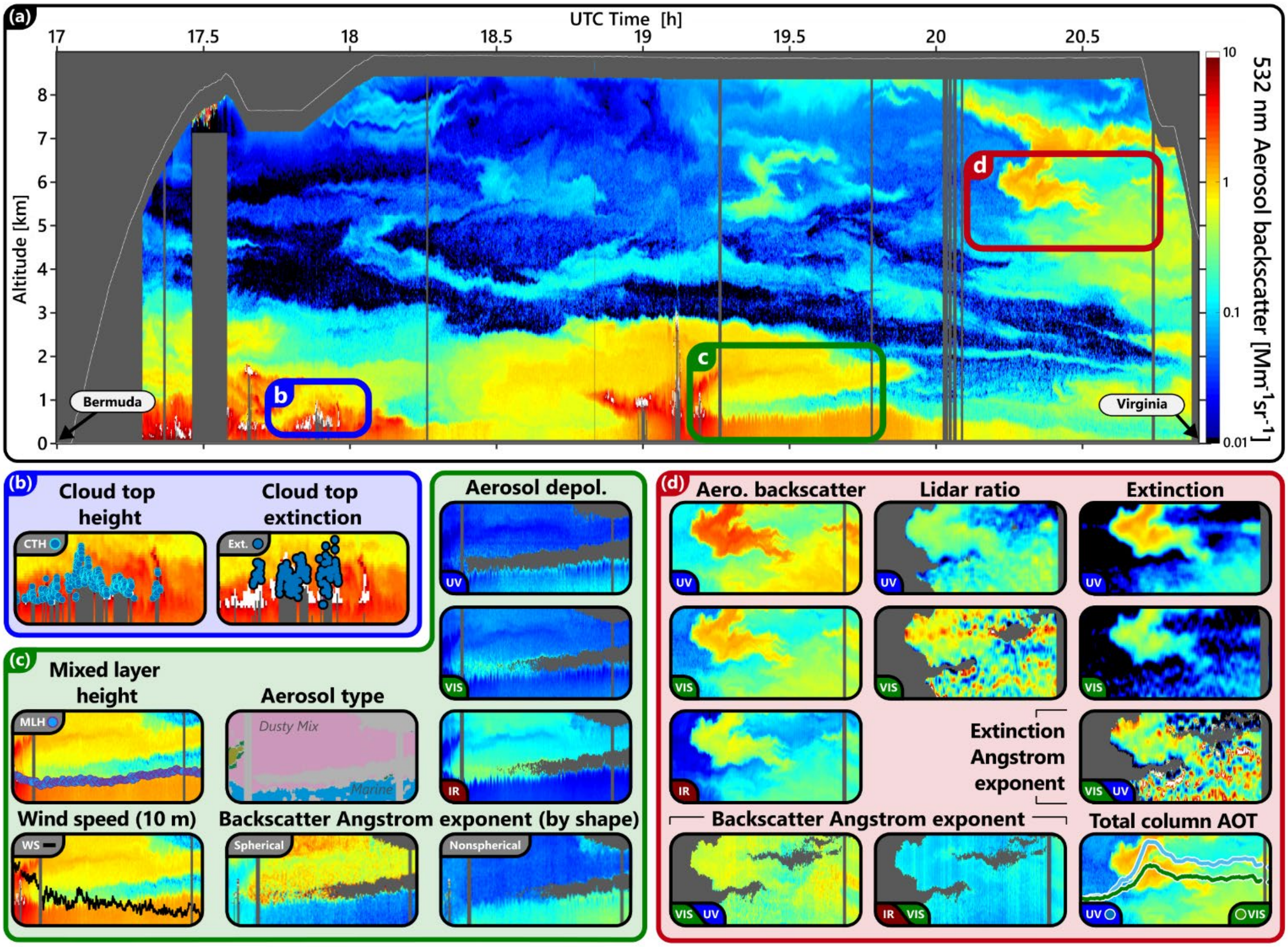

Figure 5: A qualitative visualization of selected HSRL-2 data products archived for a representative ACTIVATE flight (RF157 on 18 May 2022, L2). This flight was the second one on this day, returning from Bermuda to NASA LaRC. (a) A curtain vertical profiles of aerosol backscatter (532 nm) as a function of UTC time for the entire flight provides context of the aerosol particles measured. The labeled boxes indicate regions where subsets of HSRL-2 data products are highlighted in the corresponding small boxes below panel (a). (b) Cloud data: blue dots show (left) cloud top height and (right) cloud top extinction, averaged over the first optical depth. Both are overlaid on the backscatter curtain at the same times, with extinction being plotted on a secondary y-axis (not shown) (c) Boundary layer and lower troposphere aerosol particles: mixed layer height (blue dots), surface wind speed (black line), aerosol type, aerosol depolarization (UV (355 nm), VIS (532 nm), IR (1064 nm)), and backscatter Ångström exponents corresponding to spherical and nonspherical particles. (d) Elevated aerosol layer: aerosol backscatter (UV (355 nm), VIS (532 nm), IR (1064 nm)), backscatter Ångström exponents (VIS/UV and IR/VIS), lidar ratios (UV and VIS), aerosol extinction (UV and VIS), extinction Ångström exponent (UV/VIS), and total column AOT (UV and

VIS). The opaque cloud average extinction, surface wind speed, and total column AOT products are all overlaid on the backscatter curtains for context but plotted on a secondary y-axis and scaled for visibility inside the inset.

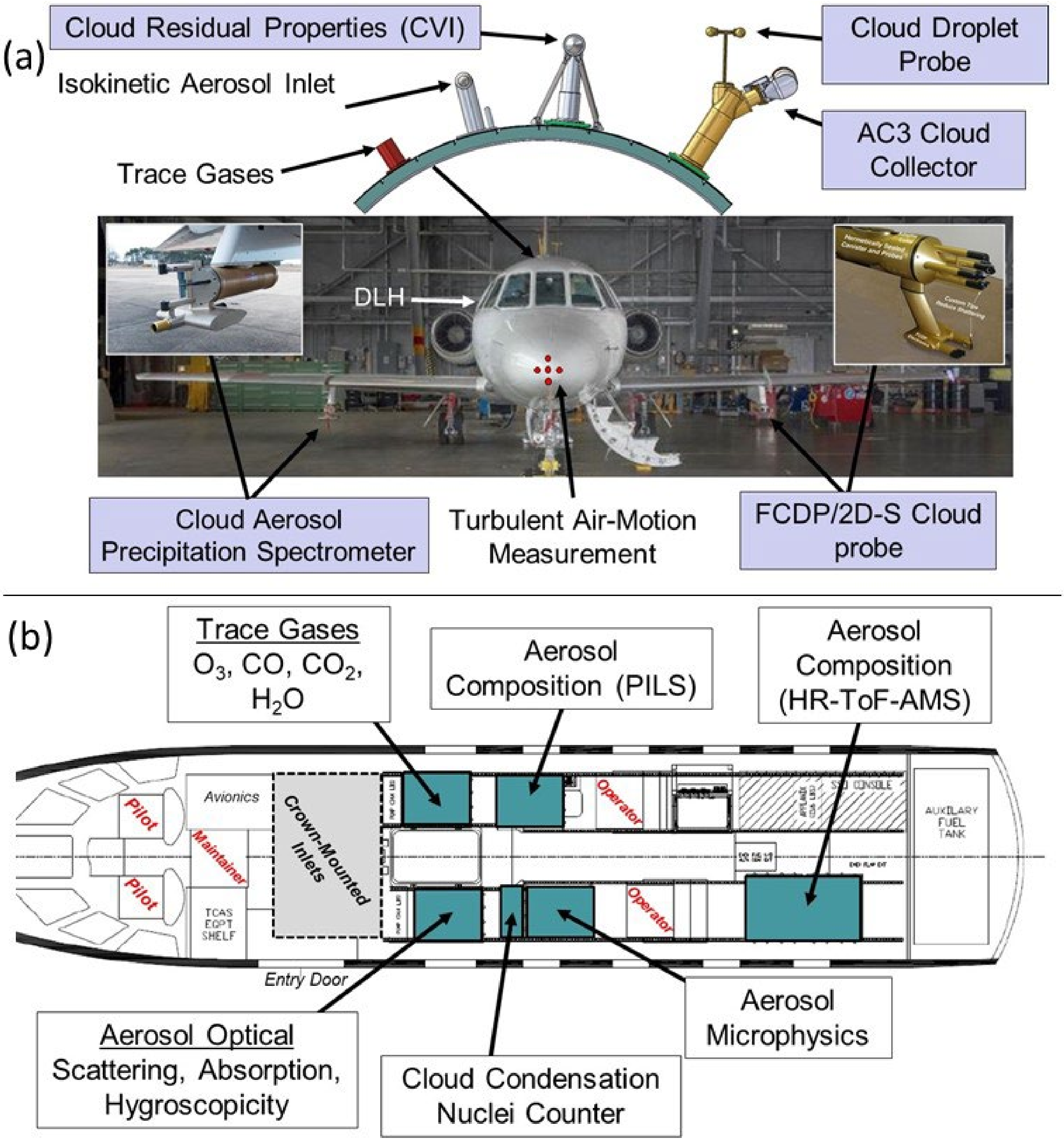

Figure 6: Visual summary of HU-25 Falcon (a) exterior probes and (b) interior layout. The Cloud Aerosol and Precipitation Spectrometer in (a) includes the Cloud and Aerosol Spectrometer (CAS) probe described in sect. 4.5.

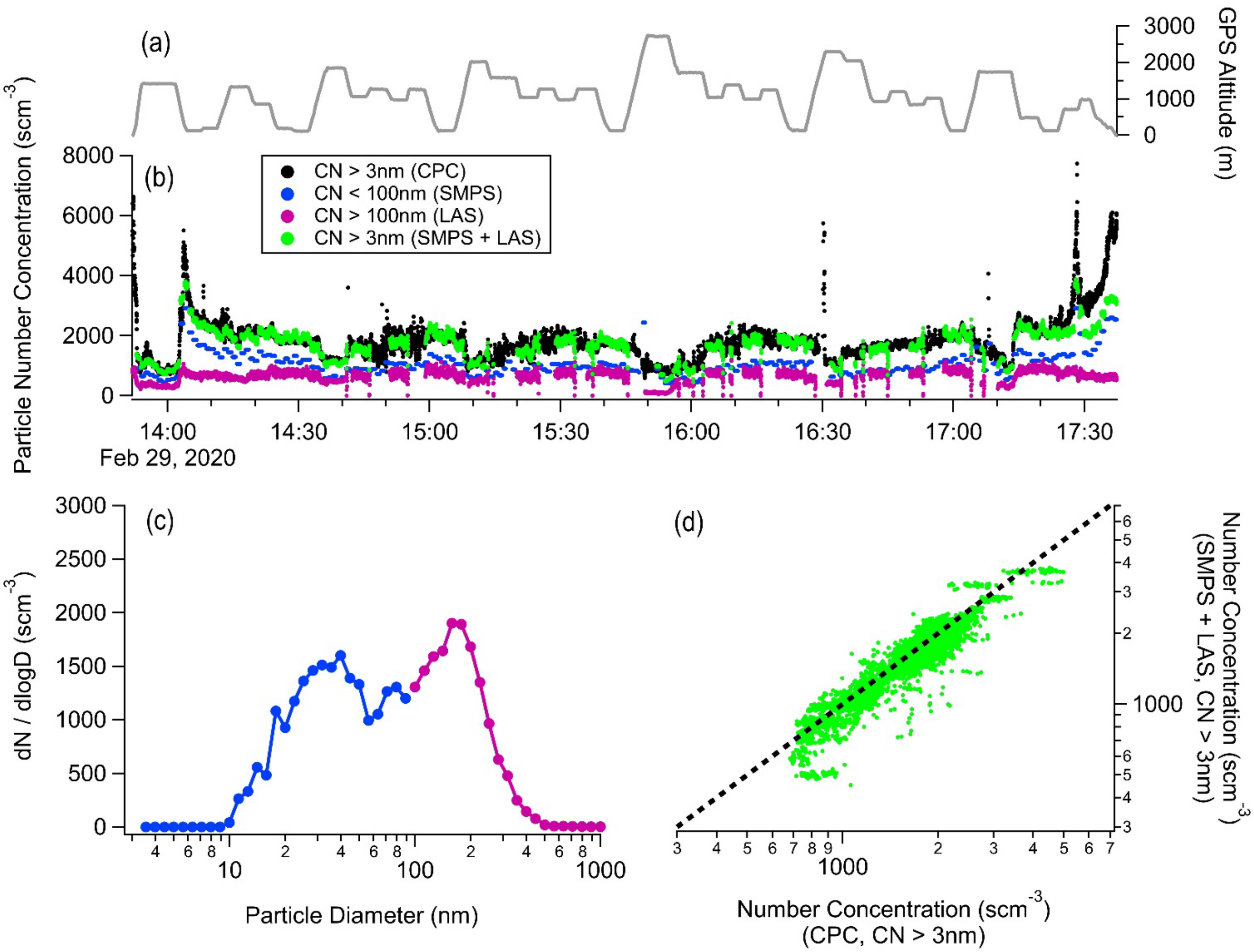

Figure 7: Closure analysis for particle number concentration measurements derived from an ultrafine CPC, SMPS, and LAS. (a-b) Time series data are shown for Research Flight 12 on 29 February 2020, (c) an average size distribution (SMPS in blue and LAS in magenta) during a BCB leg at approximately UTC 16:15 (bottom left), and (d) a scatterplot of the integrated number concentration derived from LAS+SMPS instruments against number concentration directly measured by a CPC. Units of scm^{-3} represent standard cm^{-3}. For panel d, orthogonal distance regression (ODR) linear fitting resulted in a slope of 0.961, intercept of -1.07 cm^{-3}, and coefficient of determination (r^2) of 0.868. Mean absolute error (MAE) and mean absolute percentage error (MAPE) values of 148 cm^{-3} and 8.45%, respectively, are well within stated uncertainties in Table 5 and demonstrate excellent measurement closure.

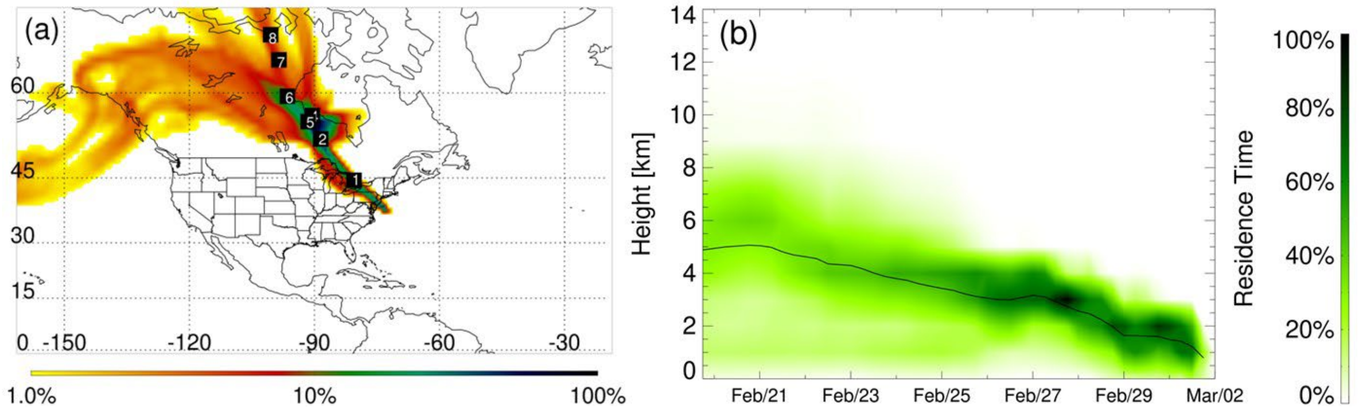

Figure 8: (a) Horizontal and (b) vertical views of simulated air mass residence time (RT) for flight measurements at 19:22 UTC on 1 March 2020 (RF14). The labels with white numbers on the map in (a) indicate the locations of maximal RT for the corresponding upwind day. Transport pathways differ significantly, and absolute RT values may vary a lot between cases. For a better comparison of transport pathways between cases, RT is expressed as a percentage of the maximal integrated value during the 10-day trajectory period. RT is color-coded with (a) logarithmic and (b) linear scales, respectively.

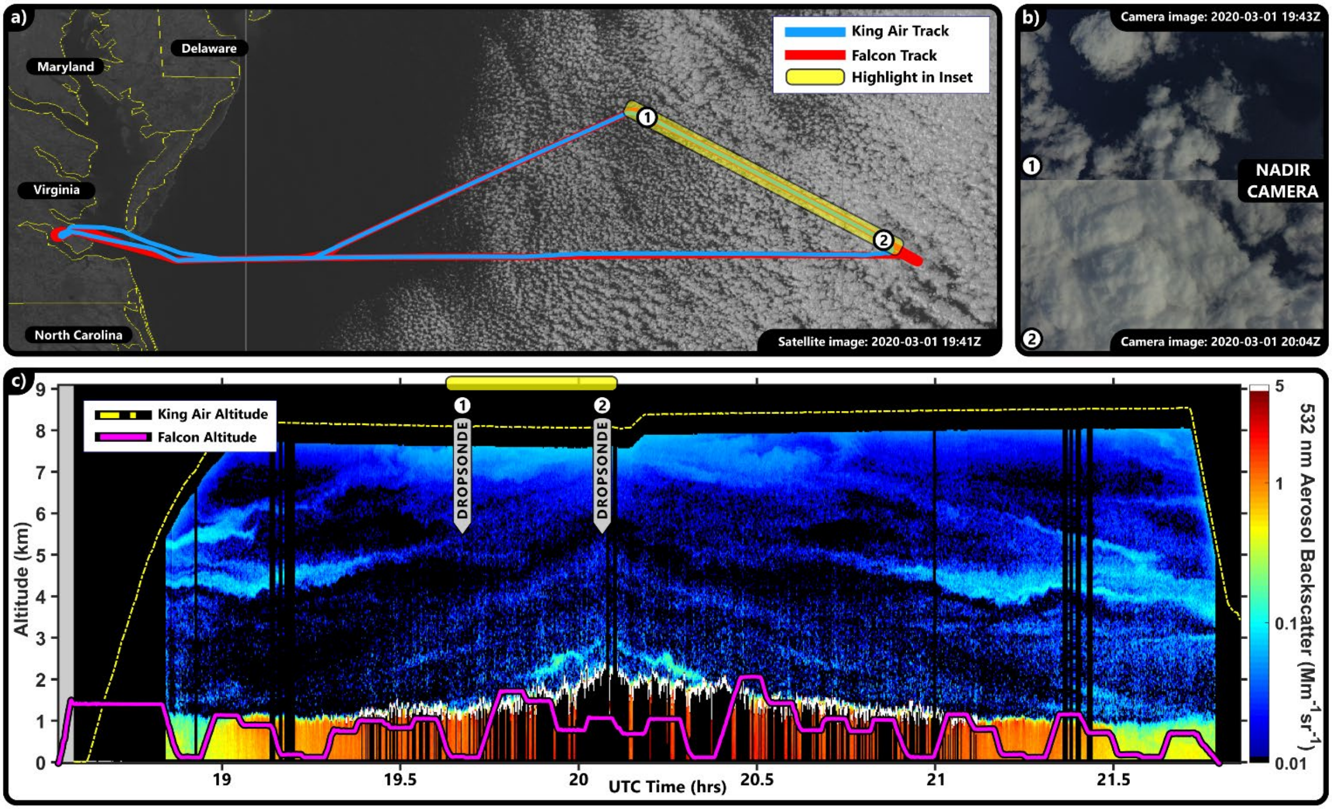

Figure 9: (a) Flight tracks of the King Air and HU-25 Falcon on RF14 on 1 March 2020 overlaid on GOES-16 visible imagery captured at UTC 19:41. The number 1 and 2 labels correspond to where the two dropsondes were launched along the downwind leg (highlighted in yellow) during this flight. These indicators are consistent in all three panels. (b) Nadir camera imagery from the King Air at the time the two dropsondes were launched. (c) Time series of the King Air aerosol backscatter shown as curtain profiles, along with the altitude trace of the King Air and Falcon aircraft. Shown also are the locations of where the two dropsondes were launched and the downwind leg is highlighted in yellow.

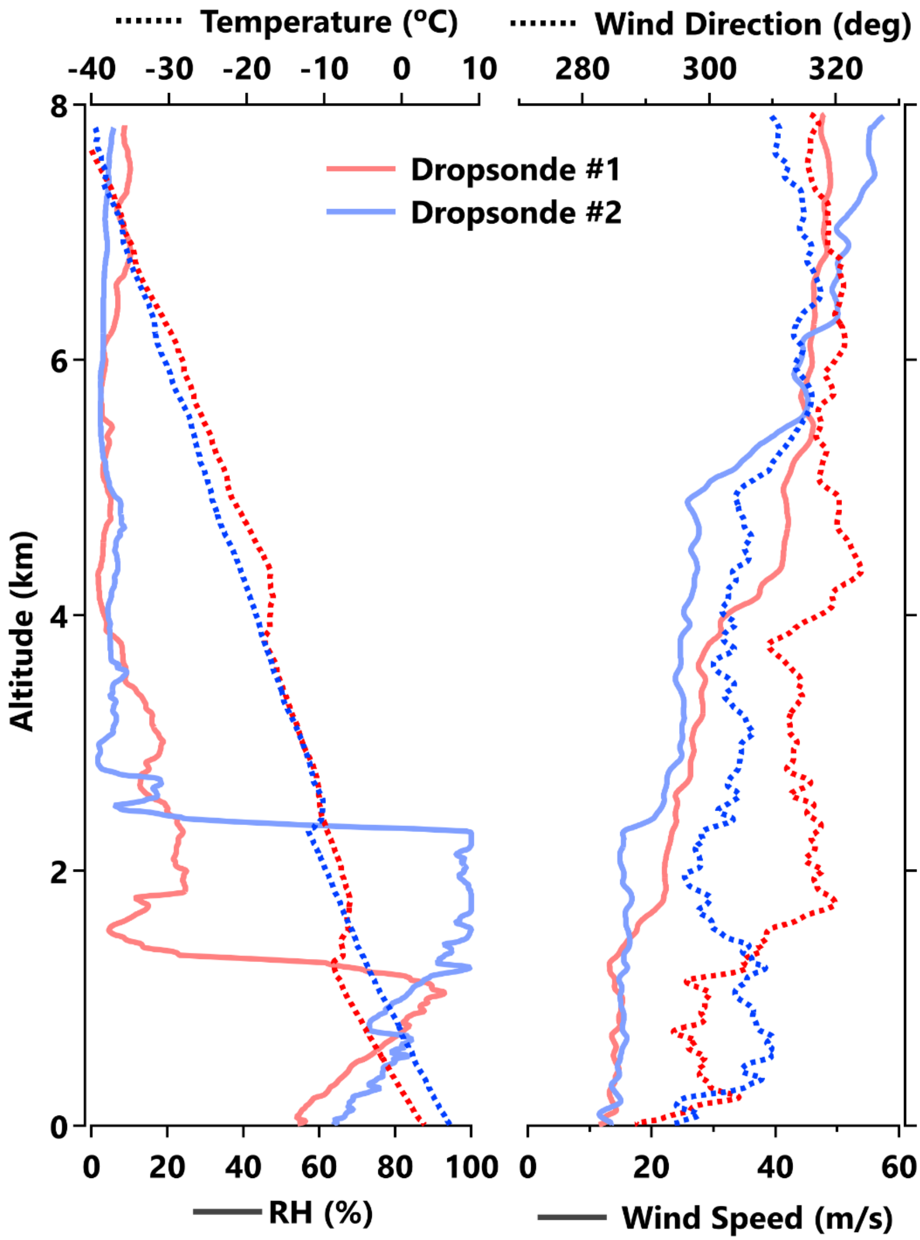

Figure 10: Vertical profiles of variables measured with the two dropsondes launched in RF14 (1 March 2020) with the markings of the drop locations shown in Fig. 9.

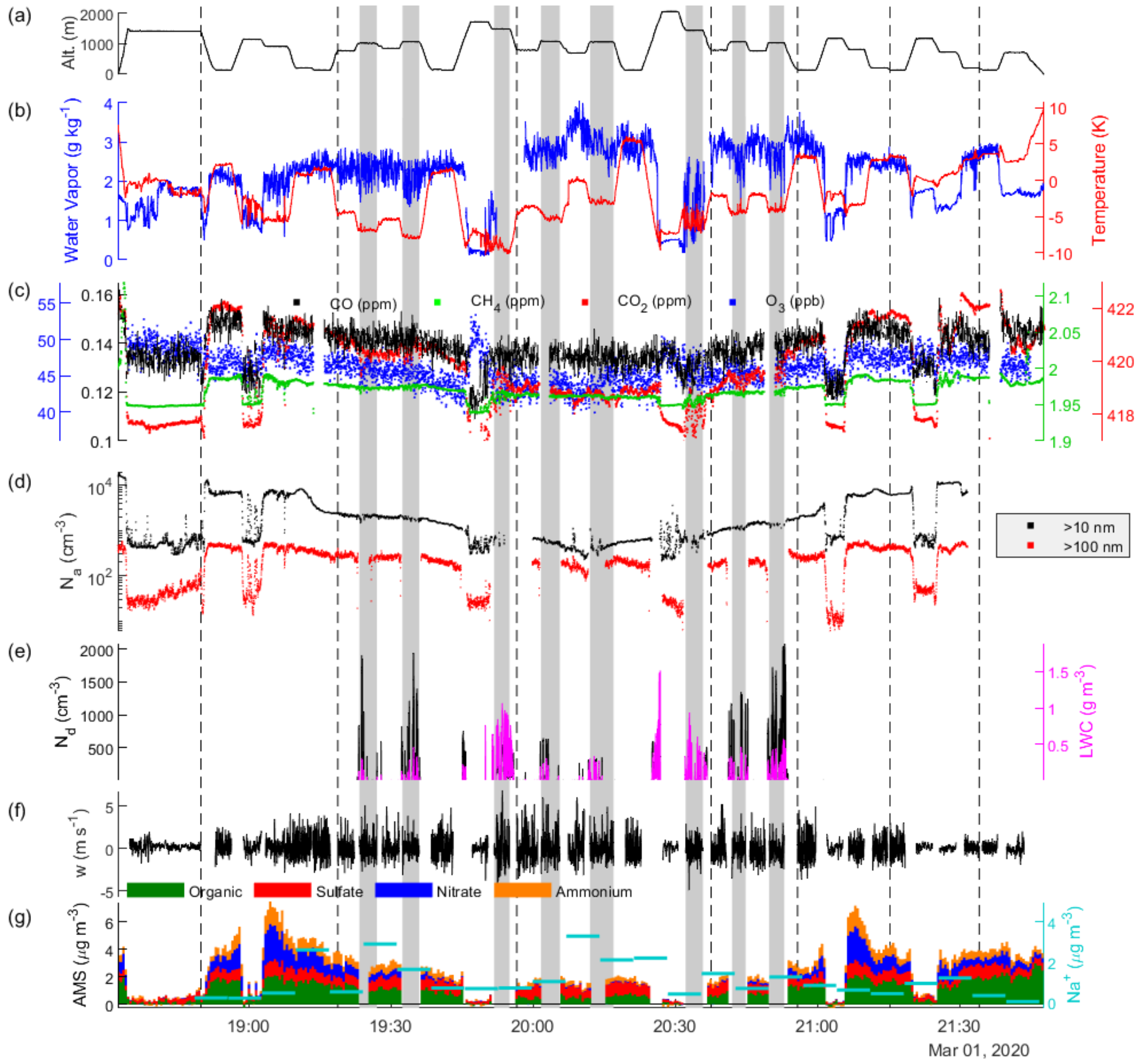

Figure 11: Time series (UTC time) of Falcon data for RF14 on 1 March 2020. Shown are the archived Falcon in situ data for (a) altitude (Applanix 610), (b) water vapor (DLH) and temperature (Rosemount 102 sensor), (c) trace gases (Picarro model G2401-m for CO, CO_2, CH_4 and 2B Tech. Inc. model 205 for O_3), (d) aerosol particle number concentration for diameter > 10 nm (TSI-3772 CPC) and > 100 nm (LAS), (e) cloud droplet number concentration and LWC (FCDP), (f) vertical wind speed (TAMMS), and (g) speciated aerosol mass concentrations from the AMS (organic, sulfate, nitrate, ammonium) and PILS (sodium). Shaded gray vertical sections denote the two level leg types in cloud (above cloud base [ACB] and below cloud top [BCT]). The dashed vertical black bars mark the beginning of either clear or cloud ensembles (ensembles in order: clear, cloud, cloud, cloud, clear, clear).

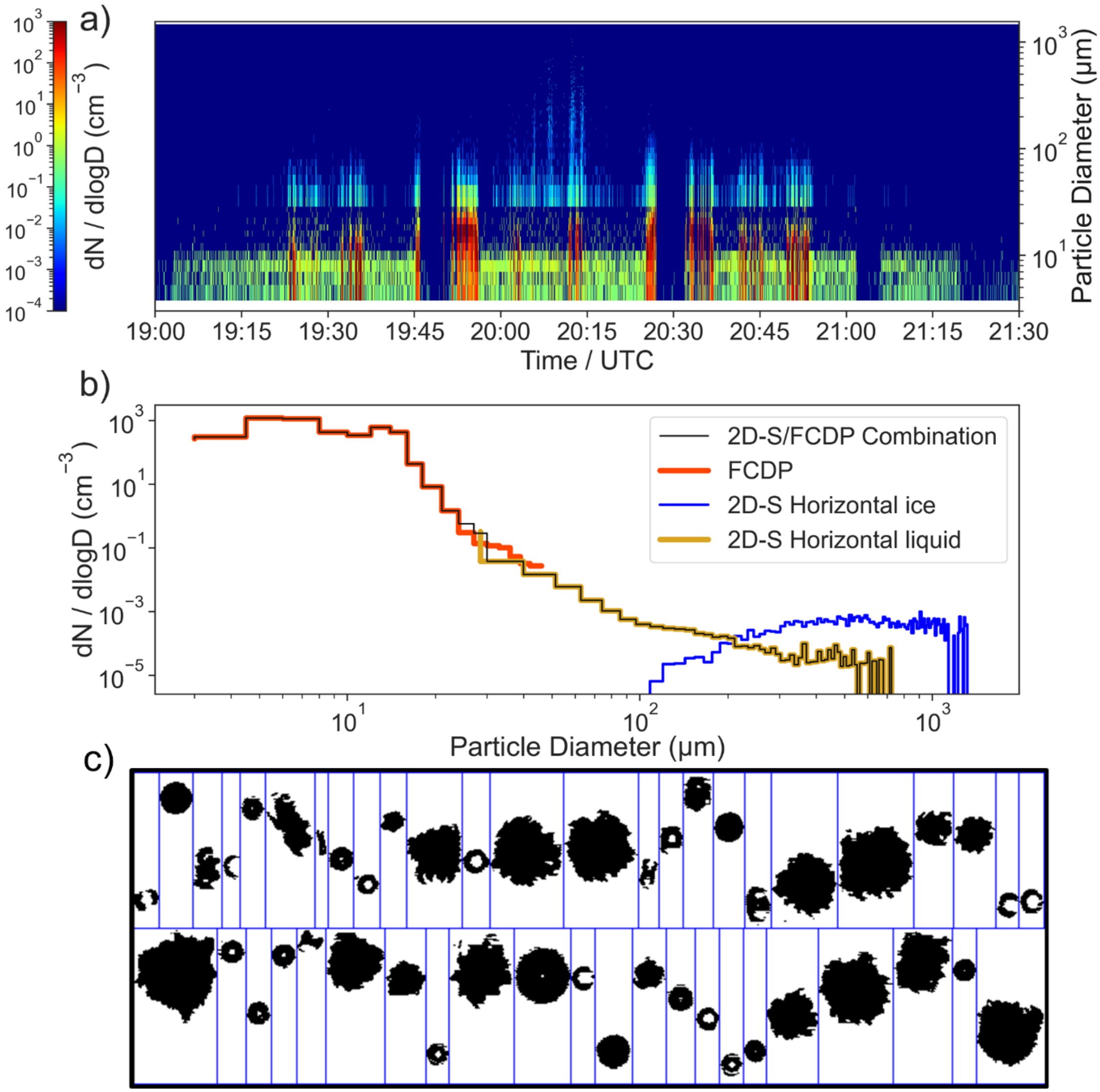

1605 Figure 12: Representative data products derived from FCDP and 2D-S on the Falcon for RF14 on 1 March 2020. (a) Time series of cloud droplet size distribution for RF14 on 1 March 2020 based on combining FCDP and 2D-S data, (b) average size distribution of liquid (FCDP and 2D-S Horizontal) and ice (2D-S Horizontal) for cloud measurements with LWC > 0.02 g m^{-3} and N_d > 10 cm^{-3}, and (c) example images captured by the 2D-S Horizontal probe for UTC 20:05:35 – 20:05:50.